

From the Department of Neurosurgery
at the Heinrich Heine University Düsseldorf

PRECISION MEDICINE DEVELOPMENTS AGAINST GLIOBLASTOMA
STEM CELLS IN A PRECLINICAL SETTING

Publication-based Dissertation

to obtain the academic title of Dr. rer. med. / Doctor of Philosophy (PhD) in Medical Sciences
from the Faculty of Medicine at Heinrich Heine University Düsseldorf

submitted by

Andres Vargas-Toscano

2022

Als Inauguraldissertation gedruckt mit Genehmigung der Medizinischen
Fakultät der Heinrich-Heine-Universität Düsseldorf

gez.:

Dekan: Prof. Dr. med. Nikolaj Klöcker

Gutachter:

Herr Prof. Simon Eickhoff (Sitzungsvorsitzende/r, Mitglied der PhD-Kommission)

Herr Prof. Michael Sabel (1. Gutachter)

Herr Prof. Guido Reifenberger (2. Gutachter)

Herr Prof. Daniel Hänggi (Habilitiertes Mitglied)

Herr Prof. Ulf Kahlert (Weiteres habilitiertes Mitglied)

To my family

Parts of the results of this thesis have been published in:

Andres Vargas-Toscano, Ann-Christin Nickel, Guanzhang Li, Marcel Alexander Kamp, Sajjad Muhammad, Gabriel Leprivier, Ellen Fritsche, Roger A Barker, Michael Sabel, Hans-Jakob Steiger, Wei Zhang, Daniel Hänggi and Ulf Dietrich Kahlert. *Rapalink-1 Targets Glioblastoma Stem Cells and Acts Synergistically with Tumor Treating Fields to Reduce Resistance against Temozolomide*. *Cancers (Basel)*, 12(12):3859; Dec (2020). <https://doi.org/10.3390/cancers12123859>.

Andres Vargas-Toscano, Dilaware Khan, Ann-Christin Nickel, Michael Hewera, Marcel Alexander Kamp, Igor Fischer, Hans-Jakob Steiger, Wei Zhang, Sajjad Muhammad, Daniel Hänggi and Ulf Dietrich Kahlert. *Robot Technology Identifies a Parkinsonian Therapeutics Repurpose to Target Stem Cells of Glioblastoma*. *CNS Oncology*. 9 no. 2: CNS58; Jun (2020). <https://doi.org/10.2217/cns-2020-0004>.

Beatriz Giesen, Ann-Christin Nickel, Alba Garzón Manjón, **Andres Vargas Toscano**, Christina Scheu, Ulf Dietrich Kahlert* and Christoph Janiak*. *Influence of Synthesis Methods on the Internalization of Fluorescent Gold Nanoparticles into Glioblastoma Stem-like Cells*. *Journal of Inorganic Biochemistry*, 203: 110952; Feb (2020). * equal contribution <https://doi.org/10.1016/j.jinorgbio.2019.110952>.

Zusammenfassung

Die langfristige und effiziente Behandlung des Glioblastoms, des häufigsten und aggressivsten primären Hirntumors, ist trotz jahrzehntelanger intensiver Forschung noch immer ein ungelöstes medizinisches Problem. Folglich konzentriert sich dieses Promotionsvorhaben auf die Entwicklung gezielter Behandlungen gegen Glioblastomstammzell-ähnliche Zellen (*Glioma Stem-like Cells*, GSCs), die als spezielle Tumorzellpopulation analog zu gesunden Stammzellen beschrieben werden. GSCs gelten maßgeblich als Grund für das Fortschreiten der Krankheit und die Vermittlung von Therapieresistenzen. Aus diesem Grund wurden methodische Ansätze der Präzisionsmedizin im Rahmen von präklinischen Modellen des Glioblastoms, d.h. GSC-Zelllinien und primäre Patientenzellen sowie neurale Stammzellen und induzierte pluripotente Stammzellen unter Verwendung von etablierten Sphäroidzellkulturtechniken getestet, um pathophysiologisch relevante Ergebnisse zu gewinnen.

Das erste Originalarbeit berichtet über die präklinische Wirksamkeit von Rapalink-1 (RL1), einer kürzlich entwickelten chemischen Verbindung, die den mTOR-Signalweg weitgehend hemmt, in Glioblastommodellen. Mechanistisch wird gezeigt, dass eine Therapie mit dieser Substanz das stammzellähnliche Verhalten und die Epitheliale-Mesenchymale Transition (EMT) von GSC effektiv unterdrücken kann. In weiteren Versuchen konnte gezeigt werden, dass die Gabe von RL1 synergistisch das therapeutische Potenzial von klinisch zugelassenen Glioblastombehandlungen, wie eine Chemotherapie mit Temozolomid und eine elektrophysikalische Therapie mit Tumor Treating Fields (TTFields), verstärken kann.

Parallel dazu wird in der zweiten Originalarbeit die Identifizierung von 22 *in vitro* gegen GSC wirksamen Medikamenten, darunter ein mTOR-Inhibitor und das klinisch zugelassene Parkinson-Medikament Trihexyphenidyl (THP), als mögliche Repurpose-Kandidaten zur Behandlung von Glioblastomen beschrieben. Diese Experimente wurden mit Hilfe eines *in vitro* Hochdurchsatz-Screens von Substanzen nach der Implementierung eines automatisierten, robotergesteuerten Liquid-Handling-Geräts durchgeführt. Darüber hinaus wurde die Wirkungsweise von THP durch mechanistische Untersuchungen analysiert.

Die zum Abschluss vorgestellte Originalarbeit berichtet über die Entwicklung einer Gold-Nanopartikel-Trägertechnologie, die eine effektive Transfektion von GSCs ermöglicht und somit als neuer Ansatz für wirksame Anti-GSC-gerichtete Behandlungen mittels Pharmakotherapie oder Gentherapie fungieren kann.

Zusammenfassend zeigt diese Dissertationsschrift, dass Ansätze der Präzisionsmedizin mittels *in vitro* Hochdurchsatzanalyse von Medikamenten, funktioneller *in vitro* Analytik und Nanotechnologie-basierter Verfahren in Glioblastommodellen potentiell synergistisch zu etablierten Behandlungsansätzen wirkende Effekte aufdecken können, welche die Entwicklung neuer Wege in der Behandlung des Glioblastoms aufzeigen können.

Summary

The long-term and efficient treatment of glioblastoma, the most common and most aggressive primary brain tumor, is still an unsolved medical problem despite decades of intensive research. Consequently, the experiments of this doctoral project were focused on the development of targeted treatments against glioblastoma stem-like cells (GSCs). GSCs are a special tumoral cell population that shares biological features of normal stem cells and is considered to be largely responsible for the progression of the disease and the mediation of therapy resistance. Therefore, we developed *precision medicine* technologies to test preclinical models of glioblastoma, including GSC cell lines and primary patient-derived cells, as well as neural stem cells and induced pluripotent stem cells by using spheroid suspension cell culture techniques in order to obtain pathophysiologically relevant findings.

The first paper reports on the preclinical efficacy of Rapalink-1 (RL1), a recently developed chemical compound that broadly inhibits the mTOR signaling pathway, in glioblastoma models. Mechanistically, it is shown that RL1 can effectively suppress stem-like behavior and the epithelial-to-mesenchymal-like transition (EMT) of GSCs. Further findings showed that exposure to RL1 synergistically reinforced the therapeutic potential of clinically approved glioblastoma treatments, namely chemotherapy with temozolomide and electrophysical therapy with Tumor Treating Fields (TTFields).

In parallel, the second paper reports on the identification of 22 drugs with *in vitro* activity against GSCs, including an mTOR inhibitor and the clinically approved Parkinson's drug trihexyphenidyl (THP), suggesting potential repurpose-candidates for glioblastoma therapy. The experiments involved an *in vitro* high throughput screening of drugs enabled by the implementation of an automated, robotically-mediated liquid handling device. Moreover, the mode of action of THP was investigated by mechanistic investigations.

The final paper included in this thesis reports on the development of a gold nanoparticle carrier technology that allows for effective transfection of GSCs and thus can function as a scaffold to increase efficacy of anti-GSC-directed treatments such as pharmacotherapy or gene therapy.

In summary, this dissertation shows that precision medicine approaches in GSC models involving *in vitro* high throughput drug screening, functional *in vitro* analyses, and nanotechnology-based methods can reveal potentially synergistic effects to established treatments, which may pave the way towards novel strategies for glioblastoma therapy.

List of abbreviations

ACh	Acetylcholine	FITC	Fluorescein isothiocyanate
ANOVA	Analysis of variance	FRET	Fluorescence resonance energy transfer
AuNP	Gold Nanoparticles	GABA	Gamma-Aminobutyric acid
AuPEI-FITC	Fluorescent gold	GBM	Glioblastoma
BBB	Blood-brain barrier	GSCs	Glioblastoma Stem Cells
BCSCs	Brain cancer stem-like cells	HRTEM	High-resolution transmission electron microscopy
BSA	Bovine serum albumin	5-HT	Serotonin
BSC	Best standard-of-care	IC₅₀	Half maximal inhibitory concentration
CER	Cerebellum	IDH-wt	Isocitrate dehydrogenase wildtype
CGGA	Chinese Glioma Genome Atlas	iNSC	Induced neural stem cell
CI	Combination Index	IR	Infrared
CL	Classical	MeOH	Methanol
CT	Computer tomography	MES	Mesenchymal
CTG	CellTiter-Glo	MGMT	O ⁶ -methylguanine-DNA methyltransferase
CTX	Fetal brain cortex	μM	Micromolar
DLS	Dynamic light scattering	MRI	Magnetic resonance imaging
DMEM	Dulbecco's Modified Eagle's medium	mTOR	Mammalian Target of Rapamycin
DMSO	Dimethyl sulfoxide	mTORC 1/2	Mammalian target of rapamycin complex 1 and 2
DNA	Deoxyribonucleic acid	MTT	3-(4,5-dimethylthiazol-2-yl) 2,5-diphenyl tetrazolium bromide
4EBP1	Eukaryotic translation initiation factor 4E-binding protein 1	ndGBM	Newly diagnosed glioblastoma
EMT	Epithelial-like-to-mesenchymal transition		
ESMO	European Society for Medical Oncology		
FACS	Fluorescence-activated cell sorting		

NE	Neural	SERRS	Surface enhanced resonance Raman scattering
nM	Nanomolar	STEM	Scanning transmission electron microscopy
NP	Nanoparticle	TCGA	The Cancer Genome Atlas
PBS	Phosphate-buffered saline	TGA	Thermogravimetric analysis
PEI	Polyethylene imine	THP	DL-trihexyphenidyl hydrochloride
pGBM	Primary glioblastoma	TMZ	Temozolomide
PN	Proneural	TTFIELDS	Tumor Treating Fields
rGBM	Recurrent glioblastoma	UV-VIS	Ultraviolet-visible light
RL1	Rapalink-1	XTT	Sodium 3'-[1-(phenylaminocarbonyl)-3,4-tetrazolium]-bis (4-methoxy6-nitro) benzene sulfonic acid hydrate
RNA	Ribonucleic acid		
S6	Ribosomal protein S6		

Table of contents

1. Introduction	1
1.1. Motivation and overview.....	1
1.2. Precision medicine in cancer and glioblastoma.....	1
1.3. Overview of electric fields, drug repurposing and nanoparticles in glioblastoma ...	2
1.4. Aim of the thesis.....	3
1.5. Ethics approval	3
2. Paper 1 - Rapalink-1 Targets Glioblastoma Stem Cells and Acts Synergistically with Tumor Treating Fields to Reduce Resistance against Temozolomide. <i>Andres Vargas-Toscano, Ann-Christin Nickel, Guanzhang Li, Marcel Alexander Kamp, Sajjad Muhammad, Gabriel Leprivier, Ellen Fritsche, Roger A Barker, Michael Sabel, Hans-Jakob Steiger, Wei Zhang, Daniel Hänggi and Ulf Dietrich Kahlert. Cancers (Basel), 12(12):3859; Dec (2020)</i>	4
3. Paper 2 - Robot Technology Identifies a Parkinsonian Therapeutics Repurpose to Target Stem Cells of Glioblastoma. <i>Andres Vargas-Toscano, Dilaware Khan, Ann-Christin Nickel, Michael Hewera, Marcel Alexander Kamp, Igor Fischer, Hans-Jakob Steiger, Wei Zhang, Sajjad Muhammad, Daniel Hänggi and Ulf Dietrich Kahlert. CNS Oncology. 9 no. 2: CNS58; Jun (2020)</i>	5
4. Paper 3 - Influence of Synthesis Methods on the Internalization of Fluorescent Gold Nanoparticles into Glioblastoma Stem-like Cells. <i>Beatriz Giesen, Ann-Christin Nickel, Alba Garzón Manjón, Andres Vargas Toscano, Christina Scheu,Ulf Dietrich Kahlert and Christoph Janiak. Journal of Inorganic Biochemistry, 203: 110952; Feb (2020)</i>	6
5. Discussion	7
6.1. General conclusions.....	9
6. References.....	10
7. Acknowledgements	

1. Introduction

1.1. Motivation and overview

In the current evolving era of *precision medicine*, complex diseases like cancer and especially brain tumors require the rapid implementation of advanced technologies to develop effective treatments¹⁻³. Particularly, the complex field of glioblastoma requires the development of novel effective treatments because the overall survival of patients with glioblastoma has not improved substantially since the introduction of temozolomide (TMZ) more than 15 years ago⁴. On the other side, advances in the molecular genetics of glioblastoma have revealed that patients whose tumors lack mutations in the isocitrate dehydrogenase 1 and 2 genes, i.e. are IDH-wildtype glioblastomas^{5,6} which have a less favorable prognosis and show poorer response to standard treatment of surgery, radiotherapy and TMZ when compared to patients with IDH-mutant high-grade gliomas⁷.

Moreover, glioblastomas are composed of heterogeneous cell populations that may demonstrate a hierarchical behavior, with the most aggressive cells sharing equivalent characteristics and molecular markers with normal stem cells, fetal cells and induced stem cells. Thus, these cells with stem-like traits are referred to as glioblastoma stem-like cells (GSCs) and show a direct correlation between biological aggressiveness and their degree of stemness or differentiation. This behavior is complemented by the highly invasive and proliferative pattern of cells that transition from a static epithelial-like behavior (proneural), to a higher invasive (mesenchymal) behavior through the process of epithelial-like-to-mesenchymal transition (EMT)^{8,9}, thereby contributing to tumor progression^{7,10-13}. This stem-like-cell hierarchy has been evidenced in some of the most aggressive human cancer types, both solid and hematopoietic, consolidating the tumor stem cell theory and creating opportunities for interdisciplinary research between developmental neurobiology and brain tumor research. Therefore, the rationale and potential implications of developing *precision medicine* technologies in stem cell-like glioblastoma models are the main motivation drivers of this dissertation.

1.2. Precision medicine in cancer and glioblastoma

Cancer is a highly adaptable, genetically complex disease. For this reason, traditional “one size fits all” approaches, such as broad spectrum chemotherapies, have fallen short and are being replaced by molecularly-tailored, highly targeted medical treatments and procedures in several cancer types^{1,3}. This is the core of most *precision medicine* approaches. Originally, this concept was called ‘personalized medicine’ but due to misunderstandings the European Society for Medical Oncology (ESMO) and the National Research Council of the United States established the term “*precision medicine*” as the new standard^{1,14}. It is defined by the ESMO as a healthcare approach with the primary aim of identifying which interventions are likely to be of most benefit to which patients, based upon the features of the individuals and their disease^{1,14,15}.

Applied to glioblastoma and GSCs, if we have an extensive knowledge of the molecular characteristics of the tumor in individual patients and know several available tools to target these specific features, we would theoretically ensure the development of highly efficient treatments with minimal adverse reactions. An interesting example of *precision medicine* in glioblastoma treatment, is the *GBM AGILE* (Adaptive Global Innovative Learning Environment) fast-track research system, which is further combined with translational research⁴.

1.3. Overview of electric fields, drug repurposing and nanoparticles in glioblastoma

In the past years, a new category of cancer therapy called Tumor Treating Fields (TTFields) or alternating electric fields was approved for the treatment of glioblastoma patients^{16–18}. This is the only treatment that has partially improved the overall survival in IDH-wildtype (IDH-wt) glioblastoma patients in more than 15 years¹⁹. Mechanistically, it applies low intensity alternating electric fields to the scalp of the patient, thereby supposed to produce an antimetabolic effect in the tumor, with limited toxicity and improved overall survival of the patients after two and five years. However, specific interactions with other treatments and the effects on GSCs remain widely unknown¹⁸.

Moreover, there are several approved drugs that are currently used for the treatment of oncological and non-oncological diseases, which have a high chance of being repurposed for a novel treatment indication in different types of cancer²⁰. For this reason, an industry-grade, liquid dispensing robotic system for *in vitro* drug screening in the research setting was established and used for performing a high throughput drug screening on molecularly characterized GSC models. Based on this approach, Rapalink-1 (RL1), a highly potent Mammalian Target of Rapamycin (mTOR) pathway inhibitor was identified as a drug showing *in vitro* efficacy against GSCs²¹. In the context of cancer, mTOR is a key player in the activation of cell growth, reprogramming of cell metabolism and structural cytoskeleton remodeling¹⁸. Thus, mTOR inhibitors have been broadly used as chemotherapeutic agents in glioblastoma and other types of tumors (i.e. subependymal giant cell astrocytoma, meningioma, advanced renal cell carcinoma, etc.), as well as immunomodulators indicated in kidney transplantation and other medical conditions^{22(p2),23,24}.

Finally, this thesis focused on nanotechnology as an innovative field of research with increasing applications in medicine during the past years. Specifically, nanoparticles may function as novel treatment vectors that offer many applications in both preclinical research and clinical medicine^{25,26}. Therefore, locally-synthesized colloidal gold nanoparticles (AuNP) were developed, making use of the highly customizable and biocompatible characteristics of this material, as a potentially novel tool for glioblastoma therapy and further research.

1.4. Aim of the thesis

The main aim of this thesis was to generate preclinical evidence that may lead to the development of novel targeted next-generation therapies against glioblastoma through *precision medicine* approaches. The project involved *state of the art* technologies, pathophysiologically relevant three-dimensional culture techniques, and either *in vitro*, *ex vivo*, or *in silico* models. In the chapters 3-5 the employed *precision medicine* technologies and obtained results are explained in detail within the individual papers, starting with the most recently published one.

1.5. Ethics approval

Ethics approval for the use of cell models to study brain cancer biology was obtained from the Ethics Committee of the Medical Faculty of Heinrich Heine University Düsseldorf (study ID 5841R). Cortical fetal neural stem cells were collected from human fetal cortical tissue grown under neurosphere conditions (study ID #5206). Primary glioblastoma tumor tissue samples were obtained from patients treated at the Department of Neurosurgery, Heinrich Heine University Düsseldorf. All patients gave their informed consent for the use of their tissue samples and clinical data for research purposes. The study was conducted in accordance with the Declaration of Helsinki, and the protocol was approved by the Ethics Committee of the Medical Faculty of Heinrich Heine University Düsseldorf (#2019-484-FmB).

2. Paper 1 - Rapalink-1 Targets Glioblastoma Stem Cells and Acts Synergistically with Tumor Treating Fields to Reduce Resistance against Temozolomide. *Andres Vargas-Toscano*, Ann-Christin Nickel, Guanzhang Li, Marcel Alexander Kamp, Sajjad Muhammad, Gabriel Leprivier, Ellen Fritsche, Roger A Barker, Michael Sabel, Hans-Jakob Steiger, Wei Zhang, Daniel Hänggi and Ulf Dietrich Kahlert. *Cancers (Basel)*, 12(12):3859; Dec (2020)

The paper with supplementary data embedded in this chapter was reprinted with the following considerations:

- Published in the year 2020 by the Open Access journal *Cancers (Basel)* from the publisher *MDPI (Multidisciplinary Digital Publishing Institute)* under the Creative Commons Attribution License BY 4.0, allowing the reprint of academic non-commercial Dissertations/Thesis as explained in the following webpage link: <https://www.mdpi.com/openaccess>
- The original publication is available under the journal webpage link: <https://www.mdpi.com/2072-6694/12/12/3859>
- It can be accessed via PubMed under the following webpage link: <https://pubmed.ncbi.nlm.nih.gov/33371210/>

Article

Rapalink-1 Targets Glioblastoma Stem Cells and Acts Synergistically with Tumor Treating Fields to Reduce Resistance against Temozolomide

Andres Vargas-Toscano¹, Ann-Christin Nickel¹, Guanzhang Li², Marcel Alexander Kamp¹, Sajjad Muhammad¹, Gabriel Leprivier³, Ellen Fritsche⁴, Roger A. Barker⁵, Michael Sabel¹, Hans-Jakob Steiger¹, Wei Zhang², Daniel Hänggi¹ and Ulf Dietrich Kahlert^{1,2,6,*}

¹ Clinic for Neurosurgery, Medical Faculty, Heinrich-Heine University Düsseldorf, 40225 Düsseldorf, Germany; Andres.VargasToscano@med.uni-duesseldorf.de (A.V.-T.); Ann-Christin.Nickel@med.uni-duesseldorf.de (A.-C.N.); marcelalexander.kamp@med.uni-duesseldorf.de (M.A.K.); sajjad.muhammad@med.uni-duesseldorf.de (S.M.); Michael.Sabel@med.uni-duesseldorf.de (M.S.); Hans-Jakob.Steiger@med.uni-duesseldorf.de (H.-J.S.); daniel.haenggi@med.uni-duesseldorf.de (D.H.)

² Beijing Neurosurgical Institute, Tiantan Hospital, Beijing 100050, China; liguanzhang122@163.com (G.L.); zhangwei_vincent@126.com (W.Z.)

³ Institute of Neuropathology, Heinrich-Heine University Düsseldorf, 40225 Düsseldorf, Germany; GabrielClementGuillaume.Leprivier@med.uni-duesseldorf.de

⁴ Leibniz Research Institute for Environmental Medicine (IUF) and Medical Faculty Heinrich-Heine University Düsseldorf, 40225 Düsseldorf, Germany; ellen.fritsche@iuf-duesseldorf.de

⁵ Department of Clinical Neurosciences and WT-MRC Stem Cell Institute, University of Cambridge, Cambridge CB2 1QN, UK; rab46@cam.ac.uk

⁶ German Consortium for Translational Cancer Research (DKTK), Essen/Düsseldorf, 40225 Düsseldorf, Germany

* Correspondence: mail@ulf-kahlert.com; Tel.: +49-2118108013

Received: 8 November 2020; Accepted: 18 December 2020; Published: 21 December 2020



Simple Summary: Glioblastoma (GBM) resistance to standard treatment is driven by stem-like cell behavior and epithelial-like-mesenchymal transition. The main purpose of this paper was to functionally validate a novel discovered pharmacological strategy to treat GBM, the dual mTOR pathway inhibitor Rapalink-1 (RL1) using relevant stem cell models of the disease to unravel mechanistic insights. Our approach also interrogates combination studies with clinical treatment options of tumor treating fields (TTFields) and the best standard of care chemotherapy, temozolomide (TMZ). We provided clinical relevance of our experimental work through in silico evaluation on molecular data of diverse patient samples. RL1 effectively impaired motility and clonogenicity of GBM stem cells and reduced the expression of stem cell molecules. We elucidated a synergistic therapeutic potential of the inhibitor with TTFields to minimize therapy resistance toward TMZ, which supports its consideration for further translational oriented studies.

Abstract: Glioblastoma (GBM) is a lethal disease with limited clinical treatment options available. Recently, a new inhibitor targeting the prominent cancer signaling pathway mTOR was discovered (Rapalink-1), but its therapeutic potential on stem cell populations of GBM is unknown. We applied a collection of physiological relevant organoid-like stem cell models of GBM and studied the effect of RL1 exposure on various cellular features as well as on the expression of mTOR signaling targets and stem cell molecules. We also undertook combination treatments with this agent and clinical GBM treatments tumor treating fields (TTFields) and the standard-of-care drug temozolomide, TMZ. Low nanomolar (nM) RL1 treatment significantly reduced cell growth, proliferation, migration, and clonogenic potential of our stem cell models. It acted synergistically to reduce cell growth when applied in combination with TMZ and TTFields. We performed an in silico analysis from

the molecular data of diverse patient samples to probe for a relationship between the expression of mTOR genes, and mesenchymal markers in different GBM cohorts. We supported the *in silico* results with correlative protein data retrieved from tumor specimens. Our study further validates mTOR signaling as a druggable target in GBM and supports RL1, representing a promising therapeutic target in brain oncology.

Keywords: glioblastoma; rapalink-1; tumor treating fields; EMT; therapy resistance; human stem cell *in vitro* platform; drug development; risk assessment; mTOR

1. Introduction

Glioblastoma (GBM) is a fatal disease that can occur at any age, with a worse prognosis in older patients. The disease is considered to be driven by glioblastoma stem cells (GSCs), a small subpopulation of highly tumorigenic cells that have stem-like properties including self-renewal, high proliferation rates, and an ability to generate and regenerate different progenies of the tumor [1–5]. GSCs also regulate the molecular process of epithelial-like-to-mesenchymal-like transition (EMT) process, in which the cells acquire a greater motile and therapy resistant phenotype [6].

After maximal safe surgical macroscopic resection of a newly diagnosed GBM (ndGBM), the consensus for best standard-of-care (BSC) involves treating the microscopic dissemination and/or the remaining unresected tumor through a combination of the chemoagent temozolomide (TMZ) and radiotherapy [1,7]. The constitution of the genomic loci of isocitrate dehydrogenase 1 (IDH1) and the activation of O⁶-methylguanine-DNA methyltransferase (MGMT) have been identified to be predictive for BSC response [8,9]. Additionally, sub classification of GBM into transcriptomic or epigenetic subtypes, associated with different gene activation signatures and clinical features have been described [10]; namely, proneural (PN), neural (NE), mesenchymal (MES), and classical (CL). Despite this progress in clinical diagnostics, adequate advances on the therapeutic side, targeting molecular features of the disease, are lagging behind. Anti-stem cell/anti-EMT directed therapies, ideally in a disease subtype specific manner, are desirable [11].

Recently, a novel therapy termed tumor treating fields (TTFields) has been approved for clinical treatment as both monotherapy for recurrent GBM (rGBM) and in combination with adjuvant post-chemoradiation TMZ for ndGBM [12,13]. It is believed to generate a main non-invasive antimitotic effect on the cells by delivering low intensity, intermediate frequency, alternating electric fields, locally targeting the tumor bed. However, the mode of action is not fully understood [14]. Additionally, the available knowledge as to its therapeutic potential in combination with other treatment regimens, or its potential to attack GSC/EMT is not fully known.

Mammalian Target of Rapamycin (mTOR) is a hallmark signaling pathway in cancer including GBM, frequently taken into account as therapeutic targets in major clinical studies [15,16]. Elevated mTOR signaling activity has been associated with the activation of EMT and GSCs maintenance [17–19]. Historically, the clinical translation of pharmacological strategies to block mTOR signaling has been challenging due to the emergence of therapy resistance or ineffectivity in signal suppression under therapy [20,21]. However, the recent generation of mTOR inhibitors directed simultaneously against the two branches of the network (mTORC1 and mTORC2) a.k.a. Rapalinks, have shown great therapeutic potential in an experimental trial of GBM [22]. However, hardly anything is known on the effects of Rapalinks on GSCs EMT biology in GBM.

Thus, we sought to tackle these knowledge gaps by using an *in vitro* platform composed of well-characterized GSCs and non-cancer neural stem cells derived from fetal origin or human induced pluripotent stem cells. Our drug characterization study employed a wide portfolio of functional bioassays and also included an *ex vivo* analysis after an *in silico* interrogation of clinical datasets to further validate the clinical relevance of our experimental findings. By integrating an experimental

TTFields system in our experimental design, we believe our results are of interest for translational oriented research community of neuro oncology and beyond.

2. Results

2.1. Rapalink-1 Inhibits Cell Growth in Glioblastoma Stem Cells (GSCs) Compared to Non-Cancerous Cells

We used established GSC models in order to corroborate the effect of a chosen compound of the Rapalink class (Rapalink-1, RL1) [22] in our models. Details about the molecular properties of the models can be found in Figure 1 and Table 1. The drug dose dependent decrease in cell growth was just visible at two days with a clear effect peak at four days (Figure 1a). We then calculated the respective half maximal inhibitory concentration (IC₅₀) values, leading to values in the nano-molar (nM) range (Table 1). In order to have a non-cancerous control for the cell growth analysis, we treated and calculated the IC₅₀ from an induced neural stem cell (iNSC) model derived from induced pluripotent stem cells (IMR90/4), and from fetal brain cortex (CTX) and cerebellum (CER) derived neural stem cells. We then compared the main protein expression profiles of the mTOR pathway, namely eukaryotic translation initiation factor 4E-binding protein 1 (4EBP1), ribosomal protein S6 (S6), and Akt with a clearly higher mTOR expression in cancer cells compared to non-cancerous stem cells, mainly with the 4EBP1 marker (Figure 1b). Based on curve analysis and IC₅₀ values, the cell line NCH644, characterized as PN [23], was the most resistant cancerous model, followed by the CL-subtype cell line GBM1 [24]. The MES subtypes BTSC233 and JHH520 [25,26] followed in drug sensitivity, finally followed by the pediatric glioblastoma model SF188, which was the most sensitive and only MGMT-unmethylated cell line used (Figure 1c,d). All cell lines were classified accordingly by other institutions and verified by our lab using RNA sequencing data from an ongoing project [10,27]. Furthermore, the effect of RL1 was significantly more potent in cancerous models compared to the non-cancerous tested models (Figure 1d).

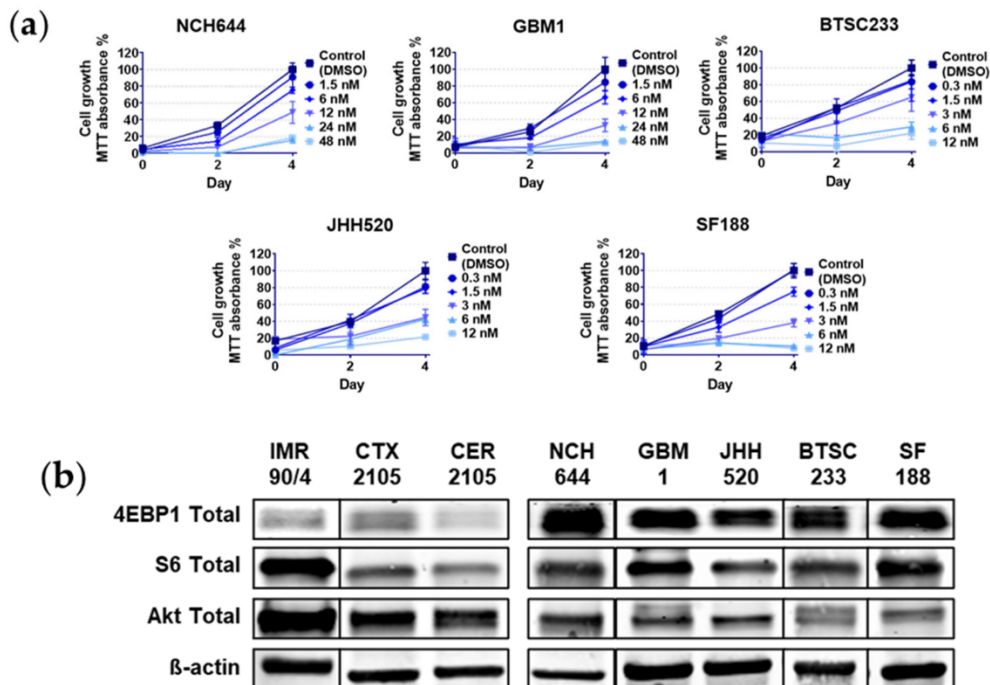


Figure 1. Cont.

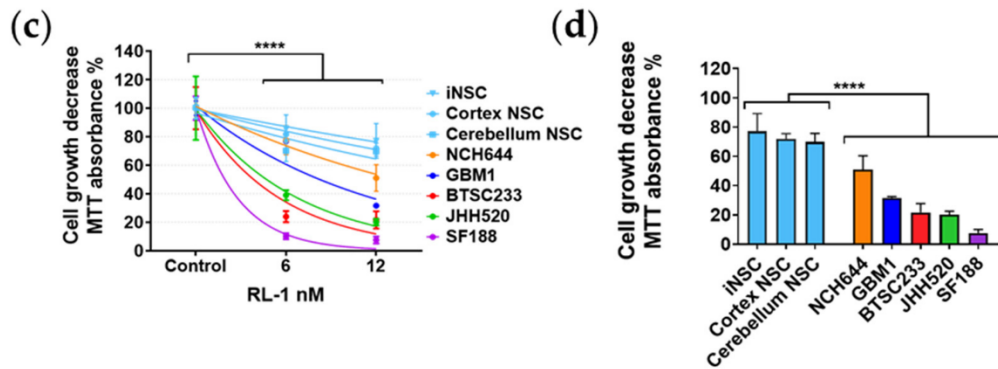


Figure 1. RL1 cell growth effects. (a) Cell growth of glioblastoma stem cells (GSCs) measured with MTT (3-(4,5-dimethylthiazol-2-yl) 2,5-diphenyl tetrazolium bromide) absorbance assay after two and four days of incubation, (b) main protein expression proteins of the mTOR pathway in cancerous and non-cancerous cells, (c) cell growth dose dependent decrease comparison measured with MTT absorbance after 4 days of incubation, (d) 4-day incubation significant difference of cell growth decrease measured with MTT absorbance of cancer GSCs compared to non-cancerous NSCs. All the plots present the mean and the standard deviation. The p -value < 0.05 was considered statistically significant in all analysis. Statistical tests performed for two variables, unpaired Student’s t -test, for more than two related variables, one-way-ANOVA. The significance of the difference between groups was described as **** $p < 0.0001$.

Table 1. Cell line characteristics.

Type	Cell Line	Color Code ¹	RL-1 IC ₅₀ nM	TMZ IC ₅₀ μM	Gender	Age Group	Molecular Subtype (Verhaak)	MGMT Status	IDH Status	ALDH1A3 Expression
Glioblastoma stem cells	NCH644		10.5	110	Female	Adult	Poneural	Methylated	Wildtype	Negative
	GBM1		7	5	Male	Adult	Classical	Methylated	Wildtype	Positive
	BTSC233		3	10	Female	Adult	Mesenchymal	Methylated	Wildtype	Positive
	JHH520		2.2	10	Female	Adult	Mesenchymal	Methylated	Wildtype	Positive
	SF188		1.8	40	Male	Pediatric	-	Unmethylated	Wildtype	Positive
Induced Neural Stem Cell	IMR 90/4		15.5	-	-	-	-	-	-	-
	Cortex		12	-	-	-	-	-	-	-
	Cerebellum		11	-	-	-	-	-	-	-

¹ Color code defined to simplify the interpretation of the figures.

2.2. RL1 Inhibits mTOR Pathway Signaling Activity

Next, we undertook a protein expression analysis to validate if the described effect of RL1 on mTORC1/2 applied to our GSCs (Figure 2a,b). For mTORC1 activity, we used the downstream markers phospho-4EBP1-Ser⁶⁵ and phospho-S6-Ser⁴⁷³, and for mTORC2, we used phospho-AKT-Ser⁴⁷³. Phosphorylation of most of the proteins used to quantify signaling pathway activity was inhibited by RL1, only the phosphorylated S6 marker was not inhibited in NCH644 (Figure 2a,b). We thus confirmed a dual inhibition of RL1 in the mTORC1 and mTORC2 downstream pathway markers in GSCs.

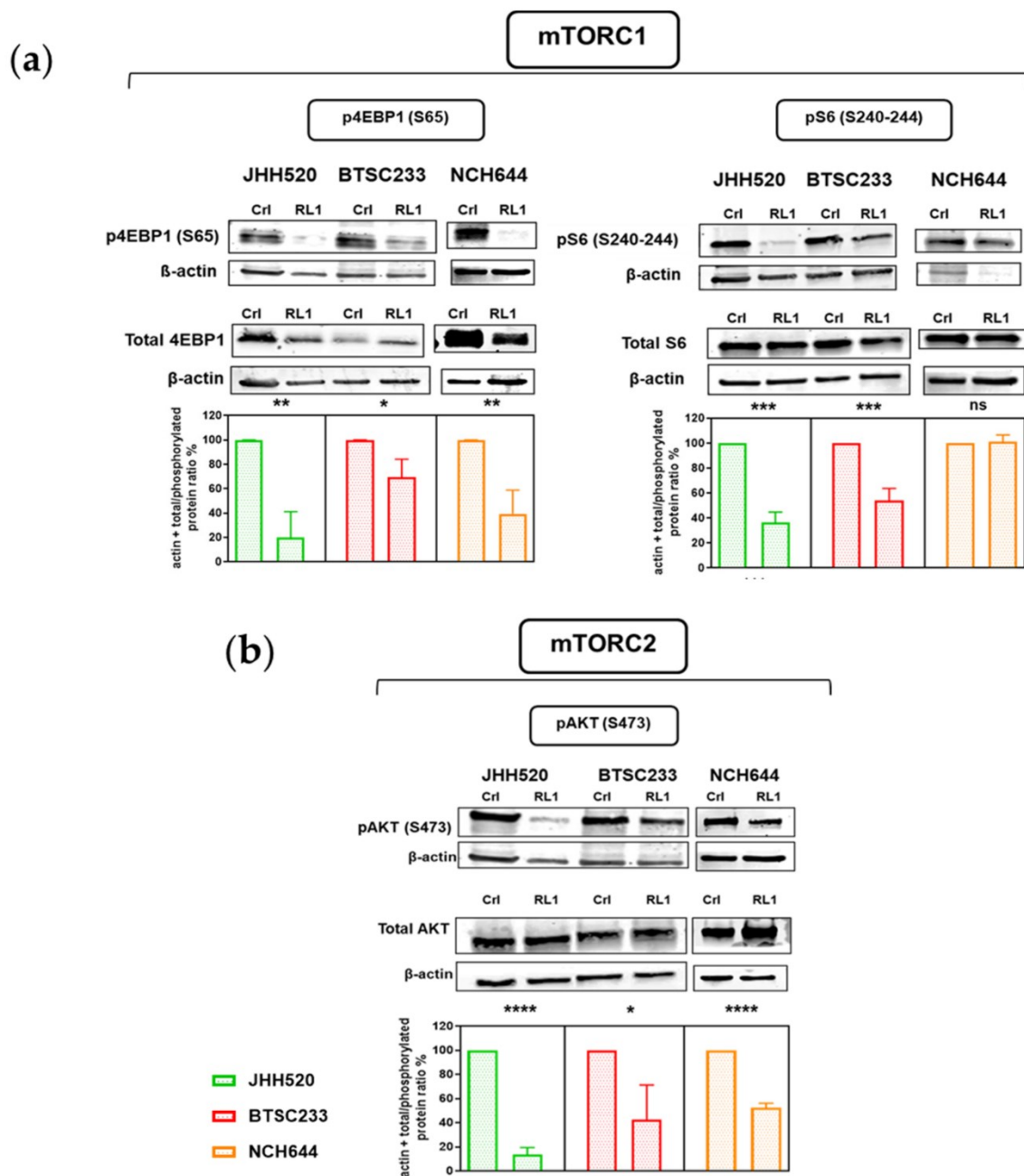


Figure 2. RL1 effect on mTOR signaling protein marker expression. RL1 protein expression analysis validates the inhibition of both (a) mTORC1 and (b) mTORC2 in our GSCs. Statistical tests performed for two variables with the unpaired Student’s t-test. The significance of the difference between groups was described as * $p < 0.05$, ** $p < 0.01$, *** $p < 0.001$, **** $p < 0.0001$.

2.3. RL1 Induces Cell Cycle Arrest, Apoptosis, and Proliferation Inhibition

After determining that the cell growth and mTOR pathway inhibition capacity of RL1 extends to GSCs, we aimed to further characterize the mode of action of this therapy. There was a significant cell cycle arrest in the G0/G1 phase of all models (Figure 3a), corroborating a clear antimitotic effect.

In parallel, there was a slight increase of apoptosis in all the cell lines as an additional effect, but this was only statistically significant in the NCH644 and BTSC233 lines (Figure 3b). In line with this, there was a significant decrease in proliferation for all the tested cell lines (Figure 3c).

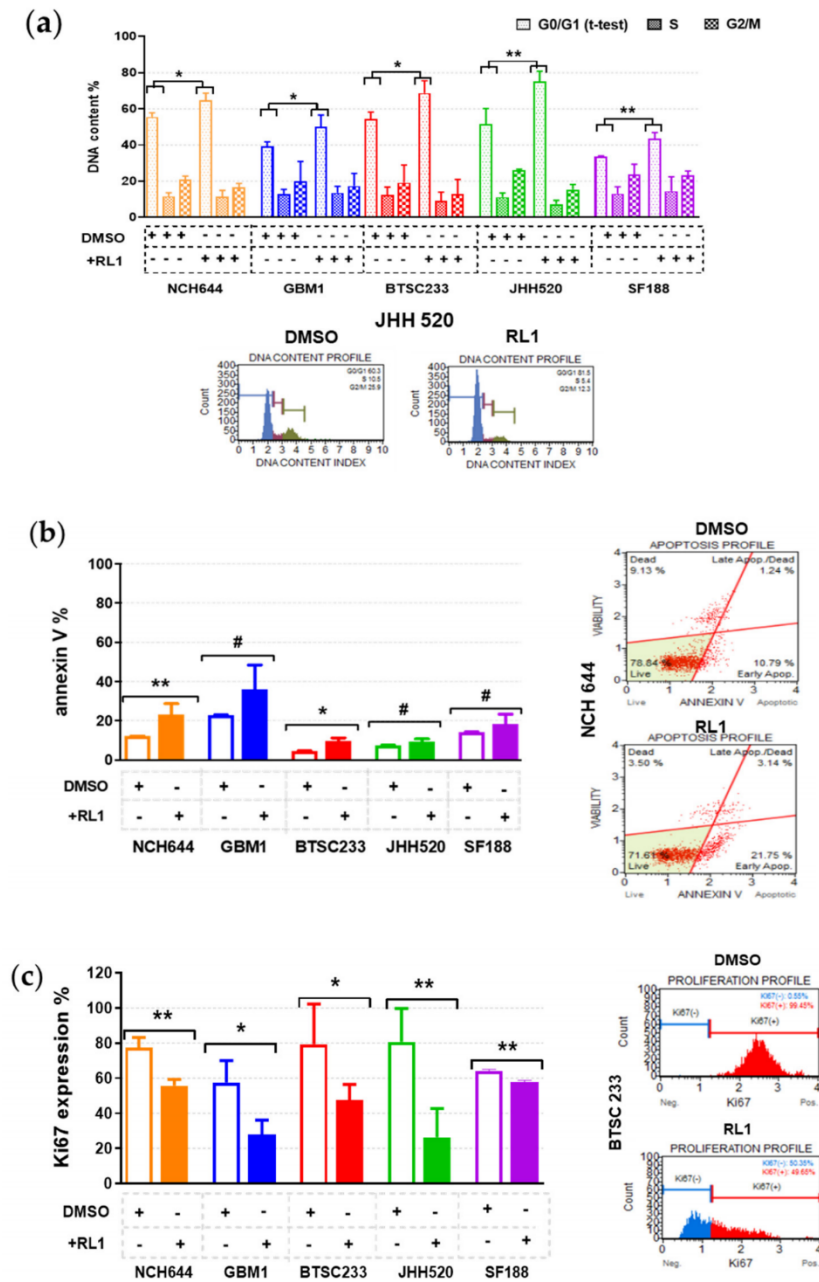


Figure 3. RL1 mechanistic effects. (a) Cell cycle arrest in the G0/G1 phase of all the models given DNA content %, (b) small apoptosis increase in all cell lines only statistically significant in NCH644 and BTSC233, with numerical increase in the other cell lines, (c) significant decrease in GSC proliferation given by Ki67% expression. Statistical tests performed for two variables with the unpaired Student’s *t*-test. The significance of the difference between groups was described as * $p < 0.05$, ** $p < 0.01$, # numerical-nonsignificant.

2.4. RL1 Inhibits Stemness and EMT

Since we identified a wide functional effect of RL1 on our GSCs, we sought to probe for the effects on markers indicating stem cell properties. We chose the validated neural stem cell markers, CD133 and SOX2, and the mesenchymal transformation markers CD44 and ZEB1 and quantified their total protein abundance. We could not observe all markers in all of our models. CD133 and SOX2 were suppressed by RL1 in NCH644, BTSC233, and JHH520; while CD44 expression was reduced by the

same drug in MES BTSC233 and JHH520, the only cell models that were found positive for this protein (Figure 4a). Phenotypically, the ability to form GSC colonies was strongly and significantly inhibited in all cell lines by RL1 (Figure 4b). The master EMT transcription-factor marker ZEB1 was inhibited by RL1 in the BTSC233 and JHH520 MES-type models, but not in PN NCH644 (Figure 4a). The indication of suppressed EMT was phenotypically supported by the fact that RL1 treatment strongly inhibited cellular migration in all cell lines except NCH644, which after several attempts continued to form consolidated neuro-spheres before undergoing migration (Figure 4c).

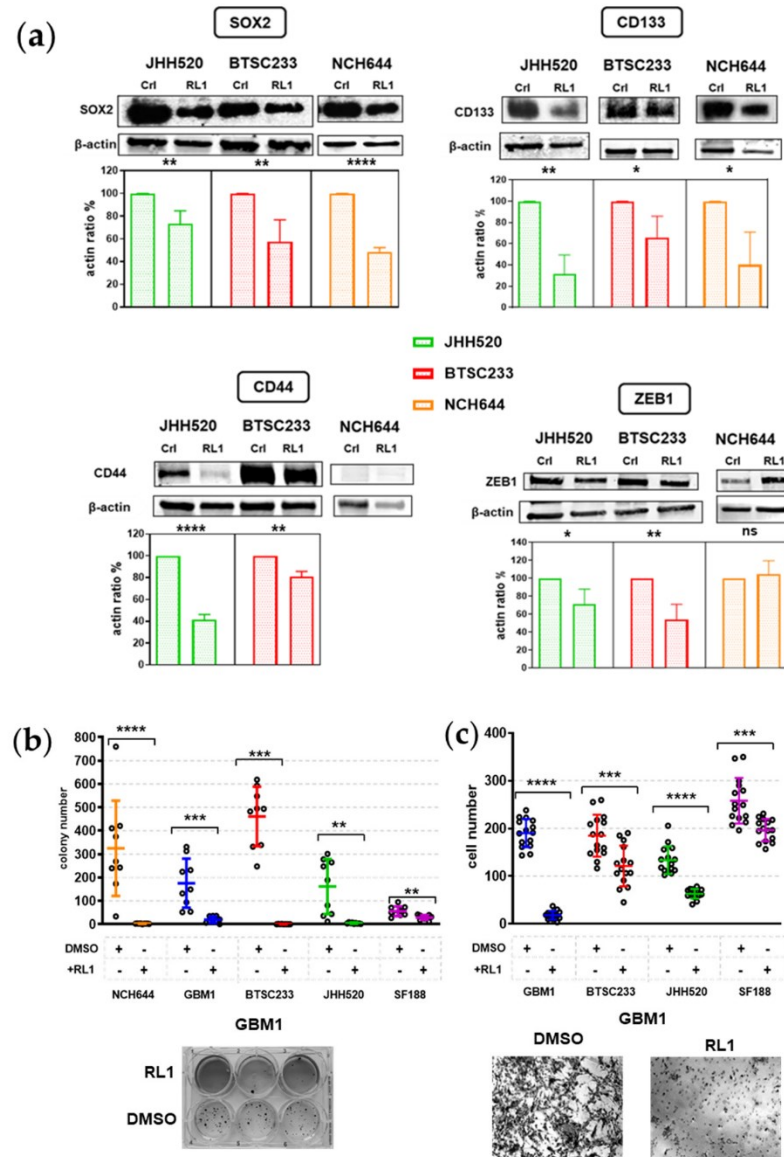


Figure 4. RL1 effect on stemness and EMT protein marker expression. (a) RL1 protein expression analysis validates the inhibition of neural stem cell markers and mesenchymal transformation markers in our GSCs, (b) RL1 strongly inhibited colony formation in all GSCs in agar assays, (c) RL1 strongly inhibited migration in all cell lines except NCH644 in Boyden chamber assays. Statistical tests performed for two variables, unpaired Student's *t*-test. The significance of the difference between groups was described as * $p < 0.05$, ** $p < 0.01$, *** $p < 0.001$, **** $p < 0.0001$.

2.5. Association between mTOR Biomarkers and EMT/Mesenchymal Markers Biosamples of GBM Patients of Western and Eastern Ethnicity

To probe for clinical relevance of our experimental data, we performed a data-mining analysis from established clinical cancer sample datasets. To this aim, we used an American cohort (The Cancer Genome Atlas, TCGA) and a Chinese cohort (Chinese Glioma Genome Atlas, CGGA) of patients. In our analysis, we put special emphasis on probing the potential correlation between the expression of two main mTOR signaling genes, namely *EIF4EBP1* (gene encoding 4EBP1) and *RPS6* (gene encoding S6), and one EMT marker, namely *ZEB1* as well as one mesenchymal marker, namely *ALDH1A3*, a recently identified marker for mesenchymal transformation in GBM [28]. We found that while *EIF4EBP1* and *ZEB1* expression were negatively correlated, even though minimally, in the American cohort, this was not observed in the Chinese dataset (Figure 5a,b). There was a significant positive correlation of *EIF4EBP1* and *ALDH1A3* mRNA expression levels in samples from Chinese patients, but not in the American dataset (Figure 5a,b). When analyzing the expression levels of *RPS6* in the same datasets, we found *RPS6* and *ZEB1* mRNA expression levels to be positively correlated in both cohorts (Figure 5c,d). While the expression levels of *ALDH1A3* was negatively correlated with *RPS6* in the American cohort, it was positively correlated with *RPS6* expression in samples from Chinese patients (Figure 5c,d).

Moreover, we verified our in silico analysis with primary GBM samples (pGBM) derived from surgical subjects of our institution. We tested the same relevant markers above-mentioned. We confirmed a high expression of the mTOR signaling pathway molecules in all of the samples. As for the phosphorylation defined proteins, the *RPS6* marker was widely activated, in contrast to *EIF4EBP1*, which was clearly phosphorylated in four samples (pGBM#2, pGBM#4, pGBM#8, pGBM#9). Correlating *ZEB1* activity, the samples pGBM#2 and pGBM#4 featuring the highest *ZEB1* activity showed a clear correlation of *ZEB1* with mTOR activity, whereas pGBM#1, pGBM#5, and pGBM#6 had a mild correlation between mTOR activity and EMT.

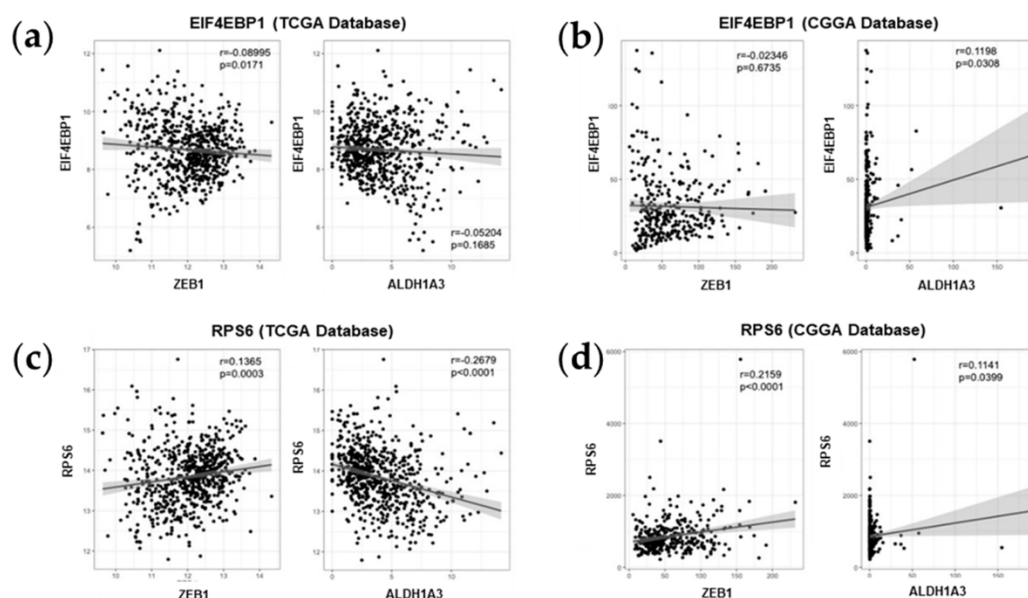


Figure 5. Cont.

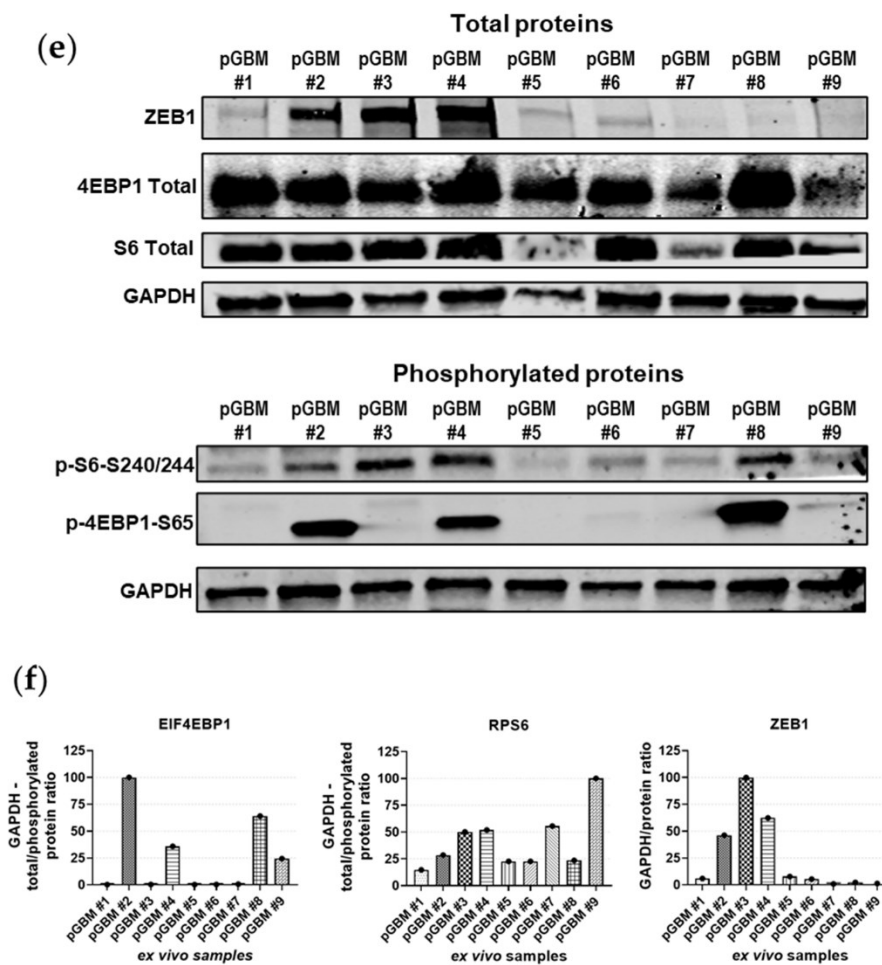


Figure 5. Bio-informatic in silico analysis. (a) TCGA *EIF4EBP1* mRNA data, (b) CGGA *EIF4EBP1* mRNA data, (c) TCGA *RPS6* mRNA data, (d) CGGA *RPS6* mRNA data, (a–d) the graphs were organized from left to right as *ZEB1* and *ALDH1A3*, (e) protein expression on surgical samples, (f) all proteins are normalized to loading control (GADPH), for *EIF4EBP1* and *RPS6* the ratio between total protein and phosphorylated form are calculated. The significance of the difference between the groups of data was analyzed by unpaired T test.

2.6. TTFIELDS, RL1, and TMZ Synergistically Reduced Cell Growth

Finally, given the recent advances in the clinic in treating GBM [7,13,28], we included experimental TTFIELDS therapy and TMZ treatment in our study. To identify the IC_{50} of TMZ of our models, we performed the cell growth assays under a range of TMZ treatment concentrations for up to six days (Table 1, Figure 6, Figure S1). This data correlates well with previous literature reports and MGMT promoter methylation characteristics of the respective models with SF188 (the only model with unmethylated MGMT promoter status) having the second lowest IC_{50} . The fast ability to form spheres may have increased the treatment resistance of the NCH644 model, which had the lowest IC_{50} .

For TTFIELDS, we applied the clinically relevant field frequency of 200 kHz. With our setup, we thus achieved a field intensity of 1.7 V/cm RMS. We then assessed growth on cells under different treatment conditions to probe for any combinational effects when combining RL1 with the clinical treatment scenarios using the Chou–Talalay method [29]. Our treatment setup can be found in Table 2.

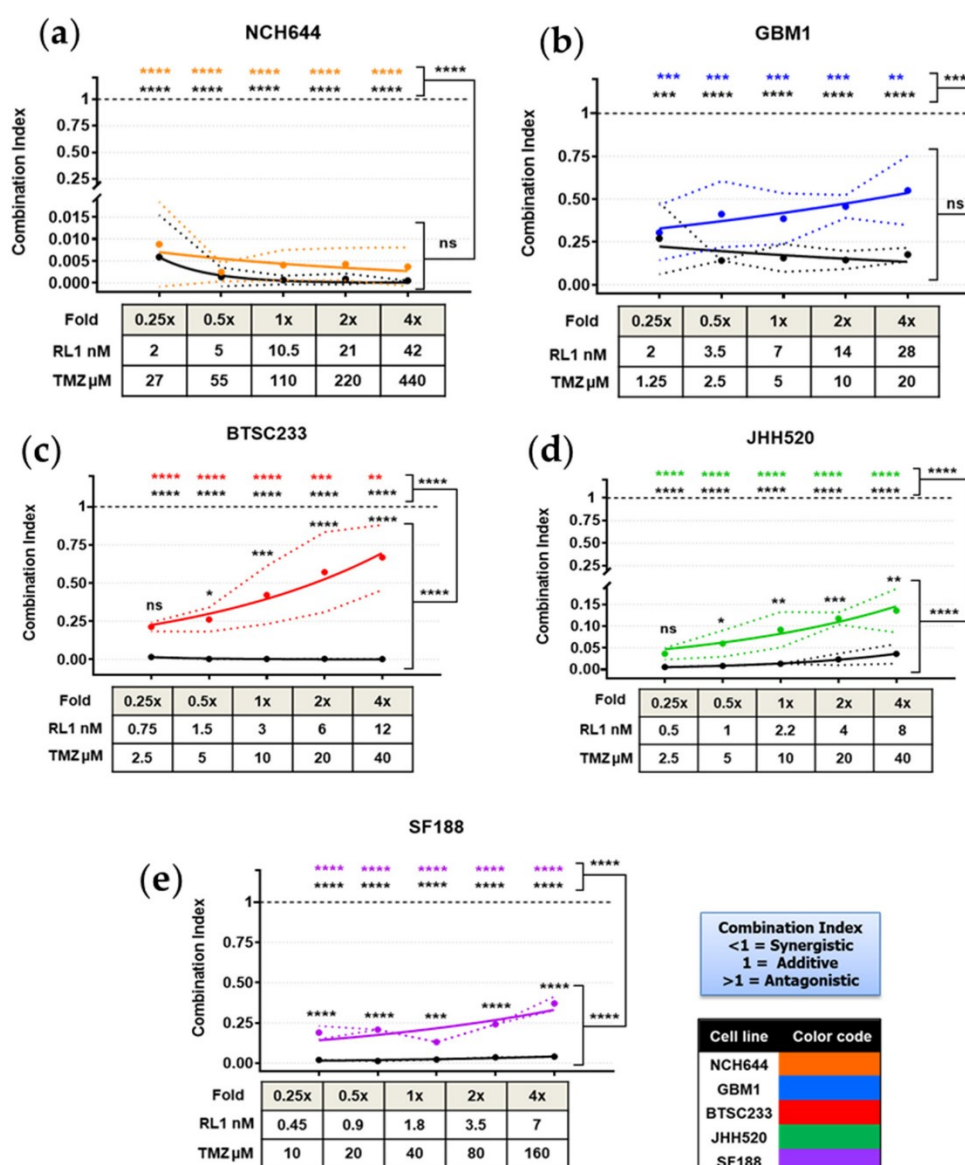


Figure 6. Synergistic effect of RL1, TMZ, and TTFIELDS. (a–e) All color coded GSCs according to RL1 IC₅₀ value showed a significant synergistic effect when combining RL1 with TMZ (colored lines), and an increased significant synergistic effect when adding TTFIELDS to the combination. Under each figure, there is a small table with the multiplication fold values of RL1 and TMZ. The statistical test performed was one-way-ANOVA. The significance of the difference between groups was described as * $p < 0.05$, ** $p < 0.01$, *** $p < 0.001$, **** $p < 0.0001$.

Table 2. Experimental setup for combination treatment study.

Dish Configuration	Value	Drug	Concentration
Frequency	200 kHz	IC ₅₀ folds of RL1	0.25x, 0.5x, 1x, 2x, 4x Plus DMSO control.
Temperature	37 °C		
Current	12 mA	IC ₅₀ folds of TMZ	0.25x, 0.5x, 1x, 2x, 4x Plus DMSO control.
Voltage	1.7 V/cm RMS	Combined IC ₅₀ folds of TMZ and RL1 in ascending order	0.25 + 0.25, 0.5 + 0.5, 1 + 1, 2 + 2, 4 + 4 Plus DMSO control.
Incubation Time	All 48 h BTSC233 96 h		

A 48-h incubation was an adequate time frame to induce a synergistic dose dependent effect in all the cell lines and groups, except for BTSC233, which required 96 h of incubation in order to show significant synergistic combination index (CI) values -CI < 1 referring to synergism, CI = 1 to additive effect and CI > 1 to antagonism-. NCH644, which was up to this point the most resistant GSC against both RL1 and TMZ, showed the most potent synergistic effect CI < 0.02 p < 0.0001 with a tendency of increased CI proportional to the drug concentrations applied, as opposed to the rest of the cell lines, which showed opposite curve directions. Despite this effect, the additional TTFIELDS treatment showed a numerically enhanced, non-significant synergistic CI effect. The cell line JHH520, showed the second most potent synergistic effect of TMZ and RL1 with values CI < 0.2 p < 0.0001, which was significantly strengthened by the TTFIELDS treatment. The cell line GBM1 had a more discrete but significant drug combination synergy with CI values lower than 0.75 p < 0.0001, however, TTFIELDS treatment showed a numerical, non-significantly stronger synergistic CI effect. For the other cell lines, namely SF188 (CI values < 0.5) and BTSC233 (CI values < 0.9), the synergistic effect was significant, both for the drugs alone (p < 0.0001) and stronger with the addition of TTFIELDS treatment (p < 0.0001). Our data strongly indicate a synergistic therapeutic potential for RL1 on GSCs when combined with TTFIELDS and TMZ. The TTFIELDS synergy bioassay results showing synergism can be found in Figure 6a–e.

3. Discussion

mTOR is a key player in the activation of cell growth, reprogramming of cell metabolism, and structural cytoskeleton remodeling, amongst many others [30]. In the context of cancer, many projects have been conducted dedicated to developing inhibition strategies to effectively block the activation of mTOR signaling activity [31], with some promising clinical trials underway [32]. Additionally, in the context of brain tumors, targeting mTOR activation is considered a potent therapeutic avenue [15,33]. However, given the complex nature of this signaling pathway comprising two molecular distinct signaling branches, enabling the compensation of signal loss from either of the two [30], it is generally accepted that clinically relevant anti-mTOR directed therapies will have to block the entire pathway [34] to avoid the emergence of therapy resistance [31].

In this regard, recent development in campaigns aimed to generate dual mTOR complex inhibitors [22,35] and their functional validation in experimental trials has raised hopes in advancing our ability to treat lethal cancers. By choosing the most promising last generation mTOR inhibitor drug candidate, termed Rapalink1, our study sought to validate its effects on state-of-the-art disease models of the disease. Rapalink1 has previously been shown to effectively penetrate the blood brain barrier and brain parenchyma of the rodent model of brain tumor [22]. We now extend the evidence of the potential of this drug candidate to possess effective anti-cancer stem cell effects and to potentiate clinical approved treatments, at least in vitro. Although we applied 3D organoid-like in vitro models of the disease, future animal studies, especially incorporating the animal setup of TTF, are required to unequivocally postulate the therapeutic relevance of our findings. Of note, our initial off target characterization assay using non cancer cell models indicated that RL1 possesses a higher therapeutic index on cancer cells, supporting this drug substance for further oncology studies.

Our results clearly demonstrated the potency of this drug candidate to be able block stem cell markers and properties including migration and clonogenicity in GBM. The soft agar assay was chosen because of our group's previous experience using reduction of sphere formation as well as the reduction of protein abundance of stem cell markers such as ZEB1, as a biomarker combination to indicate the blockade of stem cell phenotype in our disease models [36,37]. Interestingly, we found that the strongest drug effects were seen in the most aggressive cell models of the MES subtype, a subtype with the worst clinical prognosis for overall survival of the patients [38], and more moderate effects in the PN cell model, further advocating this drug candidate to be particularly useful for targeting the highest malignant cell population in GBM. Concordantly, the correlations of mTOR signaling regulating cell cycle [39,40], stemness/EMT [18,30,41], and cellular survival [42] are generally accepted and our results are well in line with those high-profile papers. Thus, together with the translational focus of our study

to test the promising drug candidate in a clinical-near experimental setting, our data proved solid ground for mode of action characterization of RL1 on GSCs featuring efficient target suppression, consequently blocking stemness/EMT.

Next, we performed a confirmatory *in silico* study to probe for the clinical relevance of mTOR and EMT biomarkers in large scale molecular datasets of clinical samples from cohorts of different genders and ethnicities. We identified a tendency of direct correlation between the expression of the mTOR gene *RPS6* and the expression of the mesenchymal marker *ZEB1* in two different cohorts (TCGA and CGGA cohorts), suggesting a link between the mTOR pathway and EMT in GBM patient samples. This is in line with a previous study identifying the mTOR pathway as a prognostic gene set in the MES subtype [43]. The results of our drug validation and patient sample studies are in line with the work of others that have identified mTOR signaling as a promoter of EMT and stemness in various diseases as well as in normal development [19]. Furthermore, previous recent work of others have already identified the existence of an mTOR-ZEB1 signaling axis in GBM using various functional attempts, which we now confirm in the context of a therapeutic relevant pharmacological *in vitro* model [44–46]. Together with our correlative assays of transcript and protein abundancy in patient samples, we hypothesize that the mTOR-ZEB1 axis extends to GSCs, but seems differentially aberrant amongst individual GBM cases. However, in all tested cases, RL1 provides an efficient option to effectively reduce their activation, leading to desired anti-cancer cell effects.

After corroborating an antimitotic and partially apoptotic effect of RL1 on GSCs, known to be highly resistant to standard clinical treatments [47], we wanted to see if RL1 can augment the effectivity of clinical GBM treatments. We executed detailed combination treatment studies *in vitro* featuring RL1, BSC chemotherapeutic agent TMZ as well as TTFields. The widely used drug combination effect method described by Chou and Talalay [29] was chosen to guide our experimental design and the quantification of results to identify any potentiating effects. Applying *in vitro*™ settings that mimic the TTFields therapy used in the clinical setting, we found a synergistic anti-cell growth effect when combining RL1 with TMZ and TTFields. Follow up testing *in vivo*, using the recently launched animal system for TTFields, *in vivo*™, will now need to be done to validate the therapeutic potential of this treatment regime. Nevertheless, given the previously described therapeutic effect of RL1 in animal models of human GBM [22], we believe that our results already support the consideration of this treatment option from a clinician-scientist point of view.

It was demonstrated that the binding of RL1 to the factor termed FKBP12 is required to inhibit mTOR activity and to mediate the anti-proliferative effect of Rapalink1 [22,48]. Therefore, it is highly likely that the effect of Rapalink1 on stemness and EMT markers as well as its synergy with tumor treating fields requires FKBP12. Since FKBP12 has not been proven as a clinically relevant marker, this may be a relevant approach for further studies.

In summary, we used our diverse stem cell *in vitro* platform to perform mode of action analysis and initial risk assessment of a novel drug candidate, and interrogated clinical treatment options to benchmark its therapeutic potential in combination regimes. We used clinical specimens from ethnic and gender diverse backgrounds to validate our experimental findings to benchmark relevance.

4. Materials and Methods

4.1. Cell Culture, Fresh Patient Samples, and Pharmacologic Substances

The *in vitro* cell models used were kindly provided as follows, glioblastoma neuro-spheres JHH520 (G. Riggins, Johns Hopkins, Baltimore, MD, USA); SF188 (E. Raabe, Johns Hopkins, Baltimore, MA, USA); BTSC233 (M.S. Carro, Freiburg University, Freiburg im Breisgau, Germany); NCH644 (C. Herold-Mende, Heidelberg University, Heidelberg, Germany); and GBM1 (A. Vescovi, San Raffaele Hospital, Milano, Italy). Ethical approval for the use of cell models to study brain cancer biology was from the ethical commission of the medical faculty of Heinrich-Heine University (study ID 5841R). Cortical fetal neural stem cells were collected from human fetal cortical tissue grown in a neurosphere

condition (ethical vote Study ID #5206). Induced neural stem cells were differentiated from the human iPSC line IMR 90/4 (WiCell, Madison, WI, USA), as previously described [49].

The primary GBM tumor samples were derived from the operation room of the department of neurosurgery (Düsseldorf, Germany) and were snap-frozen in liquid nitrogen until the preparation of lysates. All subjects gave their informed consent for inclusion before their participation in the study. The study was conducted in accordance with the Declaration of Helsinki, and the protocol was approved by the Ethics Committee of the Medical Faculty of the Heinrich-Heine University of Duesseldorf (#2019-484-FmB).

All cells were grown in complete serum-free suspension media enriched with bovine fibroblast growth factor (Peprotech, Rocky Hill, NJ, USA) and human epidermal growth factor (Peprotech), as previously described [50]. These were incubated under standard conditions (SCs, humidified 37 °C, 5% carbon dioxide (CO₂)). Cells were regularly tested for mycoplasma accumulation and authenticity using the short tandem repeat assay, as previously described [51]. Rapalink-1 was purchased from Apexbio Technology (Houston, TX USA) and TMZ (Sigma-Aldrich, St. Louis, MO, USA). Both were resuspended in a DMSO (dimethyl sulfoxide, Sigma-Aldrich) vehicle, according to their molecular weight and the manufacturer's instructions, after which we further diluted them to the required concentrations and stored them at −20 °C.

4.2. Cell Growth (MTT Assay)

Cell growth of the different models was assessed using the MTT (3-(4,5-dimethylthiazol-2-yl) 2,5-diphenyl tetrazolium bromide; Sigma Aldrich) assay and plating 3000 cells per well in technical triplicates of 100 µL growth-media each in clear-96-well plates (Corning Inc., Corning, NY, USA). On each plate, we included a respective cell control triplicate (media, cells, and DMSO < 1%) and a blank control (media, no cells) to normalize the cell growth and background reading. We tested RL1 at the following concentrations of 1.5, 6, 12, 24, and 48 nM. For TMZ, 5, 10, 25, 50, and 100 µM. Cells were then incubated with RL1, initially over six days, then finally over four days in SCs. In parallel, for TMZ, this was done for six days in SCs. Starting from day 0 and then every other day (days 2, 4, or 6), we measured the MTT absorbance values as follows: we added 10% of MTT reagent per well, incubated the cells in SCs for three hours, verified the formation of crystals under bright field microscope, and finally lysed the cells by incubating them with HCl-isopropanol-TritonX for 10 min. The resulting relative absorbance was finally measured with the Paradigm micro-plate reader (Molecular Devices LLC, San Jose, CA, USA). All experiments were done in three independent biological repetitions before statistical analysis and IC₅₀ calculations.

4.3. Tumor Treating Fields

The in vitro™ preclinical laboratory research system dishes (Novocure, Saint Helier, Jersey) were plated in parallel to the 35 mm cell culture dishes and similarly contained 40,000 cells in 2 mL of complete media per plate. Using the previously calculated IC₅₀; different multiplication folds of drug concentrations were applied to each condition in the in vitro™ dishes as follows:

- IC₅₀ fold of RL1 (0.25×, 0.5×, 1×, 2×, 4×) plus DMSO control.
- IC₅₀ fold of TMZ (0.25, 0.5, 1, 2, 4) plus DMSO control.
- Combined IC₅₀ folds of TMZ and RL1 in ascending order (0.25 + 0.25, 0.5 + 0.5, 1 + 1, 2 + 2, 4 + 4) plus DMSO control.

Immediately after, they were treated with TTFields (1.7 V/cm RMS) via the in vitro™ system by using perpendicular pairs of transducers insulated by a high dielectric constant ceramic. TTFields were applied for 48 h (except BTSC233 with 96-h treatment) at a frequency of 200 kHz, the optimal frequency established clinically for glioblastoma patients at final temperature of 37 °C, in a humidified incubator with 5% CO₂.

In parallel, identically plated non-TTFields control 35 mm cell culture dishes were incubated in SCs. All dishes/plates/conditions had an equal DMSO concentration of less than 1%.

After 48 h of treatment or incubation, the different cell lines were re-plated in clear 96-well-plates and processed as described above for the MTT assays. All experiments were done using three independent biological repetitions before statistical analysis.

4.4. Synergy Assays

The CI, based on the unified theory of the median effect equation, was calculated using the Chou method, as previously described [36,52] using the CompuSyn Software® (ComboSyn Inc., Paramus, NJ, USA). The software algorithm defined as $CI < 1$ referring to synergism, $CI = 1$ to additive effect, and $CI > 1$ to antagonism.

The significance of the synergistic effect of all treatments was calculated compared to the additive effect ($CI = 1$), using the resulting CI values of each triplicate. The closer to $CI = 0$, the stronger the synergy, and the closer to $CI = 1$ or >1 , the lower the synergism. Using this, the significance of the RL1 effect compared to TMZ was calculated comparing the resulting CI values of each combination.

4.5. Flow Cytometry–Muse© Assays

Using the Muse © Cell Analyzer Flow Cytometer device (Merck, Darmstadt, Germany) as previously described [53], we tested apoptosis assays with the Annexin V & Dead Cell Kit (Luminex, TX, USA), proliferation assays with the Ki67 Proliferation Kit (Luminex), and the cell cycle assay with the Cell Cycle Kit (Luminex), according to the manufacturer's protocols. All kits used a 7aad fluorophore marker. All assays were performed after 48 h, in order to have an earlier drug effect incubation, with the previously calculated IC_{50} drug concentration, in independent biological triplicates.

4.6. Migration–Boyden Chamber Assay

Assessment of the cellular migration was performed using a modified 24-well Boyden Chamber assay similar to the invasion assay described before [50], but without coating, in order to determine the migration effect. 75,000 cells were suspended in 500 μ L of DMEM and placed on top of each insert membrane (Life Technologies, Carlsberg, CA, USA). The bottom was filled with 700 μ L DMEM media containing 10% fetal calf serum. All Boyden chamber assays were analyzed 14 h after cell plating. The upper side of the membrane was then wiped with a moist PBS (phosphate-buffered saline) cotton swab to remove the remaining plated cells. The membrane was then fixed at -20 °C with methanol for 15 min and stained with hematoxylin. The invasion of the cells was evaluated by counting the cell nuclei on the lower side of the membrane under a bright field microscope, counting five random high-power fields per insert in three independent biological repetitions. The migrated cells were quantified using ImageJ software (National Institutes of Health, Maryland, USA), before statistical analysis.

4.7. Clonogenicity–Colony Formation Assay

To evaluate the clonogenic capacity of our cell models, we performed a colony formation assay in soft agarose as described previously [37]. Clear six-well plates (Corning Inc.) were initially coated with a bottom layer of 1.5 mL of 1% agarose (Life Technologies) and complete media, then incubated for at least 1 h at room temperature. Afterward, a 2 mL layer of 0.6% agarose with 5000 cell per well was plated for all cells except SF188, which required 10,000 cells per well to generate clear clones. It was then covered with an additional 2 mL of fresh media, which was changed every three days. After three weeks, colonies were stained with 1 mg/mL 4-nitro blue tetrazolium chloride (NBT) solution (Sigma-Aldrich), and incubated overnight in SCs; three independent biological repetitions were performed before the colonies were quantified using Clono-Counter software [54], and the statistical analysis was performed. This assay was established to functionally verify the stem cell properties of our cell models [37,55].

4.8. Protein Expression–Western Blot

Western blotting was done as previously described [50]; antibodies were used as per the manufacturer's instructions (for specifications, see Table S1 and Figure S2. Western blots membranes). The total protein content of each cell line was extracted using RIPA Buffer, then determined colorimetrically using the DC Protein Assay Kit (Bio-Rad, Hercules, CA, USA), according to the manufacturer's instructions, and measured with the Paradigm micro-plate reader. Primary antibodies (as reported in Supplementary Table S1) were incubated overnight at 4° on a rocking platform. Secondary antibodies (goat-anti-rabbit, IRDye800CW LI-COR #926-32211; goat-anti-mouse, IRDye680RD LI-COR #926-68070; goat anti-rabbit-HRP, Jackson Immuno Research #111-035-144; all 1/10,000) were incubated for 1 h at room temperature. All antibodies were diluted in blocking solution containing either 5% bovine serum albumin (BSA) for phosphorylated proteins, or 5% milk powder for the rest of the non-phosphorylated proteins; both diluted in Tris-buffered saline with Tween20 (TBST). For the phospho-proteins, we used a BSA blocking agent that allowed clear bands, since albumin tends to not be phosphorylated; and we normalized the resulting inhibited proteins with the total non-phosphorylated corresponding mTORC1 and mTORC2 markers. Signals were detected using either a film-based system by applying a Super Signal West Pico Chemiluminescent Substrate (Thermo Scientific) or a luminescence-based system in a LI-COR Odyssey CLx Imager (LI-COR). Densitometry quantification was done either with the supplied software from LI-COR or ImageJ software for the films. Experiments were performed using three independent biological repetitions before statistical analysis.

4.9. Bio-Informatic Analysis

Transcriptome sequencing data and clinical data of glioma patients were obtained from the CGGA (Chinese Glioma Genome Atlas) database (<https://www.cgga.org.cn>) and TCGA (The Cancer Genome Atlas Program) database (<https://tcgadata.nci.nih.gov>). For stemness, we tested the ALDH1A3 in order to complement the limited reports of this marker in the published literature. For EMT, we explored the master transcription factor ZEB1. The statistical computations and figure drawing were performed with R package 'ggplot2'.

The data used from CGGA were approved by the Beijing Tiantan Hospital Institutional Review Board and tumor specimen quality control.

4.10. Statistical Analysis

All graphs and analyses were calculated with Prism GraphPad 8 software (San Diego, CA, USA) except for the bioinformatics analysis, which was performed with the R package above-mentioned. The media control absorbance value average was rested from all wells. The average absorbance value of every DMSO-vehicle-control cell containing wells was used as the control for normalization. IC₅₀ values were calculated using a logarithmic nonlinear regression formula in the aforementioned software. The performed statistical tests depended on the related variables; for two variables, the unpaired Student's *t*-test, and for more than two related variables, one-way-ANOVA was applied. All plots present the mean and standard deviation. The *p*-value < 0.05 was considered statistically significant in all analysis. The significance of the difference between groups was described as * *p* < 0.05, ** *p* < 0.01, *** *p* < 0.001, **** *p* < 0.0001.

5. Conclusions

We validated the therapeutic potential of RL1 against GBM using advanced human stem cell disease modeling technology and identified its synergistic effect potency when combined with TTFields and TMZ, two of the main clinically approved treatment options for this disease. By showing fewer toxic effects on non-cancer stem cells, we validated our platform technology to be of benefit for drug development and for projects that assess the risk of substances applied in experimental or clinical

contexts. Given the previous report on the effectiveness of RL1 in animal models of human GBM, our results support clinical trials of RL1 in patients with GBM.

Supplementary Materials: The following are available online at <http://www.mdpi.com/2072-6694/12/12/3859/s1>, Figure S1: TMZ cell growth and IC₅₀; Figure S2: Western blots membranes. Table S1: Western blot antibody concentrations.

Author Contributions: Conceptualization, U.D.K., and A.V.-T.; Methodology, A.V.-T.; Software, A.V.-T.; Bio-informatic analysis, W.Z., G.L. (Guanzhang Li), and A.V.-T.; mTOR/4EBP1 support, G.L. (Gabriel Leprivier); Validation, A.V.-T., A.-C.N., and U.D.K.; Formal analysis, A.V.-T.; Investigation, A.V.-T.; Resources, U.D.K., R.A.B., M.S., D.H., H.-J.S., and E.F.; Data curation, U.D.K.; Writing—original draft preparation, A.V.-T.; Writing—review and editing, M.A.K., S.M., and all authors; Visualization, All authors; Supervision, U.D.K.; Project administration, U.D.K.; Funding acquisition, U.D.K., D.H., and H.-J.S. All authors have read and agreed to the published version of the manuscript.

Funding: Andres Vargas-Toscano is supported by the German Catholic Academic Exchange Service (KAAD). The work of Ulf Dietrich is supported by the Federal Ministry of Education and Research (BMBF KZ 03VP03791), the VolkswagenStiftung, the Hempel Family Foundation, the Brigitte-and Konstanze Wegener Foundation, and the Sino-German Center for Science Promotion and EU COST CA17140. We acknowledge the funding support from the European Association of Neurosurgical Sciences and Forschungskommission of the Medical Faculty of the University of Düsseldorf to SM. The collection of some of the human fetal tissue was supported by an NIH grant to the Cambridge Biomedical Research Center and the WT-MRC funded Cambridge Stem Cell Institute. The authors have no other relevant affiliations or financial involvement with any organization or entity with a financial interest in or financial conflicts with the subject matter or materials discussed in the manuscript apart from those disclosed.

Acknowledgments: The authors acknowledge Guido Reifenberger, Constanze Uhlmann, Michael Hewera, Renfei Du (Heinrich-Heine University Düsseldorf), Xiaoling He (University of Cambridge), Huda Abdullah, and Moshe Giladi (Novocure) for kindly providing technical assistance.

Conflicts of Interest: The authors declare no conflict of interest. The funders had no role in the design of the study; in the collection, analyses, or interpretation of data; in the writing of the manuscript, or in the decision to publish the results.

References

1. Tonn, J.-C.; Reardon, D.A.; Rutka, J.T.; Westphal, M. (Eds.) *Oncology of CNS Tumors*; Springer: Cham, Switzerland, 2019; ISBN 978-3-030-04151-9.
2. Stupp, R.; Hegi, M.E.; Mason, W.P. Effects of radiotherapy with concomitant and adjuvant temozolomide versus radiotherapy alone on survival in glioblastoma in a randomised phase III study: 5-year analysis of the EORTC-NCIC trial. *Lancet Oncol.* **2009**, *10*, 8. [[CrossRef](#)]
3. Tabatabai, G.; Stupp, R.; van den Bent, M.J.; Hegi, M.E.; Tonn, J.C.; Wick, W.; Weller, M. Molecular diagnostics of gliomas: The clinical perspective. *Acta Neuropathol.* **2010**, *120*, 585–592. [[CrossRef](#)]
4. Singh, S.K.; Hawkins, C.; Clarke, I.D.; Squire, J.A.; Bayani, J.; Hide, T.; Henkelman, R.M.; Cusimano, M.D.; Dirks, P.B. Identification of human brain tumour initiating cells. *Nature* **2004**, *432*, 396–401. [[CrossRef](#)]
5. Guardia, G.D.A.; Correa, B.R.; Araujo, P.R.; Qiao, M.; Burns, S.; Penalva, L.O.F.; Galante, P.A.F. Proneural and mesenchymal glioma stem cells display major differences in splicing and lncRNA profiles. *NPJ Genomic Med.* **2020**, *5*, 2. [[CrossRef](#)]
6. Kahlert, U.D.; Nikkhah, G.; Maciaczyk, J. Epithelial-to-mesenchymal (-like) transition as a relevant molecular event in malignant gliomas. *Cancer Lett.* **2013**, *331*, 131–138. [[CrossRef](#)]
7. Stupp, R.; Weller, M.; Belanger, K.; Bogdahn, U.; Ludwin, S.K.; Lacombe, D.; Mirimanoff, R.O. Radiotherapy plus Concomitant and Adjuvant Temozolomide for Glioblastoma. *N. Engl. J. Med.* **2005**, *352*, 987–996. [[CrossRef](#)]
8. Brennan, C.W.; Verhaak, R.G.W.; McKenna, A.; Campos, B.; Nounshmehr, H.; Salama, S.R.; Zheng, S.; Chakravarty, D.; Sanborn, J.Z.; Berman, S.H.; et al. The Somatic Genomic Landscape of Glioblastoma. *Cell* **2013**, *155*, 462–477. [[CrossRef](#)]
9. Machado, L.E.; Alvarenga, A.W.; da Silva, F.F.; Roffé, M.; Begnami, M.D.; Torres, L.F.B.; da Cunha, I.W.; Martins, V.R.; Hajj, G.N.M. Overexpression of mTOR and p(240–244)S6 in IDH1 Wild-Type Human Glioblastomas Is Predictive of Low Survival. *J. Histochem. Cytochem.* **2018**, *66*, 403–414. [[CrossRef](#)]

10. Verhaak, R.G.W.; Hoadley, K.A.; Purdom, E.; Wang, V.; Qi, Y.; Wilkerson, M.D.; Miller, C.R.; Ding, L.; Golub, T.; Mesirov, J.P.; et al. Integrated Genomic Analysis Identifies Clinically Relevant Subtypes of Glioblastoma Characterized by Abnormalities in PDGFRA, IDH1, EGFR, and NF1. *Cancer Cell* **2010**, *17*, 98–110. [[CrossRef](#)] [[PubMed](#)]
11. Wang, Q.; Hu, B.; Hu, X.; Kim, H.; Squatrito, M.; Scarpacci, L.; deCarvalho, A.C.; Lyu, S.; Li, P.; Li, Y.; et al. Tumor Evolution of Glioma-Intrinsic Gene Expression Subtypes Associates with Immunological Changes in the Microenvironment. *Cancer Cell* **2017**, *32*, 42–56.e6. [[CrossRef](#)] [[PubMed](#)]
12. Stupp, R.; Wong, E.T.; Kanner, A.A.; Steinberg, D.; Engelhard, H.; Heidecke, V.; Kirson, E.D.; Taillibert, S.; Liebermann, F.; Dbalý, V.; et al. NovoTTF-100A versus physician's choice chemotherapy in recurrent glioblastoma: A randomised phase III trial of a novel treatment modality. *Eur. J. Cancer* **2012**, *48*, 2192–2202. [[CrossRef](#)] [[PubMed](#)]
13. Stupp, R.; Taillibert, S.; Kanner, A.; Read, W.; Steinberg, D.M.; Lhermitte, B.; Toms, S.; Idbaih, A.; Ahluwalia, M.S.; Fink, K.; et al. Effect of Tumor-Treating Fields Plus Maintenance Temozolomide vs. Maintenance Temozolomide Alone on Survival in Patients with Glioblastoma: A Randomized Clinical Trial. *JAMA* **2017**, *318*, 2306. [[CrossRef](#)] [[PubMed](#)]
14. Wang, Y.; Pandey, M.; Ballo, M.T. Integration of Tumor-Treating Fields into the Multidisciplinary Management of Patients with Solid Malignancies. *Oncologist* **2019**, *24*. [[CrossRef](#)] [[PubMed](#)]
15. Wick, W.; Dettmer, S.; Berberich, A.; Kessler, T.; Karapanagiotou-Schenkel, I.; Wick, A.; Winkler, F.; Pfaff, E.; Brors, B.; Debus, J.; et al. N2M2 (NOA-20) phase I/II trial of molecularly matched targeted therapies plus radiotherapy in patients with newly diagnosed non-MGMT hypermethylated glioblastoma. *Neuro Oncol.* **2019**, *21*, 95–105. [[CrossRef](#)] [[PubMed](#)]
16. Wick, W.; Gorlia, T.; Bady, P.; Platten, M.; Taphoorn, M.J.B.; Steuve, J.; Brandes, A.A.; Hamou, M.-F.; Wick, A.; Kosch, M.; et al. Phase II Study of Radiotherapy and Temozolomide versus Radiochemotherapy with Temozolomide in Patients with Newly Diagnosed Glioblastoma without MGMT Promoter Hypermethylation. *Clin. Cancer Res.* **2016**, *22*, 4797–4806. [[CrossRef](#)] [[PubMed](#)]
17. Lamouille, S.; Connolly, E.; Smyth, J.W.; Akhurst, R.J.; Derynck, R. TGF-induced activation of mTOR complex 2 drives epithelial-mesenchymal transition and cell invasion. *J. Cell Sci.* **2012**, *125*, 1259–1273. [[CrossRef](#)] [[PubMed](#)]
18. Katsuno, Y.; Meyer, D.S.; Zhang, Z.; Shokat, K.M.; Akhurst, R.J.; Miyazono, K.; Derynck, R. Chronic TGF- β exposure drives stabilized EMT, tumor stemness, and cancer drug resistance with vulnerability to bitopic mTOR inhibition. *Sci. Signal.* **2019**, *12*, eaau8544. [[CrossRef](#)]
19. Karimi Roshan, M.; Soltani, A.; Soleimani, A.; Rezaie Kakhkhaie, K.; Afshari, A.R.; Soukhtanloo, M. Role of AKT and mTOR signaling pathways in the induction of epithelial-mesenchymal transition (EMT) process. *Biochimie* **2019**, *165*, 229–234. [[CrossRef](#)]
20. Galanis, E.; Buckner, J.C.; Maurer, M.J.; Kreisberg, J.I.; Ballman, K.; Boni, J.; Peralba, J.M.; Jenkins, R.B.; Dakhil, S.R.; Morton, R.F.; et al. Phase II Trial of Temozolomide (CC-779) in Recurrent Glioblastoma Multiforme: A North Central Cancer Treatment Group Study. *J. Clin. Oncol.* **2005**, *23*, 5294–5304. [[CrossRef](#)]
21. Mecca, C.; Giambanco, I.; Donato, R.; Arcuri, C. Targeting mTOR in Glioblastoma: Rationale and Preclinical/Clinical Evidence. *Dis. Markers* **2018**, *2018*, 1–10. [[CrossRef](#)]
22. Fan, Q.; Aksoy, O.; Wong, R.A.; Ilkhanizadeh, S.; Novotny, C.J.; Gustafson, W.C.; Truong, A.Y.-Q.; Cayanan, G.; Simonds, E.F.; Haas-Kogan, D.; et al. A Kinase Inhibitor Targeted to mTORC1 Drives Regression in Glioblastoma. *Cancer Cell* **2017**, *31*, 424–435. [[CrossRef](#)] [[PubMed](#)]
23. Podergajs, N.; Brekka, N.; Radlwimmer, B.; Herold-Mende, C.; Talasila, K.M.; Tiemann, K.; Rajcevic, U.; Lah, T.T.; Bjerkvig, R.; Miletic, H. Expansive growth of two glioblastoma stem-like cell lines is mediated by bFGF and not by EGF. *Radiol. Oncol.* **2013**, *47*, 330–337. [[CrossRef](#)]
24. Galli, R.; Binda, E.; Orfanelli, U.; Cipelletti, B.; Gritti, A.; De Vitis, S.; Fiocco, R.; Foroni, C.; Dimeco, F.; Vescovi, A. Isolation and characterization of tumorigenic, stem-like neural precursors from human glioblastoma. *Cancer Res.* **2004**, *64*, 7011–7021. [[CrossRef](#)] [[PubMed](#)]
25. Fedele, V.; Dai, F.; Masilamani, A.P.; Heiland, D.H.; Kling, E.; Gätjens-Sanchez, A.M.; Ferrarese, R.; Platania, L.; Soroush, D.; Kim, H.; et al. Epigenetic Regulation of ZBTB18 Promotes Glioblastoma Progression. *Mol. Cancer Res. MCR* **2017**, *15*, 998–1011. [[CrossRef](#)] [[PubMed](#)]

26. Binder, Z.A.; Wilson, K.M.; Salmasi, V.; Orr, B.A.; Eberhart, C.G.; Siu, I.-M.; Lim, M.; Weingart, J.D.; Quinones-Hinojosa, A.; Bettegowda, C.; et al. Establishment and Biological Characterization of a Panel of Glioblastoma Multiforme (GBM) and GBM Variant Oncosphere Cell Lines. *PLoS ONE* **2016**, *11*, e0150271. [[CrossRef](#)] [[PubMed](#)]
27. Wilson, K.M.; Mathews-Griner, L.A.; Williamson, T.; Guha, R.; Chen, L.; Shinn, P.; McKnight, C.; Michael, S.; Klumpp-Thomas, C.; Binder, Z.A.; et al. Mutation Profiles in Glioblastoma 3D Oncospheres Modulate Drug Efficacy. *SLAS Technol. Transl. Life Sci. Innov.* **2019**, *24*, 28–40. [[CrossRef](#)] [[PubMed](#)]
28. National Comprehensive Cancer Network. Central Nervous System Cancers (Version 1.2016). Available online: <https://www.nccn.org/patients/guidelines/content/PDF/brain-gliomas-patient.pdf> (accessed on 16 October 2020).
29. Chou, T.-C. Drug Combination Studies and Their Synergy Quantification Using the Chou-Talalay Method. *Cancer Res.* **2010**, *70*, 440–446. [[CrossRef](#)]
30. Meng, D.; Frank, A.R.; Jewell, J.L. mTOR signaling in stem and progenitor cells. *Development* **2018**, *145*, dev152595. [[CrossRef](#)]
31. Duzgun, Z.; Eroglu, Z.; Biray Avcı, C. Role of mTOR in glioblastoma. *Gene* **2016**, *575*, 187–190. [[CrossRef](#)]
32. Magaway, C.; Kim, E.; Jacinto, E. Targeting mTOR and Metabolism in Cancer: Lessons and Innovations. *Cells* **2019**, *8*, 1584. [[CrossRef](#)]
33. Munster, P.; Mita, M.; Mahipal, A.; Nemunaitis, J.; Massard, C.; Mikkelsen, T.; Cruz, C.; Paz-Ares, L.; Hidalgo, M.; Rathkopf, D.; et al. First-In-Human Phase I Study of a Dual mTOR Kinase and DNA-PK Inhibitor (CC-115) in Advanced Malignancy. *Cancer Manag. Res.* **2019**, *11*, 10463–10476. [[CrossRef](#)] [[PubMed](#)]
34. Chiarini, F.; Evangelisti, C.; Lattanzi, G.; McCubrey, J.A.; Martelli, A.M. Advances in understanding the mechanisms of evasive and innate resistance to mTOR inhibition in cancer cells. *Biochim. Biophys. Acta BBA Mol. Cell Res.* **2019**, *1866*, 1322–1337. [[CrossRef](#)] [[PubMed](#)]
35. Fan, Q.W.; Nicolaidis, T.P.; Weiss, W.A. Inhibiting 4EBP1 in Glioblastoma. *Clin. Cancer Res. Off. J. Am. Assoc. Cancer Res.* **2018**, *24*, 14–21. [[CrossRef](#)] [[PubMed](#)]
36. Koch, K.; Hartmann, R.; Schröter, F.; Suwala, A.K.; Maciaczyk, D.; Krüger, A.C.; Willbold, D.; Kahlert, U.D.; Maciaczyk, J. Reciprocal regulation of the cholinic phenotype and epithelial-mesenchymal transition in glioblastoma cells. *Oncotarget* **2016**, *7*, 73414–73431. [[CrossRef](#)]
37. Kahlert, U.D.; Suwala, A.K.; Koch, K.; Natsumeda, M.; Orr, B.A.; Hayashi, M.; Maciaczyk, J.; Eberhart, C.G. Pharmacologic Wnt Inhibition Reduces Proliferation, Survival, and Clonogenicity of Glioblastoma Cells. *J. Neuropathol. Exp. Neurol.* **2015**, *74*, 889–900. [[CrossRef](#)]
38. Fedele, M.; Cerchia, L.; Pegoraro, S.; Sgarra, R.; Manfioletti, G. Proneural-Mesenchymal Transition: Phenotypic Plasticity to Acquire Multitherapy Resistance in Glioblastoma. *Int. J. Mol. Sci.* **2019**, *20*, 2746. [[CrossRef](#)]
39. Fingar, D.C.; Richardson, C.J.; Tee, A.R.; Cheatham, L.; Tsou, C.; Blenis, J. mTOR controls cell cycle progression through its cell growth effectors S6K1 and 4E-BP1/eukaryotic translation initiation factor 4E. *Mol. Cell. Biol.* **2004**, *24*, 200–216. [[CrossRef](#)]
40. Fingar, D.C.; Salama, S.; Tsou, C.; Harlow, E.; Blenis, J. Mammalian cell size is controlled by mTOR and its downstream targets S6K1 and 4EBP1/eIF4E. *Genes Dev.* **2002**, *16*, 1472–1487. [[CrossRef](#)]
41. Kwasnicki, A.; Jeevan, D.; Braun, A.; Murali, R.; Jhanwar-Uniyal, M. Involvement of mTOR signaling pathways in regulating growth and dissemination of metastatic brain tumors via EMT. *Anticancer Res.* **2015**, *35*, 689–696.
42. Hung, C.-M.; Garcia-Haro, L.; Sparks, C.A.; Guertin, D.A. mTOR-dependent cell survival mechanisms. *Cold Spring Harb. Perspect. Biol.* **2012**, *4*. [[CrossRef](#)]
43. Park, A.K.; Kim, P.; Ballester, L.Y.; Esquenazi, Y.; Zhao, Z. Subtype-specific signaling pathways and genomic aberrations associated with prognosis of glioblastoma. *Neuro Oncol.* **2019**, *21*, 59–70. [[CrossRef](#)] [[PubMed](#)]
44. Chen, W.; Kong, K.-K.; Xu, X.-K.; Chen, C.; Li, H.; Wang, F.-Y.; Peng, X.-F.; Zhang, Z.; Li, P.; Li, J.-L.; et al. Downregulation of miR-205 is associated with glioblastoma cell migration, invasion, and the epithelial-mesenchymal transition, by targeting ZEB1 via the Akt/mTOR signaling pathway. *Int. J. Oncol.* **2018**, *52*, 485–495. [[CrossRef](#)] [[PubMed](#)]
45. Zhang, L.; Zhang, W.; Li, Y.; Alvarez, A.; Li, Z.; Wang, Y.; Song, L.; Lv, D.; Nakano, I.; Hu, B.; et al. SHP-2-upregulated ZEB1 is important for PDGFR α -driven glioma epithelial-mesenchymal transition and invasion in mice and humans. *Oncogene* **2016**, *35*, 5641–5652. [[CrossRef](#)] [[PubMed](#)]

46. Song, Y.; Chen, Y.; Li, Y.; Lyu, X.; Cui, J.; Cheng, Y.; Zhao, L.; Zhao, G. Metformin inhibits TGF- β 1-induced epithelial-to-mesenchymal transition-like process and stem-like properties in GBM via AKT/mTOR/ZEB1 pathway. *Oncotarget* **2018**, *9*, 7023–7035. [[CrossRef](#)]
47. Lathia, J.D.; Mack, S.C.; Mulkearns-Hubert, E.E.; Valentim, C.L.L.; Rich, J.N. Cancer stem cells in glioblastoma. *Genes Dev.* **2015**, *29*, 1203–1217. [[CrossRef](#)]
48. Rodrik-Outmezguine, V.S.; Okaniwa, M.; Yao, Z.; Novotny, C.J.; McWhirter, C.; Banaji, A.; Won, H.; Wong, W.; Berger, M.; de Stanchina, E.; et al. Overcoming mTOR resistance mutations with a new-generation mTOR inhibitor. *Nature* **2016**, *534*, 272–276. [[CrossRef](#)]
49. Fritsche, E.; Tigges, J.; Hartmann, J.; Kapr, J.; Serafini, M.M.; Viviani, B. Neural In Vitro Models for Studying Substances Acting on the Central Nervous System. *Handb. Exp. Pharmacol.* **2020**. [[CrossRef](#)]
50. Kahlert, U.D.; Suwala, A.K.; Raabe, E.H.; Siebzehnrubl, F.A.; Suarez, M.J.; Orr, B.A.; Bar, E.E.; Maciaczyk, J.; Eberhart, C.G. ZEB1 Promotes Invasion in Human Fetal Neural Stem Cells and Hypoxic Glioma Neurospheres: ZEB1 Regulates Motility in Hypoxic Gliomas. *Brain Pathol.* **2015**, *25*, 724–732. [[CrossRef](#)]
51. Kahlert, U.D.; Cheng, M.; Koch, K.; Marchionni, L.; Fan, X.; Raabe, E.H.; Maciaczyk, J.; Glunde, K.; Eberhart, C.G. Alterations in cellular metabolome after pharmacological inhibition of Notch in glioblastoma cells. *Int. J. Cancer* **2016**, *138*, 1246–1255. [[CrossRef](#)]
52. Suwala, A.K.; Koch, K.; Rios, D.H.; Aretz, P.; Uhlmann, C.; Ogorek, I.; Felsberg, J.; Reifenberger, G.; Köhrer, K.; Deenen, R.; et al. Inhibition of Wnt/beta-catenin signaling downregulates expression of aldehyde dehydrogenase isoform 3A1 (ALDH3A1) to reduce resistance against temozolomide in glioblastoma in vitro. *Oncotarget* **2018**, *9*, 22703–22716. [[CrossRef](#)]
53. Vargas-Toscano, A.; Khan, D.; Nickel, A.-C.; Hewera, M.; Kamp, M.A.; Fischer, I.; Steiger, H.-J.; Zhang, W.; Muhammad, S.; Hänggi, D.; et al. Robot technology identifies a Parkinsonian therapeutics repurpose to target stem cells of glioblastoma. *CNS Oncol.* **2020**, *9*, CNS58. [[CrossRef](#)] [[PubMed](#)]
54. Niyazi, M.; Niyazi, I.; Belka, C. Counting colonies of clonogenic assays by using densitometric software. *Radiat. Oncol.* **2007**, *2*, 4. [[CrossRef](#)] [[PubMed](#)]
55. Koch, K.; Hartmann, R.; Tsiampali, J.; Uhlmann, C.; Nickel, A.-C.; He, X.; Kamp, M.A.; Sabel, M.; Barker, R.A.; Steiger, H.-J.; et al. A comparative pharmaco-metabolomic study of glutaminase inhibitors in glioma stem-like cells confirms biological effectiveness but reveals differences in target-specificity. *Cell Death Discov.* **2020**, *6*, 20. [[CrossRef](#)] [[PubMed](#)]

Publisher’s Note: MDPI stays neutral with regard to jurisdictional claims in published maps and institutional affiliations.



© 2020 by the authors. Licensee MDPI, Basel, Switzerland. This article is an open access article distributed under the terms and conditions of the Creative Commons Attribution (CC BY) license (<http://creativecommons.org/licenses/by/4.0/>).

Rapalink-1 Targets Glioblastoma Stem Cells and Acts Synergistically with Tumor Treating Fields to Reduce Resistance against Temozolomide

Andres Vargas-Toscano, Ann-Christin Nickel, Guanzhang Li, Marcel Alexander Kamp, Sajjad Muhammad, Gabriel Leprivier, Ellen Fritsche, Roger A. Barker, Michael Sabel, Hans-Jakob Steiger, Wei Zhang, Daniel Hänggi and Ulf Dietrich Kahlert

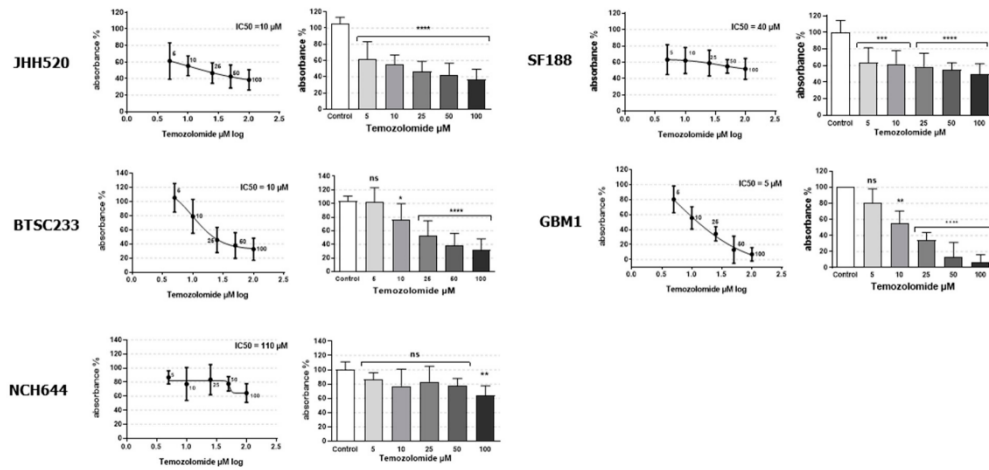
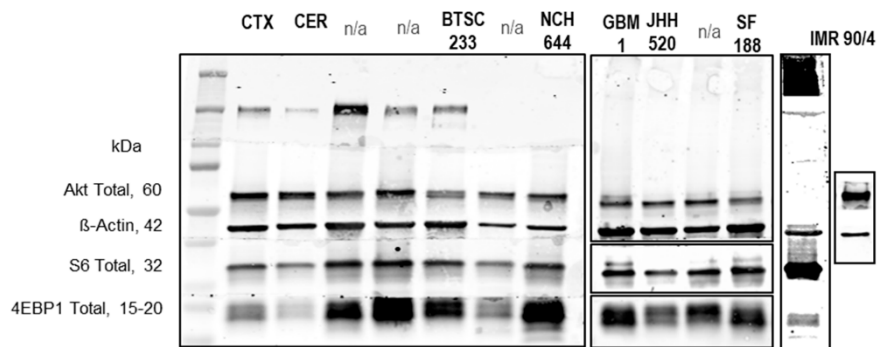


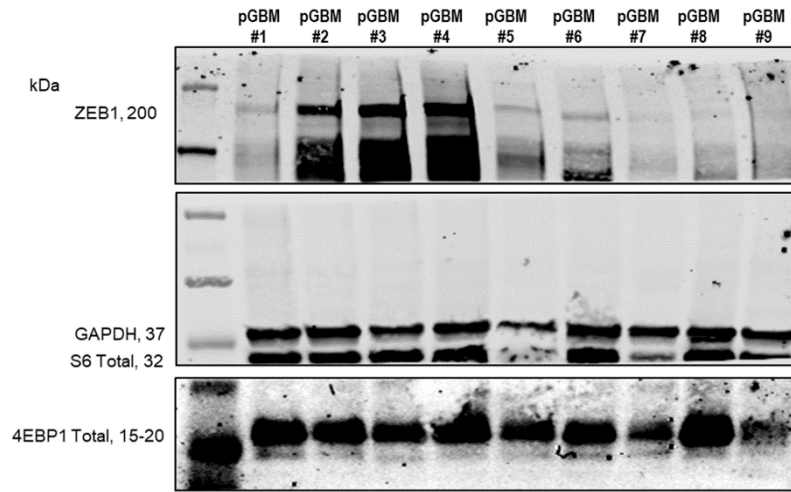
Figure S1. TMZ cell growth and IC50.



Multiple antibody screening

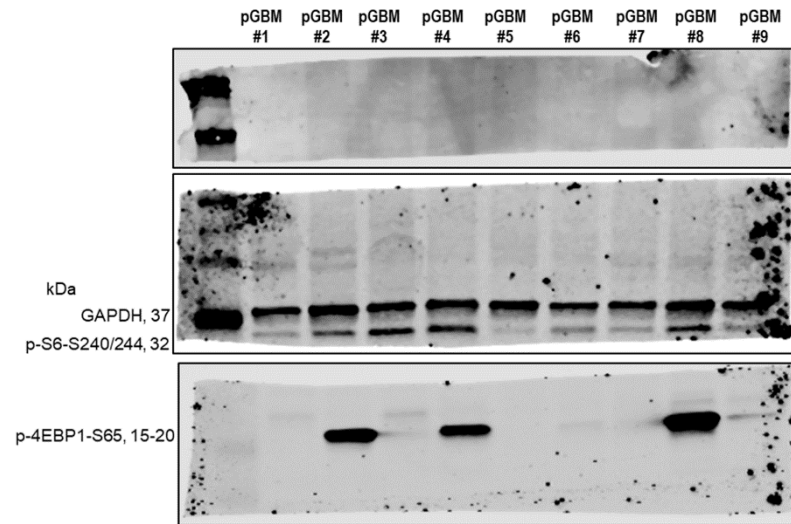
Immuno Blots visually analyzed before testing drug.

Part of the Figure 1(b)



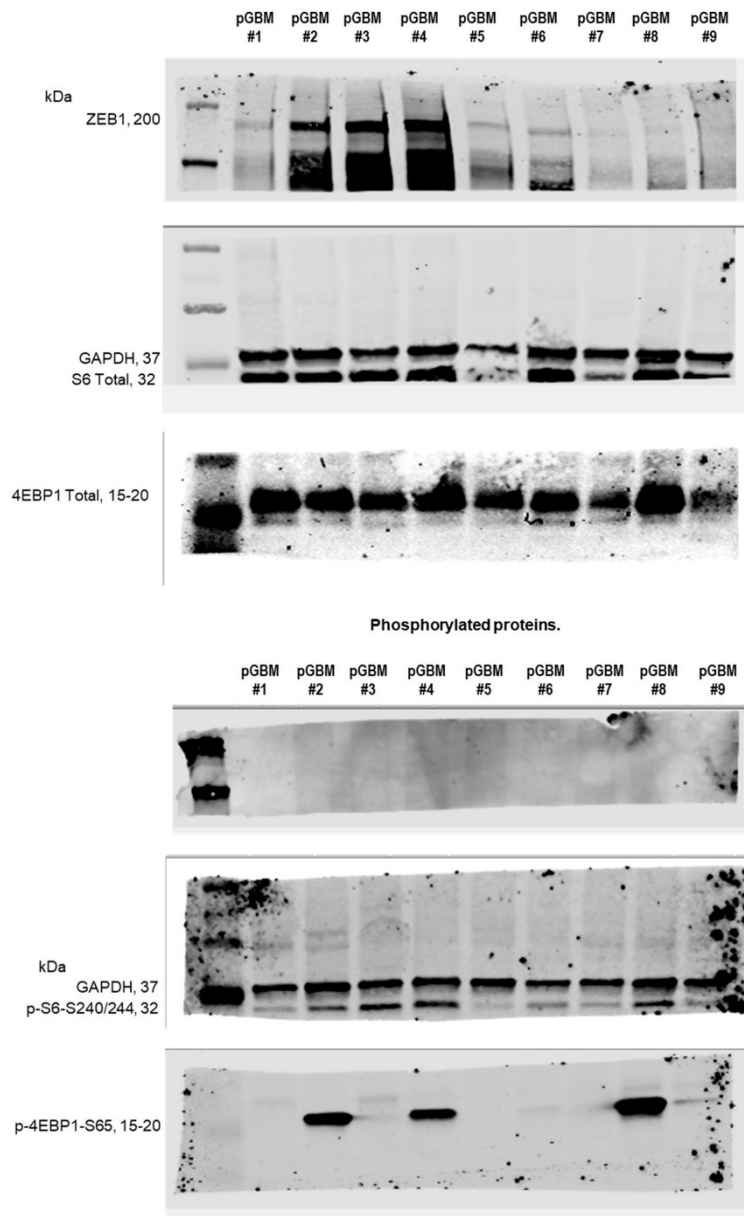
ex vivo tissue samples. Total Proteins.

Part of the Figure 5(e)



ex vivo tissue samples. Phosphorylated proteins.

Part of the Figure 5(e)



JHH520

JHH520 cell line

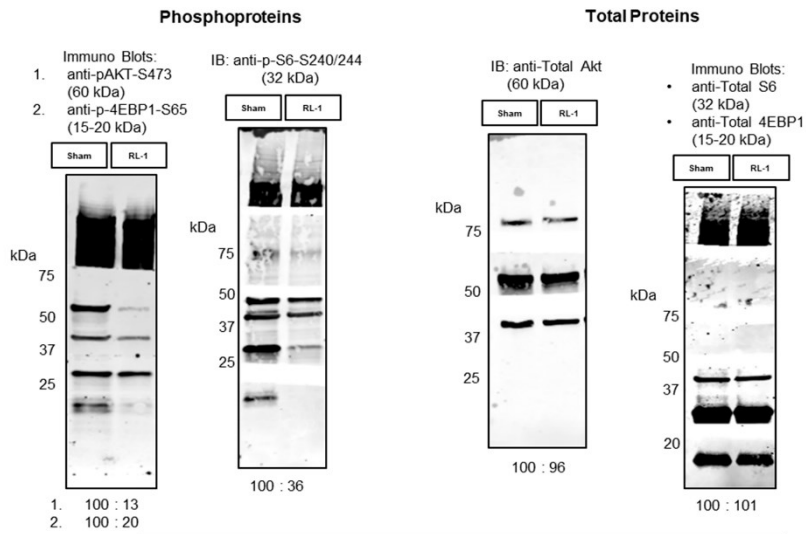


Figure 2a-b. RL1 effect on mTOR signaling protein marker expression.

JHH520 cell line

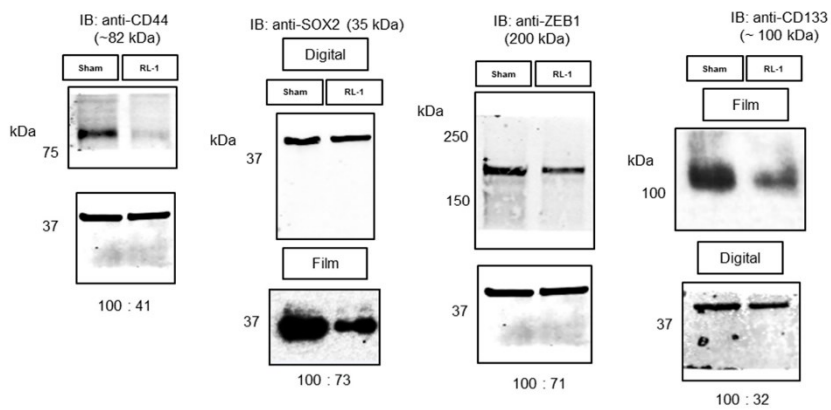


Figure 4a. RL1 effect on stemness and EMT protein marker expression.

BTSC233

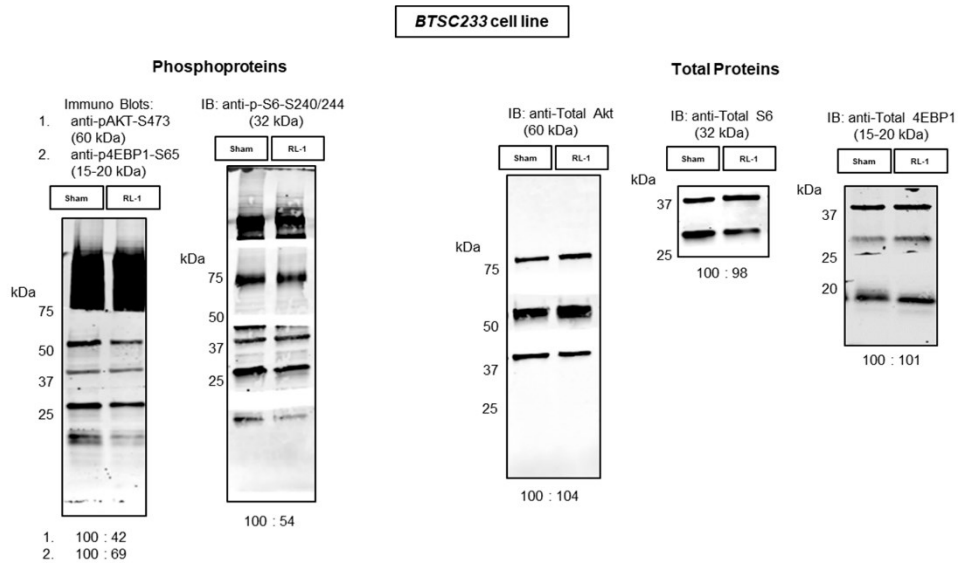


Figure 2a-b. RL1 effect on mTOR signaling protein marker expression.

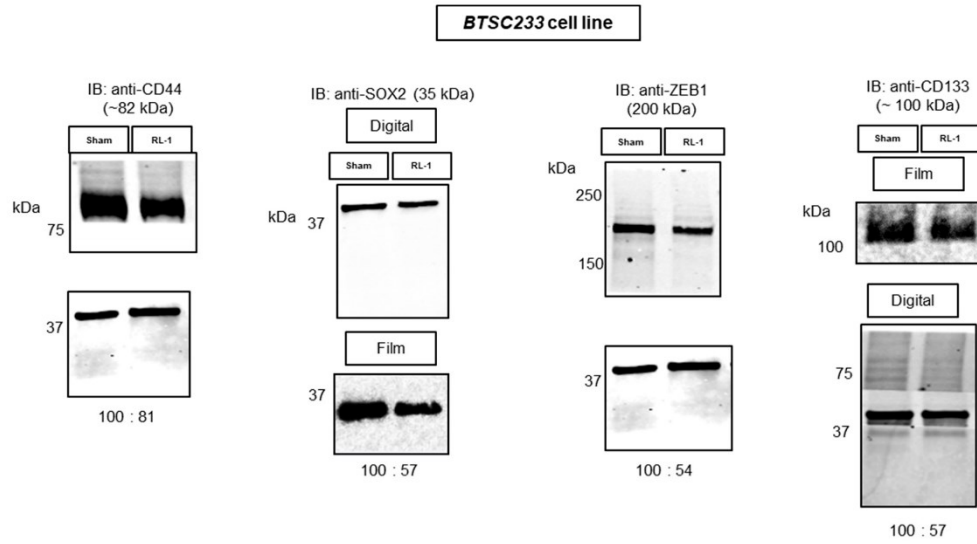


Figure 4a. RL1 effect on stemness and EMT protein marker expression.

NCH644

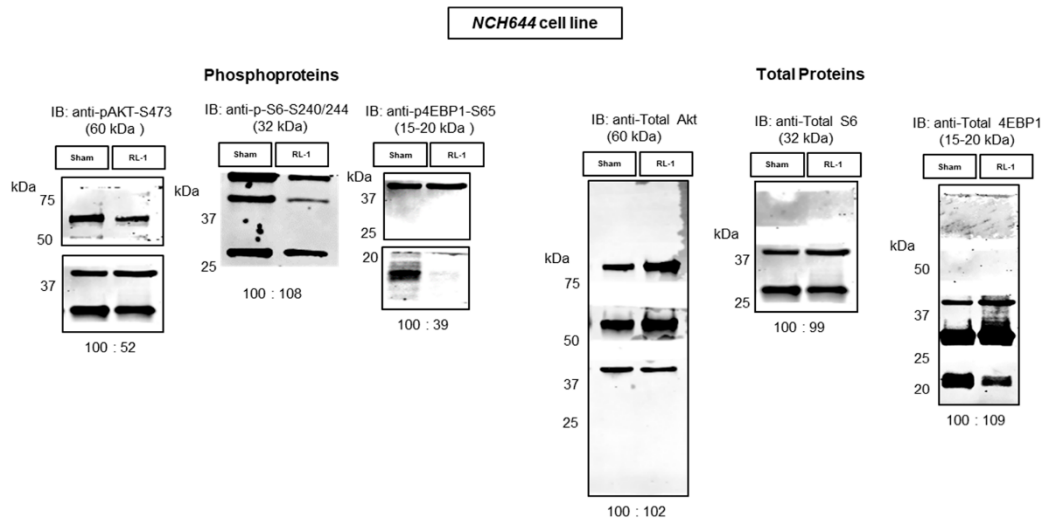


Figure 2a-b. RL1 effect on mTOR signaling protein marker expression.

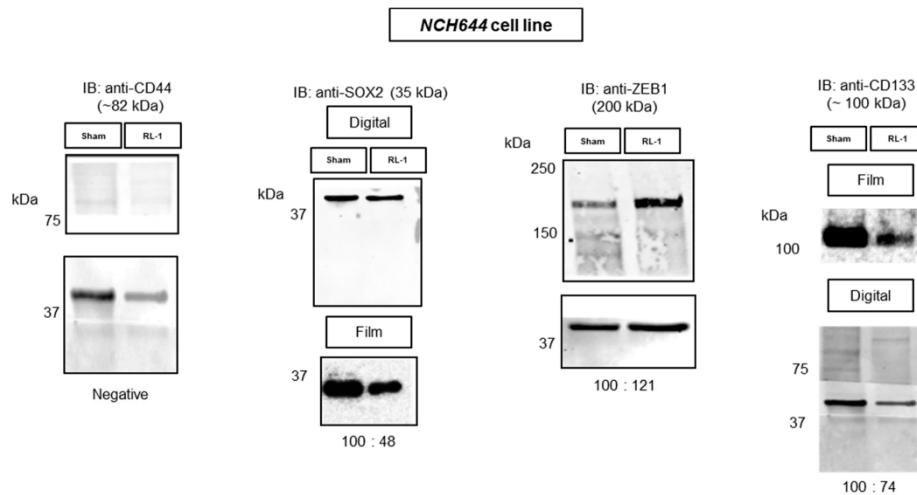


Figure 4a. RL1 effect on stemness and EMT protein marker expression.

Figure S2. Western blots membranes.

Relevant Notes: All bands were scanned digitally except otherwise written. Separate images were membranes that were cut physically before processing. Immuno Blots for the Screening of Figure 1b, were visually analysed without quantification before testing the drug (RL1). Quantified upon demand. Molecular weight estimation markers, performed with Precision Plus Protein™ Dual Color Standards, 500 µl # 1610374.

Table S1. Western blot antibody information.

Antibody	MW (kDa)	Brand	Catalog Number	Concentration	
p-4EBP1-S65	15-20	Cell Signaling Technology, Danvers, MA, USA	#9451	1:500	
Total 4EBP1	15-20		#9644	1:1000	
p-S6-S240/244	32		#2215	1:2000	
Total S6	32		#2217	1:2000	
p-Akt-S473	60		#9271	1:250	
Total Akt	60		#4691	1:1000	
Sox2	35		#L1D6A2	1:1000	
β -Actin	42		#4970	1:5000	
CD44	~82		#3570	1:100	
ZEB1	200		Sigma	#HPA027524	1:2000
CD133	~100		Miltenyi, Germany	#W6B3C1	1:100
GAPDH	~37		Proteintech	#60004-1-Ig	1:10000

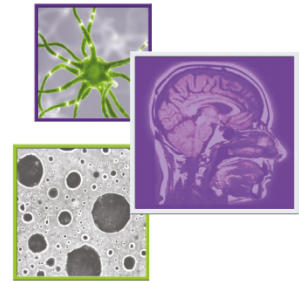


© 2020 by the author. Licensee MDPI, Basel, Switzerland. This article is an open access article distributed under the terms and conditions of the Creative Commons Attribution (CC BY) license (<http://creativecommons.org/licenses/by/4.0/>).



3. Paper 2 - Robot Technology Identifies a Parkinsonian Therapeutics Repurpose to Target Stem Cells of Glioblastoma. *Andres Vargas-Toscano, Dilaware Khan, Ann-Christin Nickel, Michael Hewera, Marcel Alexander Kamp, Igor Fischer, Hans-Jakob Steiger, Wei Zhang, Sajjad Muhammad, Daniel Hänggi and Ulf Dietrich Kahlert.* *CNS Oncology.* 9 no. 2: CNS58; Jun (2020)

The paper with supplementary data embedded in this chapter, was reprinted with the following considerations:

- Published in the year 2020 by the journal *CNS Oncology* from the publisher *Future Medicine*.
- It was adapted to the doctoral project with permission of Future Medicine Ltd, which allows the reprint of academic non-commercial Dissertations/Thesis, as detailed in the following webpage link:
<https://www.futuremedicine.com/reprints>
- The original publication is available under the journal webpage link:
<https://www.futuremedicine.com/doi/full/10.2217/cns-2020-0004>
- It can be accessed via PubMed under the following webpage link:
<https://pubmed.ncbi.nlm.nih.gov/32462934/>



Robot technology identifies a Parkinsonian therapeutics repurpose to target stem cells of glioblastoma

Andres Vargas-Toscano¹ , Dilaware Khan¹, Ann-Christin Nickel¹, Michael Hewera¹, Marcel Alexander Kamp¹, Igor Fischer¹, Hans-Jakob Steiger¹, Wei Zhang³, Sajjad Muhammad¹, Daniel Hänggi¹ & Ulf Dietrich Kahlert^{*1,2,3} 

¹Clinic for Neurosurgery, Medical Faculty, Heinrich-Heine University Düsseldorf, 40225, Germany

²German Consortium for Translational Cancer Research (DKTK), Essen/Düsseldorf, 45147, Germany

³Beijing Neurosurgical Institute, Capital Medical University, Beijing, 100050, PR China

*Authors for correspondence: Tel.: +49 211 81 080 13; Ulf.Kahlert@med.uni-duesseldorf.de; mail@ulf-kahlert.com

Aim: Glioblastoma is a heterogeneous lethal disease, regulated by a stem-cell hierarchy and the neurotransmitter microenvironment. The identification of chemotherapies targeting individual cancer stem cells is a clinical need. **Methodology:** A robotic workstation was programmed to perform a drug concentration to cell-growth analysis on an *in vitro* model of glioblastoma stem cells (GSCs). Mode-of-action analysis of the selected top substance was performed with manual repetition assays and acquisition of further parameters. **Results:** We identified 22 therapeutic potential substances. Three suggested a repurpose potential of neurotransmitter signal-modulating agents to target GSCs, out of which the Parkinson's therapeutic trihexyphenidyl was most effective. Manual repetition assays and initial mode of action characterization revealed suppression of cell proliferation, cell cycle and survival. **Conclusion:** Anti-neurotransmitter signaling directed therapy has potential to target GSCs. We established a drug testing facility that is able to define a mid-scale chemo response of *in vitro* cancer models, possibly also suitable for other cell systems.

First draft submitted: 11 March 2020; Accepted for publication: 6 May 2020; Published online: 28 May 2020

Keywords: cancer stem-like cells • drug repurposing • glioblastoma • *in vitro* pharmacogenomics • neurotransmitters • personalized medicine • robot • translational research

Cancer is a global health problem for which the most frequently used treatment is chemotherapy. Given the molecular and cellular heterogeneity of cancer as an entity, the identification of tailored chemotherapies for each individual tumor is considered to improve the response to treatment [1,2]. In this study, we focus on glioblastoma, the most frequent malignant primary brain tumor and one of the most lethal cancers [3]. Tumors, including glioblastoma, are thought to be organized in a hierarchical manner with cells possessing stem cell properties which are the main determinants of disease malignancy and progression. Moreover, the interaction of tumor cells with the microenvironment is believed to determine tumor therapy resistance [4,5]. Consequently, there is growing evidence suggesting a strong relationship between brain cancer and the neurotransmitter microenvironment and intervening in these signals was recently suggested as a promising strategy to fight the disease [4,6].

In vitro pharmacologic testing is an early stage of drug development and is the fundament of various *in vitro*-diagnostic technologies. Liquid handling systems allow large-scale, reproducible and accurate allocation of solved components and represent a standard tool in both industry laboratories and routine diagnostics [7]. By using an embedded robotic automation equipment, we applied an industry-standard technology into an academic preclinical research laboratory and performed a medium-size screening analysis by correlating drug-concentration with cell-growth. We established a screening library composed of market-approved substances with reported blood–brain barrier permeability to potentiate a rapid clinical translation of the results. Using this robotic-based strategy, we

identified 22 anti-cell-growth compounds, out of which three were neurotransmitter signal-modifying substances, with previously unreported therapeutic relevance in the context of glioblastoma.

Methods

A custom-made 10 mM drug library (dissolved in dimethyl sulfoxide; DMSO) consisting of 167 US FDA approved, molecularly diverse compounds with reported brain tissue penetration was assembled and purchased (TargetMol, MA, USA; [Supplementary Tables 1 & 2](#)). We programmed the robot to deliver drugs into 384-well plates using duplicate wells for each drug (V-bottom 384-well plates, Axygen, Corning Inc., NY, USA). The prepared plates were sealed and stored at -80°C . The following drug concentrations: 100,000, 10,000, 1000, 100 and 10 nM per well, previously diluted in Dulbecco's Modified Eagle's Medium to reduce DMSO content (in concordance with the manufacturer of the compound library) were generated by using a robot-mediated dilution assay. For each dilution, a separate 384-plate was used, and the final dispensed volume was 10 μl .

For manually executed validation assays, DL-trihexyphenidyl hydrochloride (THP; Sigma Aldrich, MO, USA) was resuspended to a final concentration of 50 mM in methanol, MeOH, (in concordance with the manufacturer instructions), after which serial dilutions for the above mentioned working concentrations were prepared; then it was stored at $+4^{\circ}\text{C}$.

The glioblastoma neurosphere model GBM1 [8,9] was cultured as previously described [10]. Cells were passaged every other day.

The Beckman Coulter Biomek[®] FxP robotic workstation with attached micro-plate reader (Paradigm, now Molecular Devices, CA, USA) was programmed according to software instructions provided by the manufacturer to perform a high-resolution (5 different molar concentrations per substance plus vehicle control) drug response testing through determination of response on cellular growth. We exclusively used the multichannel arm for pipetting.

To determine the compatibility of the cell-growth readout assay and the plastic labware selection with the robotic workstation experiments, we performed manual assays comparing the readout robustness and sensitivity of MTT assay (3-(4,5-dimethylthiazol-2-yl)-2,5-diphenyl tetrazolium bromide; Sigma Aldrich), XTT assay (sodium 3'-[1-(phenylaminocarbonyl)-3,4-tetrazolium]-bis (4-methoxy6-nitro) benzene sulfonic acid hydrate; Abcam, Cambridge, UK) and CellTiter-Glo[®] (CTG) assay (Promega, Walldorf, Germany) in our robot setup (data not shown). Given the result that the most reliable readouts were of modified CTG (1:1, v:v dilution of CTG solution with PBS [phosphate-buffered saline]) luminescence over XTT and MTT absorbance in this specific set-up ([Supplementary Figure 1B & C](#)), we decided to use CTG as our reporter assay.

First, we determined the optimal cell number to be plated in our setting, ensuring exponential growth rate and maximum signal-to-noise intensity. Therefore, we tested the CTG reporter with 500, 1000, 2000, 3000, 6000, 8000, 10,000 and 15,000 GBM1 cells per well in white 384-well plates (Corning Inc.). On each plate; we included a respective blank control (media, no cells) to normalize the background reading. Single-cell dissociation of the spheres was performed using TrypLE (Thermo Fisher Scientific, MA, USA) and cell counting was performed using Muse[™] Count & Viability Kit (Luminex, TX, USA). Robotic cell plating was assisted using 96-deep-well plates (Eppendorf, Hamburg, Germany) as reservoirs for cell suspension. The luminescence reagent (CTG) was pipetted immediately afterward and readout was performed after 2 min of shaking followed by 10 min of incubation at room temperature. We decided to use 10,000 cells in 40 μl media/well as our cell plating setup for subsequent robotic *in vitro* drug screening.

Second, we thawed the pre-assembled drug plates, carefully took off the seals and combined the dispensed drug solution with the cells (for a total volume of 50 μl ; resulting in working drug concentrations of 20,000, 2000, 200, 20 and 2 nM and vehicle control). Cells were then incubated with the drugs for 72 h in standard culture conditions (humidified 37°C , 5% CO_2). Afterward, the plates were placed in the robot deck where 40 μl of incubated cells were transferred to our white 384-well readout plates and CTG assay was performed as described. The transfer to white plates maximizes light output signal in the reaction wells and decreases noise signals compared with clear plates (data not shown). Given the fully automated nature of this transfer step, we hypothesize that it would not have introduced additional error or risk of error. All assays were performed in biological quadruplicates.

Third, the raw-values were arranged in a logarithmic dose-response curve with which IC_{50} concentrations were calculated. Statistically significant responses result in ranking the tested substances according to their therapeutic potential using curve analysis and IC_{50} values.

Fourth, for the manual THP cell growth/viability assays, GBM1 cells were dissociated with TrypLE, washed once with PBS and adjusted to 2000 cells in 100 μ l complete media per well and pipetted in technical triplicates of a 1:1000 drug dilutions on black 96-well plates (Nunc A/S, Roskilde, Denmark), resulting in concentrations of 10, 20, 30, 40 and 50 μ M of THP and a MeOH control. All assays were performed in biological triplicates.

Finally, apoptosis assays were performed with the Annexin V & Dead Cell Kit (Merck, Darmstadt, Germany), proliferation assay with the Ki67 Proliferation Kit (Luminex), cell cycle assay with the Muse[®] Cell Cycle Kit (Luminex) and used with the Muse[®] Cell Analyzer flow cytometer, according to the protocol from the manufacturer. All assays were performed after 48 h incubation with the calculated half maximal inhibitory concentration (IC₅₀) drug concentration in biological triplicates.

Statistical analysis was performed with Prism Graphpad 8 software. The media control luminescence value average was rested from all the wells. The average luminescence value of the wild-type GBM1 containing wells was used as a control for normalization. The performed statistical tests depended on the number of variables; for two variables unpaired two-sided Student's *t*-test, and for more than two variables, two-sided one-way-ANOVA were used.

Results

We acquired data for all the library compounds (Supplementary Tables 1 & 2) and observed diverse responses and curve characteristics (Supplementary Figure 1A). Afterward, we made a logarithmic dose–response curve analysis and obtained IC₅₀ values. With these variables, we then classified the drugs as compounds with intermediate potency – between 25 and 50% cell growth decrease and substances with high potency – <75% cell growth decrease. Drugs with atypical dose–response curves and IC₅₀ values not corresponding to the cell growth decrease were excluded for further consideration.

From repetitive drug-dose generated response profiles, 22 compounds exhibited a homogeneous decrease of cellular growth in the low micromolar concentration range compared with that of vehicle treatment control ($p \leq 0.001$) (Table 1; Figures 1; Supplementary 2 & 3). Out of which, 13 showed intermediate potency response and 9 exhibited high potency response (Figure 2). Out of these 22 drugs, nine were tested in preclinical studies related with glioblastoma, and ten drugs are investigated in clinical trials with glioblastoma patients. In addition, five of them have a confirmed mode of action related to neurotransmitter activity regulation including acetylcholine (ACh), serotonin (5-HT), dopamine and GABA signaling (Table 1).

From these compounds, we identified three novel repurposes for drugs without any previous reported annotation to neuro-oncology: THP, a ACh receptor antagonist used in symptomatic treatment of Parkinson's disease; homatropine, an ACh drug mainly used in ophthalmology for mydriasis induction, uveitis; as well as rizatriptan, a neurologic medication used primarily as an anti-migraine agent (Tables 1 & 2).

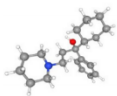
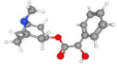
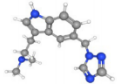
Furthermore, we classified the additional 19 drugs according to their clinical applications. Out of these, five were repurposed drugs that had main clinical application for neuropsychiatric conditions such as migraine, epilepsy, psychosis, schizophrenia and bipolar disorder among others (Supplementary Table 2). The rest of the drugs from this classification were mainly cytotoxic drugs used to treat a variety of cancers, including the DNA-alkylating agent temozolomide, the standard of care chemotherapeutic agent to treat glioblastoma patients.

With having the highest potency scoring in our screening list and given the novelty of this compound in the context of brain cancer, we chose THP for our validation experiments to manually confirm the effects found with the robot (Figure 1C). Sequential drug concentration to cell-growth assays reported logarithmic decrease of viability with increasing drug concentrations ($p \leq 0.001$; Figure 2A, calculated IC₅₀ of ~ 20 μ M). We then went ahead and performed mode of action analysis. After 48 h of incubation of the cells with the IC₅₀ dose of THP, there was a 19% increase in apoptosis compared with control ($p \leq 0.001$); supported by an increase of cells containing shredded DNA as revealed by higher 8% more subG1-fraction in our cell cycle analysis ($p \leq 0.001$). Moreover, THP causes 8% reduction of cell proliferation ($p \leq 0.05$), supported by an increase of 7% in G0/G1 of the treated cells in the cell cycle analysis ($p \leq 0.001$) (Figure 2B–D).

Discussion & conclusion

Our data expand the recent accumulating evidence that brain tumors can be treated by neurotransmitter targeting compounds, in two main points. THP has not been reported to possess therapeutic potential against glioblastoma, thereby expanding the opportunities of pharmacological compounds in this context. We also show data characterizing the mode of action underlying this observation, thereby contributing to fundament the proposed

Group	Compound	Main indication	Mechanism	Research phase in GBM treatment	Table S2 correlation no.
High potency	Palbociclib	Breast cancer	CDK inhibitor (CDK4/6)	Clinical trial	1
	Trihexyphenidyl	Parkinson's disease	Anticholinergic	None	2
	Clonidine	Arterial hypertension	Central alpha-adrenoceptor agonist	Pre-clinical	3
	Nilotinib	Leukemia and Philadelphia positive chronic myeloid	BCR/ABL tyrosine kinase inhibitor	Clinical trial	4
	Homatropine	Mydriasis induction	Anticholinergic	None	5
	Doxorubicin	Multiple types of cancers	Anthracycline, topo isomerase 2 inhibitor	Clinical trial	6
	Brexiprazole	Psychosis	Serotonin-dopamine activity modulator	Pre-clinical	7
	Dasatinib	Leukemia, Philadelphia positive acute and chronic	Tyrosine kinase inhibitor, SRC-family	Clinical trial	8
	Nintedanib	Lung cancer	FGFR and VEGFR protein inhibitor	Clinical trial	9
Intermediate Potency	Vinblastine	Multiple types of cancers	Antimicrotubule	Clinical trial	10
	Imiquimod	Skin cancer	Immune response modifier	Clinical trial (indirect*)	11
	Phenoxybenzamine	Arterial hypertension	Alpha-adrenoceptor blocker	Pre-clinical	12
	Rizatriptan	Migraine	Serotonin agonist	None	13
	Letrozole	Breast cancer	Aromatase inhibitor	Pre-clinical	14
	Divalproex	Psychosis/epilepsy	GABA agonist/histone deacetylase inhibitor	Pre-clinical	15
	Regorafenib	Multiple types of cancers	VEGFR protein inhibitor	Pre-clinical	16
	Everolimus	Multiple types of cancers	mTOR inhibitor	Clinical trial	17
	Paclitaxel	Multiple types of cancers	Antimicrotubule	Pre-clinical	18
	Romidepsin	Leukemia	Histone deacetylase inhibitor	Clinical trial	19
	Topotecan	Multiple types of cancers	Topoisomerase 1 inhibitor	Pre-clinical	20
	Gefitinib	Lung cancer	EGFR inhibitor	Pre-clinical	21
	Temozolomide	Glioblastoma	Alkylate/methylate DNA	Clinical use	22

	Molecular properties			Clinical properties				Ref.
	Molecular 3D structure	Molecular formula	Molecular weight	Mechanism of action	Brands/other names	Indications	Adult dosing	
Trihexyphenidyl		C ₂₀ H ₃₁ NO	301.5 g/mol	Muscarinic receptor-ACh antagonist	Artane, Trihex	Parkinsonism and extrapyramidal symptoms	Up to 15 mg/day, oral administration	[11]
Homatropine		C ₁₆ H ₂₁ NO ₃	275.34 g/mol	Anticholinergic	Isopto Homatropine	Mydriasis, uveitis	Up to 5 daily drops from 2% ocular solution	[11]
Rizatriptan		C ₁₅ H ₁₉ N ₅	269.34 g/mol	5-HT agonist	Maxalt	Migraine headache	Up to 30 mg/day, oral administration	[11]

ACh: Acetylcholine; 5-HT: Serotonin.

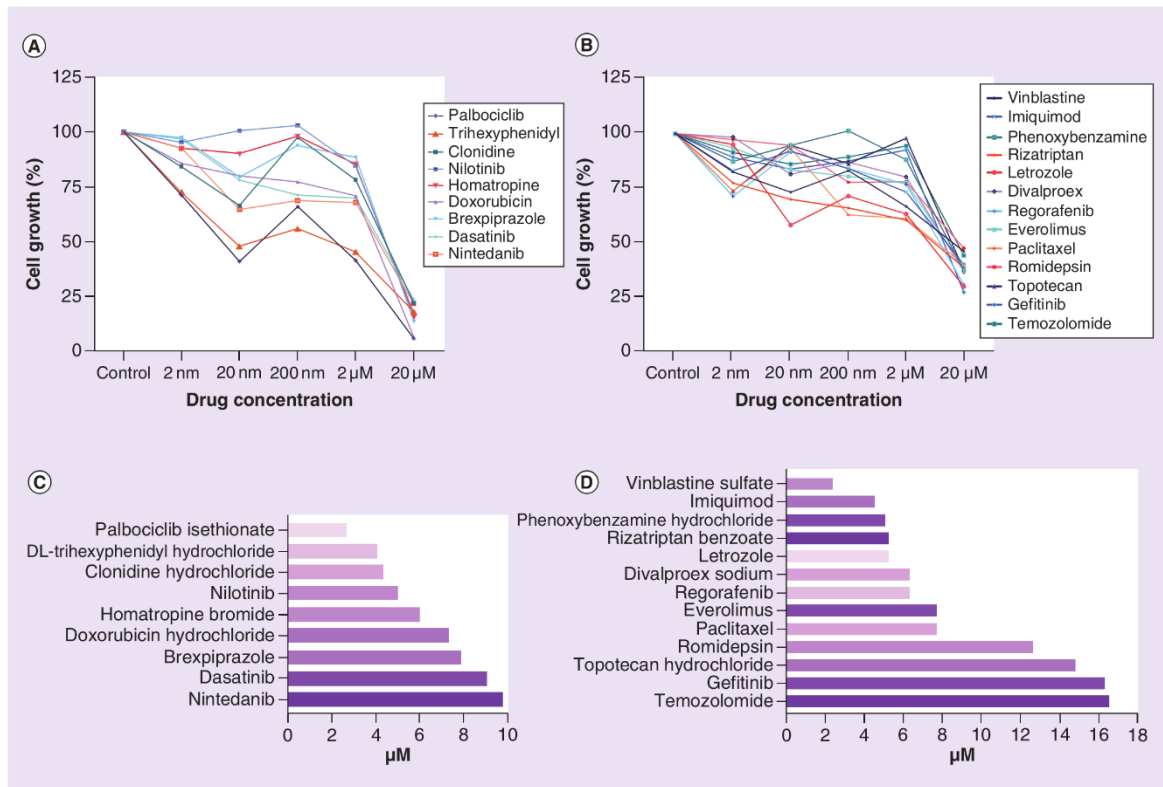


Figure 1. Compound response classification in robotic screening assay. (A) High potency drugs with >75% cell growth decrease. **(B)** Intermediate potency drugs between 25 and 50% cell growth decrease. **(C)** IC₅₀ calculation for high potency drugs with the validated drug trihexyphenidyl highlighted. **(D)** IC₅₀ calculation for intermediate potency drugs. IC₅₀: Half maximal inhibitory concentration.

drug repurposing. Second, we extend the little existing data that the stem cell population in glioblastoma can be effectively treated with neurotransmitter pathway-targeting chemotherapy [5]. THP is a Parkinson's disease approved treatment with a mACh/ACh modulating mode of action. This mechanism has been described as a glioblastoma disease modulator in recent literature [4], as well as other similar mechanisms, such as monoamines which include 5-HT, dopamine and norepinephrine [6,12]. Our results are in line with recently accumulating evidence that neurotransmitter biology promotes glioblastoma development [13].

We are aware that cell models only simplify the complexity of the disease and lack pathophysiological recapitulation of the tumor microenvironment, therefore results must be considered as an abstract guidance. The authors note that a 3D model system, more commonly referred to as HSR-GBM1 and derived from a single tumor of a patient operated in Milan, Italy, was used in this study. Those spheroidic systems are suggested to most closely recapitulate tumor conditions *in vitro* [14]. We acknowledge that our data cannot exclude that THP toxicity is caused by off-target effects and does not affect neurotransmitter signaling or members of the neurotransmitter signaling pathways in glioblastoma. Further characterization of the response of glioblastoma cells to the drug, such as through pharmacometabolomics [15] shall be conducted to validate target specificity and is required before this novel approach would be applied in the management of this fatal disease. Even if target specificity cannot be confirmed, clinical testing could possibly be proceeded since many clinical cancer drugs act in an unknown off-target way [16].

From a clinical-translational prospective, we think that this technology would be useful to determine personal chemo-responsiveness of primary cells freshly derived from surgical resection specimens. Our robotics complete the

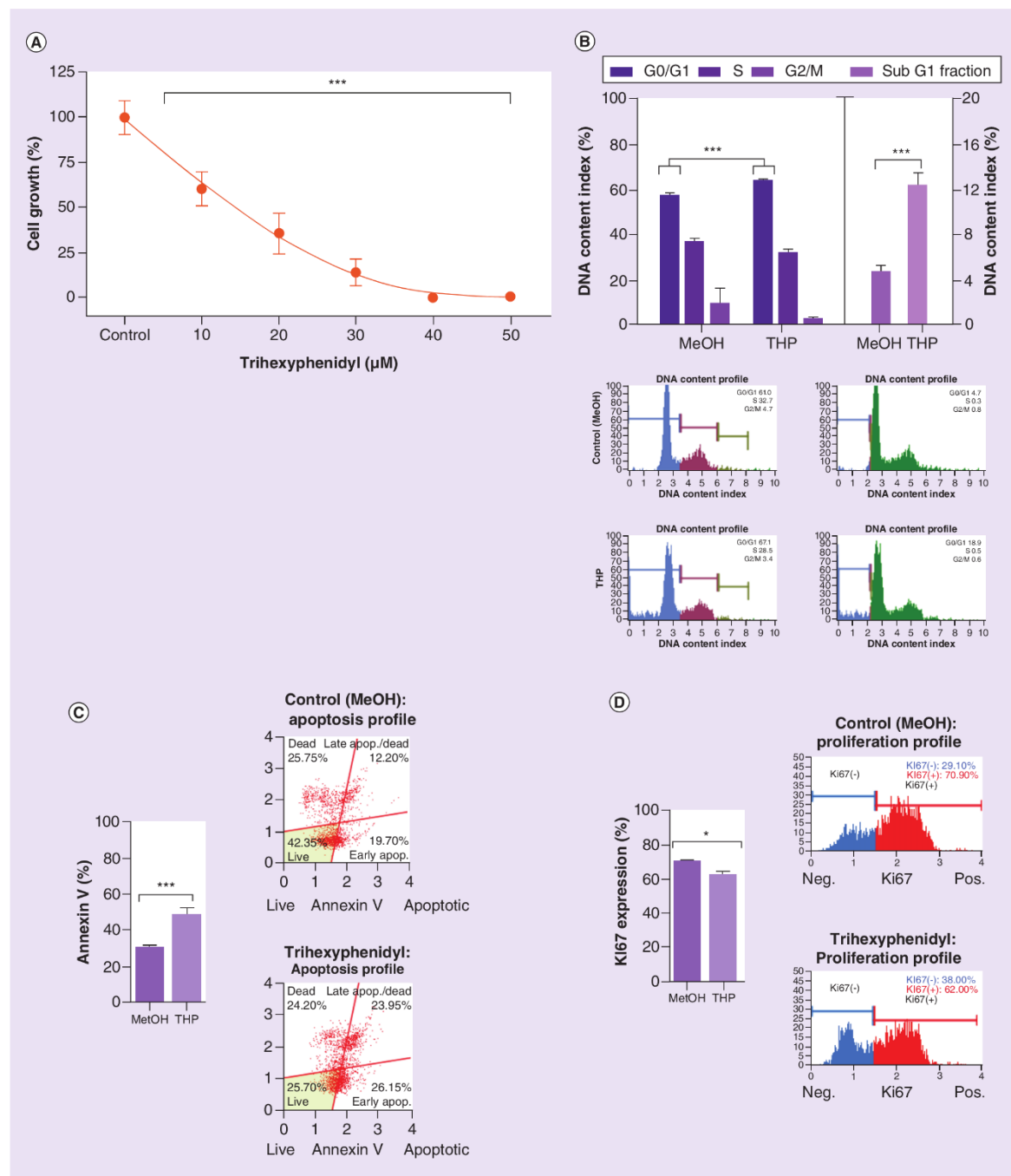


Figure 2. Targeted manual validation of robot screening results (trihexphenidyl). (A) Cytotoxic effect of Trihexphenidyl on GBM1 measured with normalized-to-control CellTiter-Glo® luminescence. (B) Increase of 8% of the apoptosis indicator subG1-fraction against MeOH control ($p \leq 0.001$), significant increase of 7% in G0/G1 of the treated cells in the cell cycle against MeOH control ($p \leq 0.001$) and flow cytometry gating. (C) Apoptosis increase and flow cytometry gating against MeOH control ($p \leq 0.001$). (D) Proliferation decrease ($p \leq 0.05$) supported by increase in G0/G1 in cell cycle results. All after 48 h drug exposure in GBM1 cell line. Unpaired two-sided student T test.

* $p < 0.05$; ** $p < 0.01$; *** $p < 0.001$.
MeOH: Methanol.

list of liquid handling devices to do drug testing on tumors *in vitro* [2,17], thereby allowing this approach to be implementable in different lab settings and suitable for a variety of disease types and disease modeling strategies. We argue that our system will also be useful for testing drug resistance on more complex cell model culture systems that require pre-coating of culture plates – such as human induced pluripotent stem cells – mainly due to the detailed and programmable pipetting basis of liquid transfer in our device, which emulate manual pipetting on a high scale and cannot be facilitated by printing-based drug screening assays [18]. We considered the identification of known anti-glioblastoma drugs among the 22 identified effective treatments, as an additional validation indicator for our screening method.

Informing patients with advanced stages of the disease about individually tailored and clinical feasible treatment options, as an alternative or addition to standard of care treatment, represents an innovation mark for modern treatment centers. Given the overall challenges in glioblastoma therapy with standard of care, this tool at least opens the opportunity of discussion to improve treatment based on functional and technological fundamentals. Furthermore, since the costs to execute such a screening are considerably low (approximately 350 EUR including all consumables, media and drugs; excluding personnel costs), we think that it could be ethical and economically feasible to include this in standard diagnostics for selected patients such as those with recurring glioblastoma and cerebral metastasis. We propose the utilization of this technology in drug discovery and personalized medicine.

Moreover, we note that our technology development project is well in line with recently stated consensus findings for research integrity [19]; and given the opportunity that we count with simple embedment of the robot-acquired electronic data in modern data -storage, -reporting and -archiving strategies, we hypothesize that the inclusion of lab-ware automation in academic laboratory routine is a useful strategy to improve reproducibility and transparency in preclinical research [20].

Summary points

- We extend the recent accumulating evidence that using a neurotransmitter targeting strategy is an innovative treatment route for glioblastoma and extend it with two principle novelties:
 - We identified a previously unrecognized, clinical approved neurotransmitter-targeting drug to possess therapeutic effect on glioblastoma.
 - We found that following the scope of using anti-neurotransmitter directed treatment kills stem cells in glioblastoma.
- We developed a robotic strategy to score therapy resistance *in vitro* in mid- to large-scale ranges.
- The pipetting fundamentals of liquid aspiration and dispersion will allow the application in more complex culture systems that require coating of the cell culture plate.
- In this context, the technology is superior than printing-based liquid handling solutions.
- Our technology is well in line with recent stated guidelines on research integrity, addressing transparency and reporting of experimental studies.
- We propose the utilization of this technology in drug discovery and personalized medicine.

Supplementary data

To view the supplementary data that accompany this paper please visit the journal website at: www.futuremedicine.com/doi/suppl/10.2217/cns-2020-0004

Author contributions

Conceptualization: UD Kahlert, S Muhammad; MA Kamp, W Zhang; methodology: UD Kahlert, I Fischer, A Vargas-Toscano and M Hewera; software: UD Kahlert and A Vargas-Toscano; validation: A Vargas-Toscano and A-N Nickel; formal analysis: A Vargas-Toscano, M Hewera, A-C Nickel; investigation: A Vargas-Toscano; resources, UD Kahlert, H-J Steiger, D Hänggi; data curation: A Vargas-Toscano; writing-original draft preparation: A Vargas-Toscano, UD Kahlert, W Zhang and D Khan; writing-review and editing: all authors; visualization: A Vargas-Toscano; supervision, UD Kahlert; project administration: UD Kahlert; funding acquisition: UD Kahlert, H-J Steiger, D Hänggi. All authors have read and agreed to the published version of the manuscript.

Acknowledgments

The authors acknowledge S Weggen, Institute for Neuropathology at Heinrich-Heine University, Düsseldorf for kindly providing the robotic related devices used for the experiments.

Financial & competing interests disclosure

A Vargas-Toscano is supported by the Catholic Academic Exchange Service of the German Catholic Church (KAAD). The work of UD Kahlert is supported by the Federal Ministry of Education and Research (BMBF KZ 03VP03791), the VolkswagenStiftung, the Hempel Family Foundation, the Brigitte-and Dr. Konstanze Wegener Foundation and the Sino-German Center for Science Promotion. The authors have no other relevant affiliations or financial involvement with any organization or entity with a financial interest in or financial conflict with the subject matter or materials discussed in the manuscript apart from those disclosed.

No writing assistance was utilized in the production of this manuscript.

Ethical conduct of research

The authors state that they have obtained appropriate institutional review board approval or have followed the principles outlined in the Declaration of Helsinki.

Open access

This work is licensed under the Attribution-NonCommercial-NoDerivatives 4.0 Unported License. To view a copy of this license, visit <http://creativecommons.org/licenses/by-nc-nd/4.0/>

References

Papers of special note have been highlighted as: ● of interest; ●● of considerable interest

1. Gorshkov K, Chen CZ, Marshall RE *et al.* Advancing precision medicine with personalized drug screening. *Drug Discov. Today* 24(1), 272–278 (2019).
- **Reports relevance of tailored chemotherapy.**
2. Skaga E, Kuleskiy E, Fayzullin A *et al.* Intertumoral heterogeneity in patient-specific drug sensitivities in treatment-naïve glioblastoma. *BMC Cancer* 19, 628 (2019).
3. Stupp R, Mason WP, van den Bent MJ *et al.* Radiotherapy plus concomitant and adjuvant temozolomide for glioblastoma. *N. Engl. J. Med.* 352(10), 987–996 (2005).
4. Thompson EG, Sontheimer H. Acetylcholine receptor activation as a modulator of glioblastoma invasion. *Cells* 8(10), E1203 (2019).
- **Reports relation between glioblastoma and the brain neurotransmitter microenvironment.**
5. Caragher SP, Shireman JM, Huang M *et al.* Activation of dopamine receptor 2 prompts transcriptomic and metabolic plasticity in glioblastoma. *J. Neurosci.* 39(11), 1982–1993 (2019).
6. Jiang SH, Hu LP, Wang X, Li J, Zhang ZG. Neurotransmitters: emerging targets in cancer. *Oncogene* 39(3), 503–515 (2020).
7. Bogue R. Robots in the laboratory: a review of applications. *Ind. Robot* 39(2), 113–119 (2012).
- **Emphasizes relevance of robotic technologies in laboratories and routine diagnostics.**
8. Fan X, Khaki L, Zhu TS *et al.* NOTCH pathway blockade depletes CD133-positive glioblastoma cells and inhibits growth of tumor neurospheres and xenografts. *Stem Cells* 28(1), 5–16 (2010).
9. Kahlert UD, Suwala AK, Raabe EH *et al.* ZEB1 promotes invasion in human fetal neural stem cells and hypoxic glioma neurospheres. *Brain Pathol.* 25(6), 724–732 (2015).
10. Kahlert UD, Maciaczyk D, Dai F *et al.* Resistance to hypoxia-induced, BNIP3-mediated cell death contributes to an increase in a CD133-positive cell population in human glioblastomas *in vitro*. *J. Neuropathol. Exp. Neurol.* 71(12), 1086–1099 (2012).
11. National Center for Biotechnology Information. PubChem Database. <https://pubchem.ncbi.nlm.nih.gov/>
12. Beaulieu JM, Gainetdinov RR. The physiology, signaling, and pharmacology of dopamine receptors. *Pharmacol. Rev.* 63(1), 182–217 (2011).
13. Venkataramani V, Tanev DI, Strahle C *et al.* Glutamatergic synaptic input to glioma cells drives brain tumour progression. *Nature* 573(7775), 532–538 (2019).
- **Reports brain tumor progression under neurotransmitter microenvironment.**
14. Brancato V, Oliveira JM, Correlo VM, Reis RL, Kundu SC. Could 3D models of cancer enhance drug screening? *Biomaterials* 232, 119744 (2020).
15. Koch K, Hartmann R, Tsiampali J *et al.* A comparative pharmaco-metabolomic study of glutaminase inhibitors in glioma stem-like cells confirms biological effectiveness but reveals differences in target-specificity. *Cell Death Discov* 6, 20 (2020).
16. Lin A, Giuliano CJ, Palladino A *et al.* Off-target toxicity is a common mechanism of action of cancer drugs undergoing clinical trials. *Sci. Transl. Med.* 11(509), eaaw8412 (2019).
17. Skaga E, Kuleskiy E, Brynjulvsen M *et al.* Feasibility study of using high-throughput drug sensitivity testing to target recurrent glioblastoma stem cells for individualized treatment. *Clin. Transl. Med.* 8(1), 33 (2019).

18. Tseng H, Gage JA, Shen T *et al.* A spheroid toxicity assay using magnetic 3D bioprinting and real-time mobile device-based imaging. *Sci. Rep.* 5, 13987 (2015).
19. Lancet T. Assessing researchers with a focus on research integrity. *Lancet* 393(10181), P1570 (2019).
20. Yeow J, Ng PK, Tan KS, Chin TS, Lim WY. Effects of stress, repetition, fatigue and work environment on human error in manufacturing industries. *J. Appl. Sci.* 14(24), 3464–3471 (2014).

Table S1. All compounds used.

well Compound Name	No.	well Compound Name	No.	well Compound Name	No.	well Compound Name	No.
A1 Almotriptan Malate	1	D17 Erzalutamide	42	H11 Mercaptopurine	83	L13 Riluzole	124
A3 Dasatinib	2	D19 Irinotecan	43	H13 Phenytoin sodium	84	L15 Timolol Maleate	125
A5 Aminoglutethimide	3	D21 Imatinib	44	H15 Primidone	85	L17 Lenvatinib	126
A7 DL-threoxyphenidyl hydrochloride	4	E1 Risperidone	45	H17 Procaine	86	L19 Scopolamine HBr trihydrate	127
A9 Everolimus	5	E3 Bosutinib	46	H19 Imiquimod	87	M1 5-Azacytidine	128
A11 Nintedanib	6	E5 Sunitinib Malate	47	I1 Cabozantinib Malate	88	M3 Afatinib Dimaleate	129
A13 Temozolomide	7	E7 Olanzapine	48	I3 Fluoxetine hydrochloride	89	M5 Idelalisib	130
A15 Topotecan hydrochloride	8	E9 Fulvestrant	49	I5 Gemcitabine	90	M7 Melindone hydrochloride	131
A17 Clonidine hydrochloride	9	E11 Oxaprozin	50	I7 Rocuronium bromide	91	M9 Eliglustat	132
A19 Gefitinib	10	E13 Amitriptyline hydrochloride	51	I9 Nintedanib Ethanesulfonate Salt	92	M11 Cobimetinib	133
A21 Benzocaine mesylate	11	E15 Risperidone	52	I11 Aprepitant mesylate	93	M13 Acalabrutinib	134
B1 Netupitant	12	E17 Ethambutol dihydrochloride	53	I13 Cabozantinib hydrochloride (849217-68-1(free base))	94	M15 Homoharringtonine	135
B3 Romidepsin	13	E19 Chlorpromazine hydrochloride	54	I15 Cariprazine	95	M17 Ivosidenib	136
B5 Quetiapine Fumarate	14	E21 Fluconazole	55	I17 Rucaparib	96	M19 Ribociclib	137
B7 Rizatriptan benzoate	15	F1 Trifluridine	56	I19 Larotrectinib sulfate	97	N1 Brexpiprazole	138
B9 Lenalidomide	16	F3 (E)-Endoxifen	57	J1 Nilotinib	98	N3 Neostigmine bromide	139
B11 Vinorelbine sulfate	17	F5 Encorafenib	58	J3 Lorlatinib	99	N5 Cisplatin	140
B13 Alpelisib	18	F7 Brutinib	59	J5 Phenazopyridine hydrochloride	100	N7 Primozide	141
B15 Abemaciclib	19	F9 Terfenadine	60	J7 Copanlisib	101	N9 Itraconazole	142
B17 Trametinib	20	F11 LDK378	61	J9 Mitoxantrone hydrochloride	102	N11 Cyclophosphamide monohydrate	143
B19 Binimetinib	21	F13 Decarbazine	62	J11 Maprotiline hydrochloride	103	N13 Docetaxel	144
B21 Decitabine	22	F15 Facitaxel	63	J13 Homatropine Bromide	104	N15 Ifosfamide	145
C1 Calcium folinate	23	F17 Fiumazenil	64	J15 Levetiracetam	105	N17 Zolmitriptan	146
C3 Acetaminophen calcium	24	F19 Sorafenib tosylate	65	J17 Protriptyline hydrochloride	106	N19 Mifepristone	147
C5 Bortezomib	25	F21 Fludarabine	66	J19 Sumatriptan succinate	107	O1 Doxorubicin hydrochloride	148
C7 Rasagiline	26	G1 Oxycodone	67	K1 Carfilzomib	108	O3 Nortriptyline hydrochloride	149
C9 Meprobamate	27	G3 Proparacaine hydrochloride	68	K3 Lurasidone hydrochloride	109	O5 Belinostat	150
C11 Phenoxybenzamine hydrochloride	28	G5 Oxaliplatin	69	K5 Floxuridine	110	O7 Vemurafenib	151
C13 Cytarabine	29	G7 Erlotinib	70	K7 Hydrocortisone butyrate	111	O9 Atomoxetine hydrochloride	152
C15 Podophyllotoxin	30	G9 Lomustine	71	K9 Niraparib	112	O11 Tamoxifen Z-isomer citrate	153
C17 Lamivudine	31	G11 Tizanidine hydrochloride	72	K11 Erlotinib	113	O13 Acetazolamide	154
C19 Meclizine dihydrochloride	32	G13 Ponatinib	73	K13 Mitomycin C	114	O15 Melflamine hydrochloride	155
C21 Desipramine hydrochloride	33	G15 Paribinostat	74	K15 Pramipexole	115	O17 Ethosuximide	156
D1 Divalproex Sodium	34	G17 Olaparib	75	K17 Axitinib	116	O19 Rifampicin	157
D3 Gilteritinib	35	G19 Cabazitaxel	76	K19 Memantine hydrochloride	117	P1 Palbociclib Isethionate	158
D5 Vandetanib	36	G21 Dacomitinib	77	L1 Alecetinib	118	P3 ABT199	159
D7 Pemetrexed Disodium Hydrate	37	H1 Eslicarbazepine Acetate	78	L3 Iloperidone	119	P5 Delamanid Mesylate	160
D9 Pazopanib	38	H3 Amantadine hydrochloride	79	L5 Duvallinib	120	P7 Crizotinib	161
D11 Osimertinib	39	H5 Plerixafor BHC (AMD3100 BHC)	80	L7 Carbamazepine	121	P9 Artecaine HCl	162
D13 Plerixafor	40	H7 kabapone	81	L9 Dimethylhydrazine	122	P11 Dabrafenib	163
D15 Neratinib	41	H9 Celecoxib	82	L11 Nimodipine	123	P13 NVP-LDE225	164
						P15 Vorinostat	165
						P17 Exemestane	166
						P19 Letrozole	167

Table S2. Compound classification

Characteristics	Number of Compounds	Drug Correlation numbers Table 1
Characteristics		
Preclinical phase	9	3, 7, 12, 14, 15, 16, 18, 20, 21
Clinical trials/use	10	1, 4, 6, 8, 9, 10, 11, 17, 19, 22
New identified drugs	3	2, 5, 13
Neurotransmitter modulation	5	2, 5, 7, 13, 15
Clinical Indication		
Oncological	14	1, 4, 6, 8, 9, 10, 14, 16, 17, 18, 19, 20, 21, 22
Multi-cancer indication	6	6, 10, 16, 17, 18, 20
Breast cancer	2	1, 14
Lung cancer	2	9, 21
Leukemia	3	4, 8, 19
Skin cancer*	1*	11*
Glioblastoma	1	22
Non-oncological	8	2, 3, 5, 7, 11, 12, 13, 15
Neurologic / Psychiatric	4	2, 7, 13, 15
Parkinson's disease	1	2
Migrane	2	13, 15*
Antipsychotic	1	7
Mood stabilizer	1	15*
Epilepsy	1	15*
Antihypertensive	2	3, 12
Ophthalmologic	1	5
Dermatologic	1	11
Total	22	1-22

*Marked compounds were classified in different indications, but were only counted once.

Figure S1

a. All compounds before classification
b. and. c. Reagent comparison.

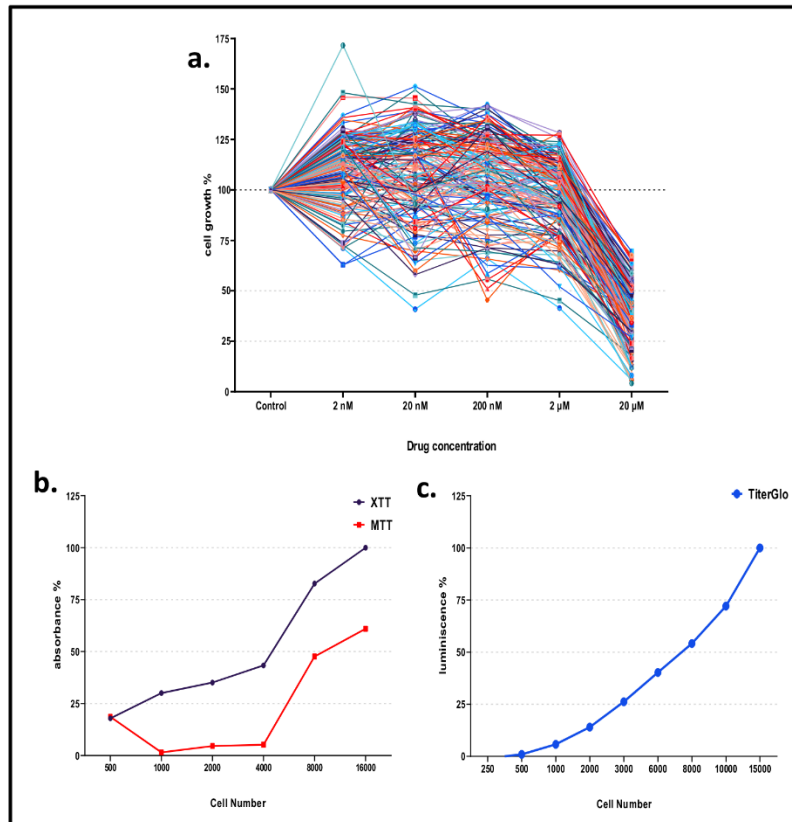


Figure S2

High Potency Compared to Control

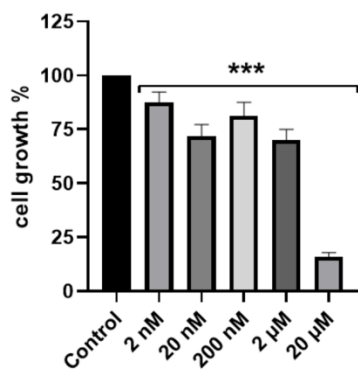
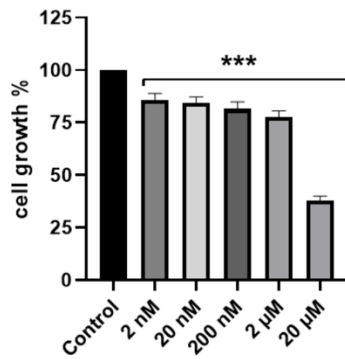


Figure S3

Intermediate Potency Compared to Control



4. Paper 3 - Influence of Synthesis Methods on the Internalization of Fluorescent Gold Nanoparticles into Glioblastoma Stem-like Cells. Beatriz Giesen, Ann-Christin Nickel, Alba Garzón Manjón, *Andres Vargas Toscano*, Christina Scheu, Ulf Dietrich Kahlert* and Christoph Janiak*. *equal contribution, *Journal of Inorganic Biochemistry*, 203: 110952; Feb (2020)

The published manuscript with supporting information embedded in this chapter was reprinted with the following considerations:

- Published in the year 2020 by the *Journal of Inorganic Biochemistry* from the publisher *Elsevier*.
- The publisher states that “Authors can include their articles in full or in part in a thesis or dissertation for non-commercial purposes”:
<https://www.elsevier.com/about/policies/copyright/permissions>
- The original publication is available under the journal webpage link:
<https://www.sciencedirect.com/science/article/pii/S0162013419306324>
- It can be accessed via PubMed under the following webpage link:
<https://pubmed.ncbi.nlm.nih.gov/31794896/>



Influence of synthesis methods on the internalization of fluorescent gold nanoparticles into glioblastoma stem-like cells

Beatriz Giesen^a, Ann-Christin Nickel^b, Alba Garzón Manjón^c, Andrés Vargas Toscano^b, Christina Scheu^c, Ulf Dietrich Kahlert^{b,d,*}, Christoph Janiak^{a,*}

^a Institut für Anorganische Chemie und Strukturchemie, Heinrich-Heine-Universität Düsseldorf, 40204 Düsseldorf, Germany

^b Klinik für Neurochirurgie, Universitätsklinikum Düsseldorf, 40225 Düsseldorf, Germany

^c Max-Planck-Institut für Eisenforschung GmbH, Max-Planck-Straße 1, 40237 Düsseldorf, Germany

^d Deutsches Konsortium für Translationale Krebsforschung (DKTK), Essen/Düsseldorf, Germany

ARTICLE INFO

Keywords:

Fluorescent gold nanoparticles
Precision medicine
Rapid synthesis
Glioblastoma stem cells
Internalization

ABSTRACT

Glioblastoma (GBM) is an aggressive disease with currently no satisfying treatment option available. GBM cells with stem cell properties are thought to be responsible for the initiation and propagation of the disease, as well as main contributors to the emergence of therapy resistance. In this work, we developed a novel method to synthesize fluorescent gold nanoparticles as potential drug and gene delivery systems for GBM therapy, able to penetrate three-dimensional stem cell selected patient-derived GBM neurosphere systems *in vitro*. By using polyethylene imine (PEI) as a stabilizer and reducing agent, as well as fluorescein isothiocyanate (FITC) as a fluorescent marker, our fully *in-house* developed fluorescent gold nanoparticles (AuPEI-FITC NPs) with core sizes between 3 and 6 nm were obtained via a fast microwave-assisted reaction. Cytotoxicity, adsorption and internalization of AuPEI-FITC NPs into the cell lines JHH520, 407 and GBM1 were investigated using the cellular growth assay and fluorescence-activated cell sorting (FACS) analysis. AuPEI-FITC NPs showed no apparent cytotoxicity and an uptake in cells of up to ~80%. A differentiation between surface-bound and internalized AuPEI-FITC NPs was possible by quenching extracellular signals. This resulted in a maximal internalization degree of 61%, which depends highly on the synthesis method of the nanoparticles and the cell type tested. The best internalization was found for AuPEI-FITC1 which was prepared in a one pot reaction from KAuCl₄, PEI and FITC. Thus, appropriately synthesized AuPEI-FITC NPs show great potential as vehicles to transport DNA or drugs in GBM cells.

1. Introduction

Glioblastoma (GBM), the most common type of brain-born neoplasm, is a lethal and ultra-aggressive type of cancer with a remaining life expectancy of under two years [1]. Current therapy consists of surgical resection, administration of temozolomide and radiotherapy but fails to give a positive outcome due to the invasive and heterogeneous nature of the tumor [2]. A population of cells with stem cell properties (= brain cancer stem-like cells, BCSCs) are thought to be the reason for GBM's high cellular invasion capacity and formation of tumor foci [3]. Delivery of therapeutics to the anticipated BCSCs target site is significantly hindered by the blood-brain barrier (BBB), a major obstacle in GBM treatment [4]. Thus, novel anti-BCSC treatments with clinical applicability are of highest clinical and economical interest.

Recent studies have placed nanomaterials in the focus as the future

technology for the delivery of drugs, molecules or genes to treat GBM, specifically by targeting BCSCs [5,6]. Gold nanoparticles (Au-NPs) in particular have been widely used for medicinal purposes due to their biocompatibility and unique optical properties. Due to the high permeability and enhanced permeation and retention (EPR) in solid tumors, Au-NPs can pass the BBB, accumulate in the damaged tissue and deliver inhibiting or target specific cell surface molecules like proteins or antibodies, which limit tumor cell proliferation and boost the anticancer effect of standard drugs [6–9]. In combination with radiotherapy, Au-NPs increase the DNA damage to GBM cells inflicted by ionization radiation [10]. This radiosensitization enhances the effectiveness of irradiation therapy and also improves the uptake of medications in GBM cells [11,12]. Besides their therapeutic benefits, Au-NPs are also widely used for imaging and sensing applications, showing a longer blood circulation time than common contrast agents [13]. They

* Corresponding author's.

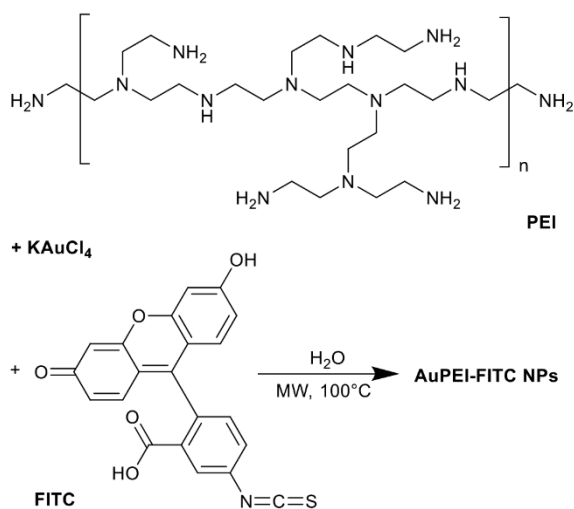
E-mail addresses: Ulf.Kahlert@med.uni-duesseldorf.de (U.D. Kahlert), janiak@uni-duesseldorf.de (C. Janiak).

<https://doi.org/10.1016/j.jinorgbio.2019.110952>

Received 17 September 2019; Received in revised form 14 November 2019; Accepted 22 November 2019

Available online 23 November 2019

0162-0134/ © 2019 Elsevier Inc. All rights reserved.



Scheme 1. Representation of the synthesis protocol for optimized AuPEI-FITC NPs for the internalization into glioblastoma GBM cells.

have allowed the accurate display of tumors for its surgical removal due to their surface enhanced resonance Raman scattering (SERRS) signals in combination with magnetic resonance imaging (MRI), as well as being introduced as precise probes for computer tomography (CT) and photoacoustic visualization of tumors [14–16]. In summary, Au-NPs are promising theranostic systems combining therapeutic anticancer effects with diagnostic features for tracking the biodistribution of GBM tumors *in vivo*.

The aqueous synthesis of Au-NPs is straight-forward, cost effective and non-toxic. Moreover, the highly stable colloids formed are modifiable in size and shape through variation of their synthesis parameters. Their surface can be functionalized with various capping ligands and shells to facilitate the loading of therapeutic agents according to specific cell or drug needs [17]. In gene therapy, polyethylene imine (PEI) (Scheme 1) constitutes a suitable capping ligand for Au-NPs because of its high cationic charge density and ability to condensate nucleic acids to the nanoparticle (NP) surface [18]. In the chemical reaction with gold, PEI acts as a three-in-one reagent: it can reduce gold(III) salts to metallic gold, it protects the formed Au-NPs from agglomeration and it can bind DNA through electrostatic interactions [19].

In nanodelivery applications, fluorescein isothiocyanate (FITC) (Scheme 1), a near-infrared organic dye, can serve as a powerful tracking device to locate NPs inside the cells after incubation due to its high extinction coefficient and great quantum yield. Due to the strong affinity of gold for sulfur, FITC can be effectively coupled to Au-NPs through electronically stable covalent bonds with its isothiocyanate group [20]. This Au-FITC combination holds a stronger fluorescent imaging effect of tumor regions compared to FITC alone, which would rapidly be metabolized and removed by cells [10]. When obtained from commercial sources, little information is given about the capping ligand of fluorescent Au-NPs, the amount of fluorophore used and, in some cases, the overall hydrodynamic size of the gold-ligand-FITC system, which is crucial for cell uptake. If the nanodelivery technology is going to become standard, there needs to be easy, reliable and fast methods to produce fluorescent nanocarriers without the need to resort to expensive outsourcing or intricate synthesis routes.

In this work, we describe a Au-NP assembly functionalized with PEI and FITC (AuPEI-FITC) able to penetrate GBM cells. AuPEI-FITC NPs were synthesized in a straight-forward manner from cheap and accessible starting materials (Scheme 1). We describe the importance of the synthesis parameters on the final size, morphology and ligand

composition of the nanomaterials even when using the same components. Our GBM functional assessments are performed with three-dimensional neurospheres, selected for high percentage of stemness due to neural stem cell growth conditions [21]. The *in vitro* AuPEI-FITC NPs transfection and level of internalization in three BCSC lines are hereby tested for a potential application as a gene or drug carrier in the treatment of GBM.

2. Results and discussion

2.1. Synthesis of gold nanoparticles

Regardless of the various works stating to have found the ideal nanoparticle size and shape for a successful internalization into cells [22–24], the actual impact of these parameters still remains highly dependent on the cell type. In this study, we opted for the synthesis of small gold nanospheres up to 10 nm diameter. By starting with a small core size, multiple functionalization steps on the nanoparticle surface are possible through a layer-by-layer construct, which allows flexibility to customize and increase the size of the carrier if needed. Furthermore, round-shaped Au-NPs were selected due to their curvature, which makes them more likely to be internalized into cells compared to asymmetrical shaped NPs [25].

The synthesis of gold nanoparticles smaller than 20 nm has been documented by adding a tetrachloroaurate precursor into an aqueous PEI solution under diverse reaction conditions [19,26,27]. Size control is not always easy since a stoichiometric variation of reaction precursors also changes the size distribution and polydispersity of the solution. In order to find the necessary gold to PEI ratio for an optimal stabilization of our delivery system, the amount of KAuCl₄ precursor added to a solution of branched PEI was continuously increased as both components were reacted under microwave irradiation (see Supp. info. for synthesis details). Variation of the n_{KAuCl_4}/n_{PEI} molar ratio between 1 and 10 (samples AuPEI1–10 accordingly) resulted in different sizes and polydispersity values, as seen from dynamic light scattering (DLS) results (Fig. 1). In our experiments, hydrodynamic diameters corresponding to the gold core and the PEI capping ligand remained between 24 and 67 nm. In some cases, various species of different sizes were detected even after post-synthesis purification. This phenomenon can be attributed to the formation of higher bridged PEI networks containing several Au cores [7].

However, there seems to be an optimal ratio of PEI to Au, resulting in small AuPEI NPs with low polydispersity, as in the case of AuPEI5 and

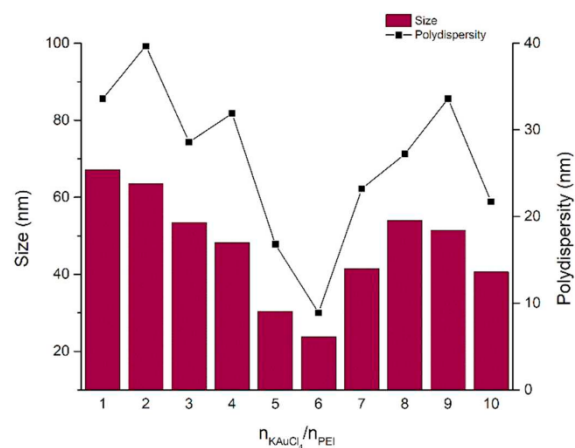


Fig. 1. Size and polydispersity of PEI-capped gold nanoparticles (Au-PEI NPs) with $n_{KAuCl_4}/n_{PEI} = 1-10$.

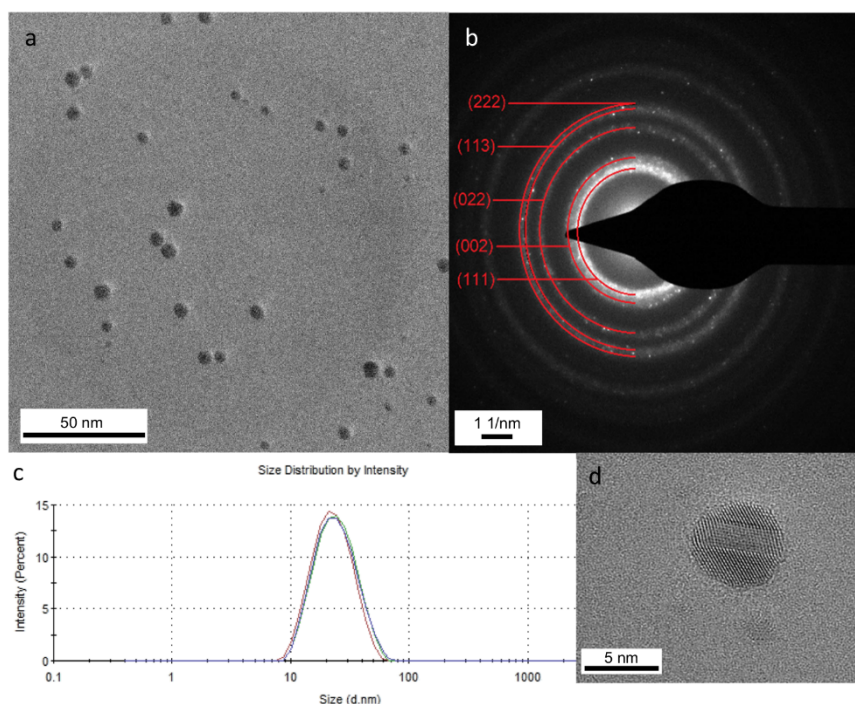


Fig. 2. Characterization of AuPEI6 NPs. a, TEM image of several NPs, b: selected area diffraction showing hkl values for *fcc* gold, c: DLS curve showing the size distribution by intensity of three measurements, d: HR-TEM image of an individual NP.

AuPEI6 with $n_{\text{KAuCl}_4}/n_{\text{PEI}} = 5$ or 6, respectively. With a hydrodynamic diameter of 24 nm and a narrow size distribution, AuPEI6 presented the most homogeneous sample. The small size of AuPEI6 NPs was further confirmed via high-resolution transmission electron microscopy (HR-TEM) measurements, which revealed a gold core of about 4 ± 1 nm (Fig. 2). The sample also displayed high crystallinity and the expected face-centered cubic (*fcc*) phase.

In the reaction of KAuCl_4 and PEI, Au-NPs are formed due to a redox reaction between the amine groups of PEI and the tetrachloridoaurate (III) anion AuCl_4^- . While the Au^{III} salt is reduced to Au^0 , oxidation at the alpha carbon to the amine groups of the PEI polymer chain results in the conversion of the amine into an amide [27]. This assumption was confirmed by infrared (IR) spectroscopy (Fig. S1 in SI).

Given that PEI itself has also been used as a vehicle for DNA transfection [28], it is crucial to eliminate the free unbound PEI from the gold solution in order to test the true ability of AuPEI NPs as a DNA or drug carrier. For this purpose, a thorough dialysis process was performed against water for 24 h (see Supp. info. for details, Fig. S2). When dialyzing the sample AuPEI6 for a longer time, a significant color change from dark red to purple was observed, signaling a size increase of AuPEI NPs due to a possible agglomeration. DLS results showed an increase in hydrodynamic diameter from 24 nm after 24 h to 68 nm after 48 h and ultimately 77 nm after 72 h. On the other hand, when the sample was left to dialyze for only 6 or 12 h, agglomerates of “free” PEI as large as 91 nm were still found in the sample. Thus, determination of the correct dialysis time is relevant to remove both polymer accumulations in the solution or unstable NP agglomerates which lack stabilization.

TEM images and ultraviolet–visible (UV–VIS) spectra of AuPEI6 before and after 24 h of dialysis (Fig. 3) show the importance of purification for obtaining a more homogeneous Au-NP solution. After dialysis, it was possible to remove larger agglomerates from the initial

sample (Fig. 3a, b) and a narrowing of the plasmonic band at 525 nm was observed (Fig. 3c). The resulting AuPEI NPs had a size of 4 ± 1 nm. NPs of this size have successfully loaded drug molecules onto their surface and would be able to exit the body by renal excretion after drug release [29].

Subsequently, the FITC fluorophore was introduced into the AuPEI system as a NP tracking tool in the cells. Several synthesis and purification approaches were tested in order to find a suitable NP species by varying the FITC concentration, the reaction media and ligand incorporation method (Table S1). As a preliminary verification, the cell viability of human embryonic kidney cells (HEK) was monitored after 1 and 3 h of incubation with AuPEI-FITC1–10 NPs at a gold concentration between 0 and 50 mg/L (Fig. S4). Using low toxicity and a good concentration dependence as relevant criteria, samples AuPEI-FITC 1–4 were chosen for further testing in GBM cells. In these four different synthesis approaches, the reaction starting components (gold precursor, PEI and FITC) were introduced at the same ratios but in different order (Fig. 4). Reduction of the gold precursor was always achieved in a hydrothermal microwave reaction, using only PEI as the reducing agent. UV–VIS results of the four samples revealed the characteristic plasmonic peak of Au-NPs at 500 nm (Fig. S5). Solution colors ranged from light orange-red to brownish-red (Fig. S6). Size and size distribution results determined by DLS and TEM for all four synthesis routes are shown in Table S2 and Fig. S7. The morphology of the samples AuPEI-FITC1–4 is displayed in Fig. 5.

Our novel preparation of AuPEI-FITC1 through a so-called “one-pot” synthesis, resulted in the formation of small nanospheres with an average gold core of 3 ± 1 nm. Preformed AuPEI NPs were prepared with the AuPEI6 protocol (see above). When these preformed AuPEI NPs were reacted with the same amount of FITC used for AuPEI-FITC1, similar sized NPs were obtained (AuPEI-FITC2). In the last two experiments, FITC was first linked to the polymer as a PEI-FITC conjugate

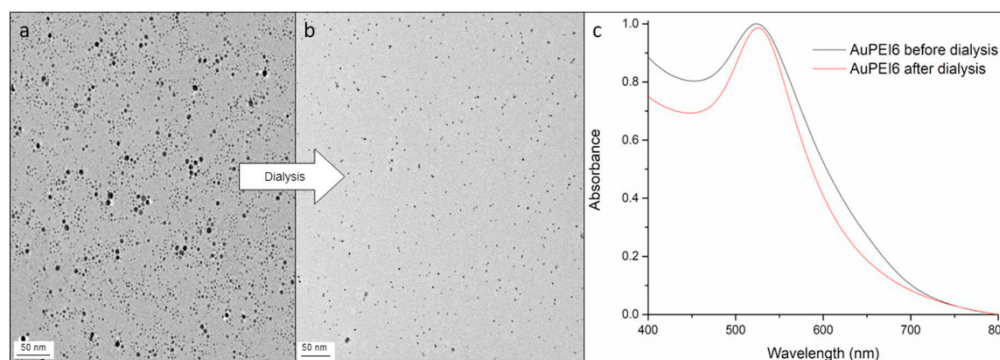


Fig. 3. Effect of purification *via* dialysis of AuPEI6. TEM micrographs of Au-NPs a: before and b: after dialysis. c: Absorbance data. The histograms and DLS measurements for the AuPEI6 NPs before and after dialysis are shown in Fig. S3, Supp. info.

and then either mixed with the preformed AuPEI NPs (for AuPEI-FITC4) or combined with an aqueous solution of KAuCl_4 followed by the reduction of the gold(III) precursor (for AuPEI-FITC3). For all cases, a microwave reaction at 100 °C using FITC is possible since the thiocyanate compound shows a decomposition temperature of 260 °C, according to thermogravimetric analysis results (Fig. S8).

In the case of AuPEI-FITC3, previously linking FITC to PEI resulted in the formation of a mixture of two species of NPs with slightly different sizes (Fig. 5c). Even though the PEI-FITC conjugate was purified to eliminate unbound components, there is the possibility that PEI remained either unlabeled or was separated from FITC during the thermal treatment. The parallel existence of both PEI and PEI-FITC in the solution is most likely responsible for two separate nucleation and growth processes of the Au colloids, which could result in different sized NP products. Similarly, a direct stabilization of Au-NPs by FITC instead of PEI cannot be ruled out due to the strong attraction of its thiocyanate group towards gold.

The presence of the fluorescent FITC marker on AuPEI NPs was confirmed using scanning transmission electron microscopy (STEM). Energy-dispersive X-ray spectroscopy (EDX) measurements in STEM mode were able to identify gold atoms corresponding to Au-NPs, as well as sulfur atoms from the FITC ligand in the same area. Both gold and sulfur signals are displayed in color-coded elemental maps in Figs. 6 and S9. Hence, the attachment of FITC to the surface of all AuPEI-FITC

NP samples was verified. Additionally, this attachment was verified to be pH resistant between pH 6 and 8, as proven for AuPEI-FITC1 NPs in different phosphate buffers (see Fig. S10).

Due to the high extinction coefficient of Au-NPs and the overlap of their surface plasmon resonance peak with the emission maximum of FITC at 517 nm (Fig. S5), a fluorescence resonance energy transfer (FRET) from FITC to the Au-NPs can be expected [30]. As FITC interacts with the Au-NPs, its fluorescence is severely quenched, which allows further confirmation of a successful functionalization of FITC onto the gold surface. Even though the same amount of FITC was used for all AuPEI-FITC synthesis reactions, fluorescence measurements displayed various degrees of quenching, most likely due to different interactions between FITC and gold atoms in each sample (Fig. S11a).

As expected, all AuPEI-FITC solutions exhibited a lower fluorescence than the FITC control, thereby supporting the attachment of FITC onto the NP surface. AuPEI-FITC1 and AuPEI-FITC3 showed similar fluorescence intensities, contrary to the other two samples. AuPEI-FITC2 exhibited the highest fluorescence intensity (still about 50% less than the FITC control) and AuPEI-FITC4 the lowest (75% less than FITC) of all four NP types. In this case, a lower fluorescence can be the result of a stronger quenching effect and/or a lower amount of FITC being attached to the gold surface. In order to rule out the fluorescence detection from “free” FITC in the solution, AuPEI-FITC samples were centrifuged and the spectra from their supernatants were also recorded

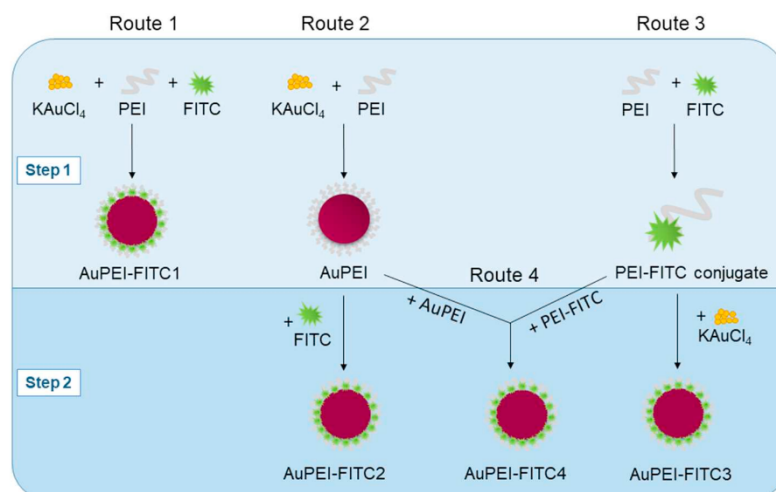


Fig. 4. Synthesis routes of AuPEI-FITC NPs.

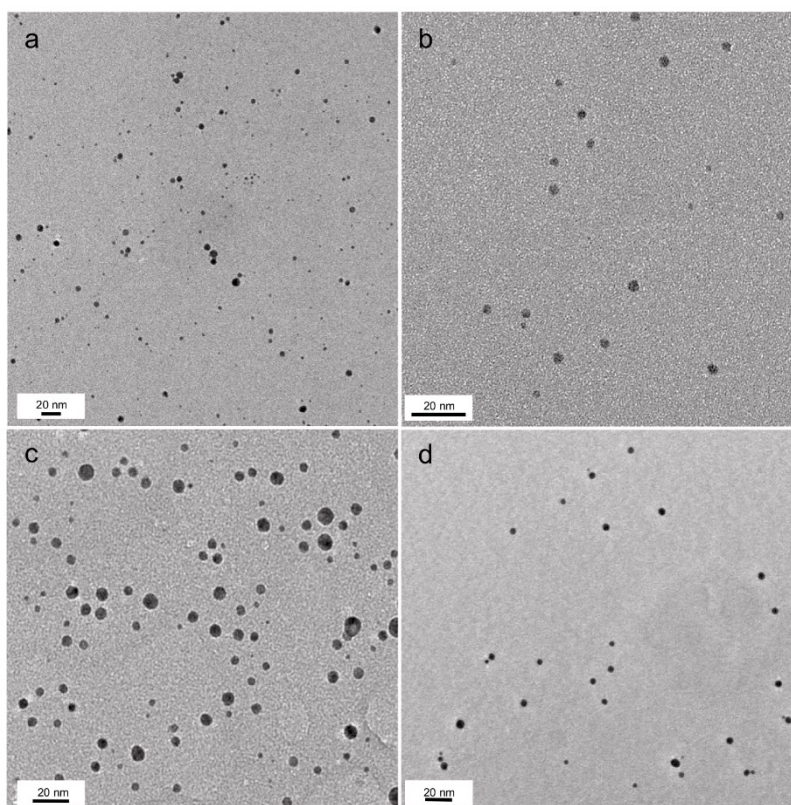


Fig. 5. TEM images of a: AuPEI-FITC1, b: AuPEI-FITC2, c: AuPEI-FITC3 and d: AuPEI-FITC4.

(Fig. S11b), showing no apparent fluorescence in the supernatants.

2.2. Cytotoxicity of AuPEI-FITC NPs

AuPEI-FITC NPs were incubated with the GBM cell lines GBM1, JHH520 and 407 at increasing concentrations for 1, 6, 12 and 24 h respectively (Fig. 7). Viability assays using the tetrazolium dye 3-(4,5-dimethylthiazol-2-yl)-2,5-diphenyltetrazolium bromide (MTT) showed that all AuPEI-FITC NPs have low impact on cell viability when added in concentrations between 0.25 and 2 mg/L, compared to untreated control cells. If NP treatment was extended for longer than 24 h, cytotoxicity of all four types of AuPEI-FITC NPs rose slightly. A possible

reason for this effect can be an increased NP size or gradual loss of stabilization of the nanomaterials in culture media. Thus, we tested the stability of AuPEI-FITC NPs incubated in Dulbecco's Modified Eagle Medium (DMEM). Fig. S13 shows a rise in NP size from 118 nm to 199 nm after 3 h until a stable size of approximately 243 nm is reached between 24 and 48 h and maintained for up to two weeks of incubation in DMEM, as seen before for citrate-capped Au-NPs [31]. The greater NP size is a result of the formation of a protein corona on the surface of the NPs as they come in contact with the different proteins contained in cell culture media [32]. However, we can guarantee a stable size of the AuPEI-FITC1 system for a prolonged biomedical application. This is an important finding given that the protein corona can significantly hinder

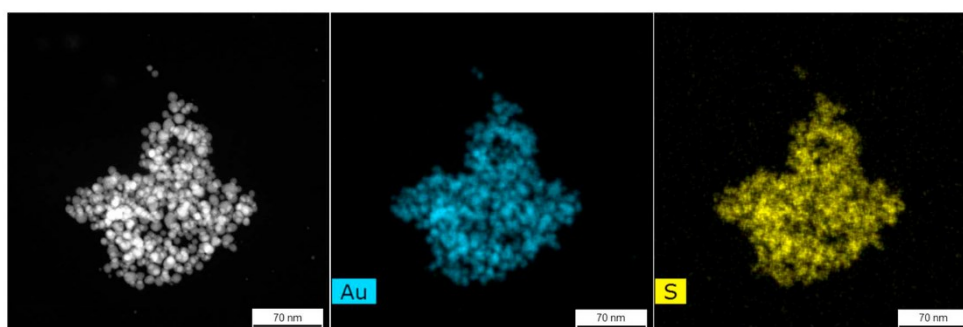


Fig. 6. STEM-EDX elemental maps of AuPEI-FITC3 showing gold (in blue) and sulfur (in yellow) atoms within the agglomerate of NPs.

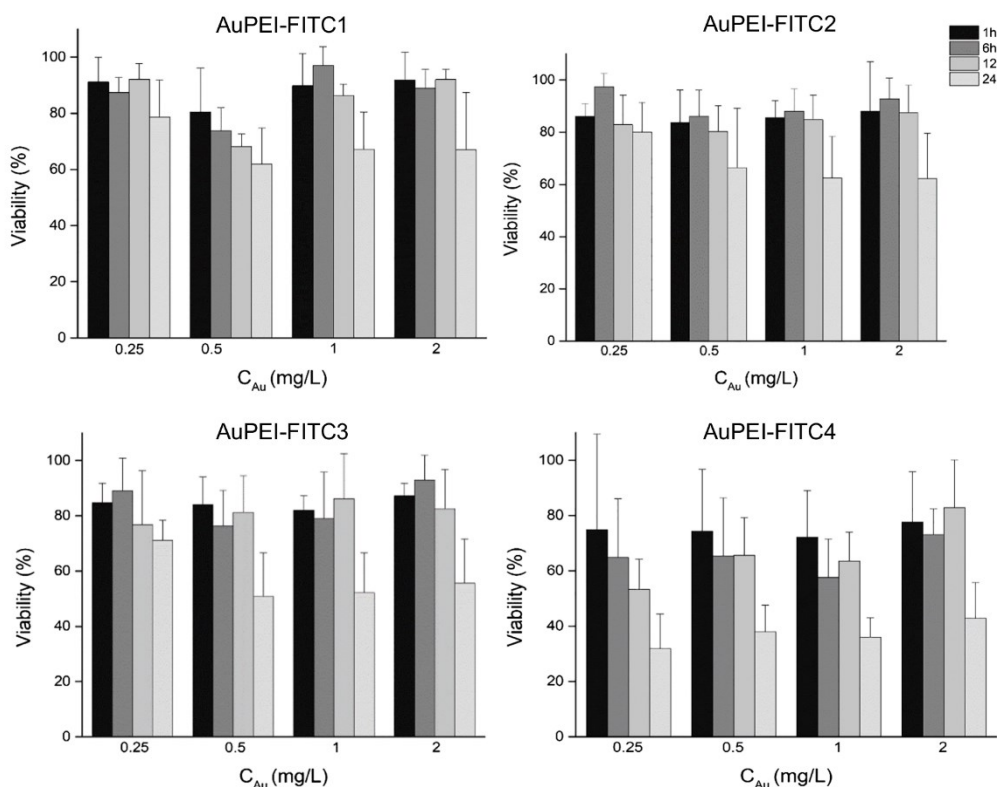


Fig. 7. Viability after 1, 6, 12 and 24 h incubation of GBM1, JHH520 and 407 cells with AuPEI-FITC NPs at increasing concentrations.

the internalization of NPs.

Other factors, such as changes in pH and ionic interactions during NP uptake processes ending in particle agglomeration and loss of their unique properties [33], could be also the reason for a lower cell viability after 24 h. Moreover, a polymer degradation and release of the PEI capping ligand from the NP surface inside the cell [34] would also account for an increased toxicity.

Additionally, our viability studies indicated some variations when incubating the same AuPEI-FITC NP sample in the different GBM cell lines. Thus, there is a dependence of the biocompatibility of AuPEI-FITC NPs on the cell type in which they were incubated. In consequence, the results displayed in Fig. 7 are sometimes widely spread around the mean value. When a mean of all concentrations and all incubation times in all cell lines was calculated (Fig. S14), AuPEI-FITC4 was identified as the least suitable for treatment with a maximum viability of only 61%. AuPEI-FITC3 showed a cell viability of 77%, whereas AuPEI-FITC1 and AuPEI-FITC2 showed values above 82%.

2.3. Uptake in glioblastoma stem-like cells

To investigate a possible uptake of AuPEI-FITC NPs into GBM stem-like cells, plated cells were investigated through a microscope after incubation, as shown in Fig. 8 for JHH520 cells treated with AuPEI-FITC4 NPs. The images in fluorescence correspond to the same area observed through a white light microscope (Fig. 8a). In these experiments, almost all neurospheres displayed fluorescent signals (Fig. 8b). This fluorescence is a result of the stable attachment of the FITC dye to the AuPEI NPs even after cell internalization. The stable dye attachment was verified through a spectroscopic investigation of the formerly internalized AuPEI-FITC1 NPs upon forced release from cells through

induced osmolysis (see Fig. S15 in SI).

To rule out cell autofluorescence and to differentiate between internalized and surface-bound (adsorbed) NPs, Trypan blue quenching [35,36] was applied to inhibit extracellular fluorescence (Fig. 8c). We observed a reduction of fluorescence intensity, yet some signals remained visible after the procedure. To quantify the internalization of the NPs, we used the quantitative signal detection technology of fluorescence-activated cell sorting (FACS). In the following the term “adsorbed” refers to AuPEI-FITC NPs adhering to outside of the cell membrane (surface-bound).

2.4. Internalization of AuPEI-FITC NPs

For quantification experiments, GBM cells were treated with AuPEI-FITC NPs and measured in a buffered solution. Fig. S16 displays exemplary FACS results of untreated GBM1 cells (a), cells after incubation with AuPEI-FITC NPs (b, c) and after addition of the extracellular fluorescence quencher Trypan blue (d, e). Untreated cells showed a side scatter (SSC) under $40 \cdot 10^3$ and values lower than 10^3 when results were separated based on their fluorescence intensity (FITC scale), which can be attributed to the autofluorescence of the cells. When treated with AuPEI-FITC NPs, a new cell population (B) appeared higher on the SSC scale because of the increased complexity of cells when exposed to NPs. This population corresponded to cells which have either adsorbed only or adsorbed and internalized fluorescent NPs. As expected, such population presented higher fluorescence values due to the incorporation of the FITC fluorophore into the system. After quenching with Trypan blue, population B decreased to reveal the actual percentage of cells which have internalized fluorescent AuPEI-FITC NPs; omitting the cells with extracellular NPs (Fig. S16d, e).

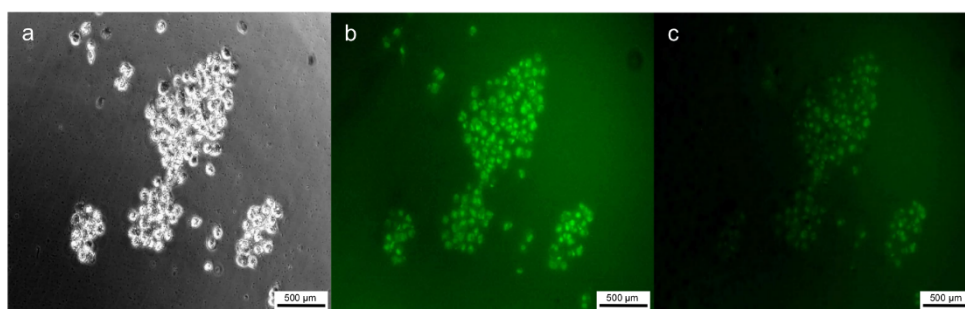


Fig. 8. Microscopic Images of JHH520 cell culture incubated with AuPEI-FITC4 NPs. Image b and c were taken using a fluorescent filter. Image b depicts the cells with adsorbed and internalized AuPEI-FITC4 NPs. Image c was taken after extracellular fluorescence quenching with Trypan blue, hence, depicts the residual internalized AuPEI-FITC4 NPs.

Moreover, analogous FSC intensities were found in both treated and untreated cells. This demonstrates again the low toxicity of our samples given that such intensity is highly dependent on cell death processes such as apoptosis.

In agreement with MTT results, FACS tests also indicated that not all cell lines react in the same way to a treatment with AuPEI-FITC NPs (Table 1). While up to 77% of JHH520 cells showed FITC fluorescence before quenching, GBM1 cells reached an adsorption plus internalization maximum of only 65% (with AuPEI-FITC4) and 407 cells yielded only 60% (with AuPEI-FITC3). From all cell lines, JHH520 cells lost the most percentage of fluorescence after quenching of the (extracellular) adsorbed AuPEI-FITC1–4 NPs. This observation highlights the importance of distinguishing between internalized and extracellular NP species. More importantly, the NP type played an even bigger role concerning their uptake in GBM cells (results after quenching). An average of the adsorbed plus internalized *versus* internalized only AuPEI-FITC NPs in all four cell lines is given at the end of Table 1. The most interesting observation was the lowest decrease in fluorescence intensity before and after quenching of AuPEI-FITC1, as well as its highest internalization average of 53% after only an hour, out of all AuPEI-FITC NP types. Thus, this vehicle possesses the best cellular uptake potential at low NP concentrations and is hypothesized as a good candidate for treatment delivery studies against GBM.

Compliant with viability results, AuPEI-FITC4 appeared to be the most unsuitable nanocarrier, given that only ~10% of the NPs could be internalized. This realization led us to examine the nature of AuPEI-FITC4 NPs more closely. HR-TEM images revealed a polymer accumulation around the Au-NPs, sometimes even joining several gold spheres into one large agglomerate (Fig. S17). The increased amount of PEI on the NP surface would also explain the low attachment of FITC onto the AuPEI NPs and hence its lesser fluorescence intensity (Fig. S11). AuPEI-FITC4 NPs were easily adsorbed through the higher quantities of PEI polymer of AuPEI6 and the addition of the PEI-FITC conjugate (Fig. 4). This construct most likely causes strong electrostatic interactions with the cell membrane, which is negatively charged. AuPEI-FITC4 also

presented the largest diameter and core size out of all AuPEI-FITC samples which probably hampers the internalization (Table S2). Overall, AuPEI-FITC4 NPs were incompatible with GBM cells, starting from their synthesis method, as they failed to well integrate the fluorescent FITC tracking system into our AuPEI NPs, contrary to the samples AuPEI-FITC1–3.

3. Conclusions

Four types of fluorescent Au-NPs with a PEI shell were reproducibly synthesized in a straight-forward manner using accessible starting materials. Gold cores sizes varied between 3 and 6 nm, according to the synthesis route. The novel one-pot method for obtaining fluorescent AuPEI-FITC NPs proved to be not only rapid and simple but also the most suitable gene vector for GBM stem-like cells. Experiments showed the importance of the synthesis method on the final morphology and internalization of gold nanocarriers. The one-pot synthesis where KAuCl_4 , PEI and FITC were reacted together proved to be superior to two-step syntheses where two out of the three reactants were pre-reacted before being combined with the third reagents. Even though the difficulty of internalization into GBM cells remains, more than the half of the cells got nanofected for each tested cell line. Thus, we presented a quick and simple-to-adjust tool for the development of molecular-targeting Au-NPs with high clinical translational properties. Given the high chemotherapy resistance of BCSC [37], our results are promising for further experiments to develop effective drug delivery devices to eradicate that highly malignant cell population. Moreover, molecular sub-classification of brain cancers revolutionizes current neuropathology [38]. Subtype specific susceptibilities of GBM to our nanotechnology may enhance the efficacy in certain tumors. Further studies are needed to investigate any association of delivery resistance and molecular subtype. In the future, we aim to contribute to improve treatment for GBM by developing drug-conjugated vehicles equipped with epitope-specific anchor proteins such as CD133 or CD44. Efforts to attach novel discovered anti-BCSC drugs to AuPEI-NPs are underway.

Table 1

Fraction of cells with adsorbed and internalized vs. internalized AuPEI-FITC NPs in different GBM cell lines.^a

Cell line	AuPEI-FITC1		AuPEI-FITC2		AuPEI-FITC3		AuPEI-FITC4	
	Adsorbed + internalized (%)	Internalized (%)	Adsorbed + internalized (%)	Internalized (%)	Adsorbed + internalized (%)	Internalized (%)	Adsorbed + internalized (%)	Internalized (%)
GBM1	63	61	56	29	52	7	65	9
JHH520	60	51	75	44	77	39	76	7
407	49	47	53	33	60	9	54	5
Average (all)	57	53	61	35	63	18	65	7

^a 500,000 cells were incubated with 1 mg/L AuPEI-FITC NPs in PBS for 1 h. The column “Adsorbed + internalized” refers to cells before quenching. The column “Internalized” gives the fraction of cells after addition of Trypan blue solution that is quenching the extracellular NPs.

4. Experimental

4.1. Materials and methods

Branched polyethylene imine (PEI) with an average molar mass of $M_w \sim 25,000$ g/mol, potassium tetrachloroaurate (III) and fluorescein isothiocyanate (FITC) were purchased from Sigma Aldrich and used without further purification. Water for the reactions was purified using the Milli-Q® purification system. Dialysis was performed using Spectra/Por® membranes from Spectrum Laboratories with a MWCO of 3.5 kDa and 50 kDa. To increase the water solubility of FITC, 50 mg (0.13 mmol) were solved in dimethyl sulfoxide (DMSO) (Honeywell, 99.7% purity) to create a FITC solution with a concentration of 4 mg/mL. This solution was then diluted to 0.05 mg/mL either in water (*FITC stock 1*) or PBS (Gibco, #10010015, Thermo Fisher Scientific, USA) buffer (*FITC stock 2*) before adding it to the nanoparticle synthesis reaction.

4.2. NP characterization

4.2.1. Transmission electron microscopy (TEM)

Sample preparation consisted on dropping 10 μ L of the gold solution onto a 200 μ m carbon-coated copper grid and allowing it to dry in air. TEM images were acquired on a FEI Tecnai G2 F20 electron microscope operated at 200 kV accelerating voltage and recorded with a Gatan UltraScan 1000P camera. This microscope was also used to record selected area electron diffraction (SAED) patterns. An area with sufficient material was put inside the round aperture and illuminated with wide-spread parallel beam to obtain focused diffraction patterns. Images were calibrated using Debye-Scherrer patterns recorded from a gold reference sample (S106, Plano GmbH, Wetzlar, Germany). High resolution TEM of gold NPs was performed using a Titan Themis 60-300 X-FEG microscope equipped with an image corrector and operated at 300 kV. Using the Gatan Digital Micrograph software, over 100 particles were counted to determine NP size and size distribution.

4.2.2. Scanning transmission electron microscopy (STEM)

STEM studies using a high-angle annular dark-field (HAADF) detector from 73 mrad to 350 mrad in combination with energy-dispersive X-ray (EDX) mapping were carried out in the Titan Themis 60-300 X-FEG microscope with a ~ 150 pA current, a convergence semi-angle of ~ 23.8 mrad and a beam size of ~ 0.1 nm.

4.2.3. Dynamic light scattering (DLS)

The hydrodynamic diameters of Au-NPs were determined using a Zetasizer instrument (Malvern Nano S Zetasizer) with a HeNe laser at a wavelength of 633 nm. Three measurements with four runs were assessed to calculate the mean size value.

4.2.4. Ultraviolet-visible spectroscopy (UV-VIS)

Gold nanoparticle samples were measured as synthesized on a UV-2450 spectrometer and analyzed using the UVProbe software, both from Shimadzu.

4.2.5. Fluorescence spectroscopy

300 μ L of gold solution were diluted in 3 mL PBS, placed in quartz glass cuvettes and measured on a FluoroMax-4 Spectrofluorometer from HORIBA Scientific with an excitation of 490 nm.

4.2.6. Thermogravimetric analysis (TGA)

FITC decomposition studies were carried out on a Netzsch TG209 F3 Tarsus (Netzsch, Selb, Germany) instrument under a nitrogen atmosphere with a ramp between 1 and 1000 °C.

4.3. Synthesis of PEI-coated gold nanoparticles (AuPEI)

50 mg (2 μ mol) of PEI were dissolved in 50 mL water and added to a round bottom flask containing a specific amount of the gold precursor KAuCl_4 corresponding to a $n_{\text{KAuCl}_4}/n_{\text{PEI}}$ molar ratio between 1 and 10. The yellow solution was placed in a microwave (CEM, Discover) equipped with a reflux unit and irradiated for 2 min at 100 °C and 300 W while stirring. Dialysis of the red solution was done against water for 24 h using a 50 kDa tube.

4.4. Synthesis of fluorescent gold nanoparticles (AuPEI-FITC)

4.4.1. AuPEI-FITC1

4.5 mg (12 μ mol) of KAuCl_4 and 5 mL of *FITC stock 1* were added to a solution of 50 mg (2 μ mol) of PEI dissolved in 50 mL of water and irradiated in the microwave for 2 min at 100 °C. Dialysis through a 50 kDa membrane against water for 24 h was performed as a purification step.

4.4.2. AuPEI-FITC2

4.5 mg (12 μ mol) of KAuCl_4 were added to a solution of 50 mg (2 μ mol) of PEI dissolved in 50 mL of water, irradiated in the microwave for 2 min at 100 °C and dialyzed through a 50 kDa membrane against water for 24 h. 5 mL of *FITC stock 1* were added to the AuPEI NP solution, stirred at room temperature for 8 h and dialyzed through a 3.5 kDa membrane against PBS for 24 h.

4.4.3. AuPEI-FITC3

5 mL of *FITC stock 2* were added to a solution of 50 mg (2 μ mol) of PEI in 50 mL of PBS. The FITC-PEI solution was stirred at room temperature for 8 h and dialyzed through a 3.5 kDa membrane against PBS for 24 h. Afterwards, 4.5 mg (12 μ mol) of KAuCl_4 were added, the solution was irradiated for 2 min at 100 °C and dialyzed through 3.5 kDa membrane against PBS for 24 h.

4.4.4. AuPEI-FITC4

4.5 mg (12 μ mol) of KAuCl_4 were added to a solution of 50 mg (2 μ mol) of PEI dissolved in 50 mL of water, irradiated in the microwave for 2 min at 100 °C and dialyzed through a 50 kDa membrane against water for 24 h. Volume was adjusted to 40 mL. 5 mL of *FITC stock 2* were added to a solution containing 50 mg (12 μ mol) of PEI in 10 mL of PBS, stirred at room temperature for 8 h and dialyzed through a 3.5 kDa membrane against PBS for 24 h. AuPEI NP and FITC-PEI solutions were combined, stirred at room temperature for 8 h and dialyzed through a 3.5 kDa membrane against PBS for 24 h.

For synthesis details about samples AuPEI-FITC5-10, refer to Table S1 in Supp. info.

4.5. Cell cultures

Human embryonic kidney (HEK) cells are cultured in Dulbecco's Modified Eagle Medium (DMEM) without pyruvate (Gibco, #11965092, Thermo Fisher Scientific, USA) supplemented with 10% fetal calf serum (Gibco, #26140079, Thermo Fisher Scientific, USA). Glioma (BCSC) cells JHH520 cells were generously provided by G. Riggins (Baltimore, USA), GBM1 by A. Vescovi (Milan, Italy) and 407 by M.S. Carro (Freiburg, Germany). BCSC neurospheres were cultured in DMEM without pyruvate (Gibco, #11965092, Thermo Fisher Scientific, USA), 30% Ham's F12 Nutrient Mix (Gibco, #11765047), 2% B27 supplement (Gibco, #17504044), 20 ng/mL human basic fibroblast growth factor (Peprotech, #AF-100-18B, USA), 20 ng/mL human epidermal growth factor (Peprotech, #AF-100-15), 5 μ g/mL Heparin (Sigma, #H0878, Merck KGaA, Germany). Both media contained 1 \times Antibiotic-Antimycotic (Gibco, #15240096). Cells are tested for their absence of mycoplasma contamination and validated for their genetic identity using short tandem repeat analysis similar as described before

using the core facility service of our institute [21].

4.6. Cell viability assay

96-well plates were coated with a laminin-PBS solution (1:20 v:v) (Sigma-Aldrich, # 2020, Germany) and left to dry in the sterile working bench. Each well was loaded with 20,000 GBM cells suspended in 100 μ L culture medium. After successful cell adhesion on the bottom, medium was removed from each well and cells were incubated for 1, 6, 12 and 24 h with a nanoparticle:medium dilution at different concentrations. The gold concentration of the nanoparticle solutions was estimated assuming that all 12 μ mol of KAuCl_4 were completely reduced to Au^0 . A solution of 5 mg/mL MTT in PBS was diluted 1:10 in medium and added to each well (100 μ L) after removal of the nanoparticle dilutions and washing each well with PBS. Allowing 90 min reaction time, MTT was taken out and 50 μ L DMSO were pipetted to release the purple color. Absorbance was measured at 550 nm on an iMark™ Microplate Reader using the Microplate Manager® software from Biorad.

4.7. Nanoparticle uptake by GBM cells

500,000 glioblastoma cells were suspended in 500 μ L PBS and incubated with nanoparticle dilutions at 1 mg/L for 1 h. To quench extracellular fluorescence, a 0.4% Trypan Blue solution (Sigma-Aldrich, # T8154, Germany) was added to the cell suspension in a 1:3 volume ratio. FACS measurements were performed on a BD FACSCanto™ flow cytometer equipped with blue (488 nm, air-cooled, 20 mW solid state) and red (633 nm, 17 mW HeNe) excitation sources and the FACSDiva™ software. Kaluza Analysis Software from Beckman Coulter was used for further analysis of scattering plots.

Declaration of competing interest

The authors declare that they have no known competing financial interests or personal relationships that could have appeared to influence the work reported in this paper.

Acknowledgments

The authors thank N. Stoecklein, Department of Surgery, Universitätsklinikum Düsseldorf (UKD) and his team for the technical support and providing the FACS infrastructure. We acknowledge Dr. Juri Barthel at the Ernst Ruska-Centre, Forschungszentrum Jülich GmbH (FZ Jülich), Germany for his technical support at the TEM facility under project number ER-C A-060. We thank Dr. Dirk Bier from FZ Jülich and Dr. Evmorfia Petropoulou from UKD for their helpful knowledge and help in this project. U.D. Kahlert thanks H.J. Steiger for his continuous support.

Appendix A. Supplementary data

The Supporting Information contains IR spectra, size and size distributions for NPs, details on synthesis and purification, viability plots, UV-Vis spectra, STEM-EDX for AuPEI-FITC NPs, stability characterizations, determinations of ratio of fluorescent NPs and of amounts of AuNPs in cells. Supplementary data to this article can be found online at <https://doi.org/10.1016/j.jinorgbio.2019.110952>.

References

- [1] U.D. Kahlert, S.M. Mooney, M. Natsumeda, H.-J. Steiger, J. Maciaczyk, *Int. J. Cancer* 140 (2017) 10–22.
- [2] Y. Yang, I.-Y. Hsieh, X. Huang, J. Li, W. Zhao, *Front. Pharmacol.* 7 (2016) 477.
- [3] J.D. Lathia, S.C. Mack, E.E. Mulkearns-Hubert, C.L.L. Valentim, J.N. Rich, *Genes Dev.* 29 (2015) 1203–1217.
- [4] B.G. Harder, M.R. Blomquist, J. Wang, A.J. Kim, G.F. Woodworth, J.A. Winkles, J.C. Loftus, N.L. Tran, *Front. Oncol.* 8 (2018) 462.
- [5] S.S. Kim, A. Rait, F. Rubab, A.K. Rao, M.C. Kiritry, K.F. Pirolo, S. Wang, L.M. Weiner, E.H. Chang, *Mol. Ther.* 22 (2014) 278–291.
- [6] A. Orza, O. Sorişău, C. Tomuleasa, L. Olenic, A. Florea, O. Pana, I. Bratu, E. Pall, S. Florian, D. Casciano, A. Biris, *Int. J. Nanomedicine* 8 (2013) 689–702.
- [7] I. Naletova, L.M. Cucci, F. D'Angeli, C.D. Anfuso, A.M. Magri, D. La Mendola, G. Lupo, C. Satriano, *Cancers* 11 (2019) 1322, <https://doi.org/10.3390/cancers11091322>.
- [8] T.-M. Sun, Y.-C. Wang, F. Wang, J.-Z. Du, C.-Q. Mao, C.-Y. Sun, R.-Z. Tang, Y. Liu, J. Zhu, Y.-H. Zhu, X.-Z. Yang, J. Wang, *Biomaterials* 35 (2014) 836–845.
- [9] Y. Zhong, C. Wang, R. Cheng, L. Cheng, F. Meng, Z. Liu, Z. Zhong, *J. Control. Release* 95 (2014) 63–71.
- [10] G. Yang, S. Xiang, K. Zhang, D. Gao, C. Zheng, F. Zhao, *Int. J. Clin. Exp. Med.* 9 (2016) 753–759.
- [11] D.Y. Joh, L. Sun, M. Stangl, A.A. Zaki, S. Murty, P.P. Sautoiemma, J.J. Davis, B.C. Baumann, M. Alonso-Basanta, D. Bhang, G.D. Kao, A. Tsourkas, J.F. Dorsey, *PLoS One* 8 (2013) e62425, <https://doi.org/10.1371/journal.pone.0062425>.
- [12] L. Bobyk, M. Edouard, P. Deman, M. Vautrin, K. Pernet-Gallay, J. Delarochéa, J.-F. Adam, F. Estève, J.-L. Ravanat, H. Elleaume, *Nanomed.-Nanotechnol.* 9 (2013) 1089–1097.
- [13] M.F. Kircher, A. de la Zerda, J.V. Jocker, C.L. Zavaleta, P.J. Kempen, E. Mittra, K. Pitter, R. Huang, C. Campos, F. Habte, R. Sinclair, C.W. Brennan, I.K. Mellinshoff, E.C. Holland, S.S. Gambhir, *Nat. Med.* 18 (2012) 829–834.
- [14] W. Shang, C. Zeng, Y. Du, H. Hui, X. Liang, C. Chi, K. Wang, Z. Wang, J. Tian, *Adv. Mater.* 29 (2017) 1604381.
- [15] X. Gao, Q. Yue, Z. Liu, M. Ke, X. Zhou, S. Li, J. Zhang, R. Zhang, L. Chen, Y. Mao, C. Li, *Adv. Mater.* 29 (2017) 1603917.
- [16] L. Zhao, S. Wen, M. Zhu, D. Li, Y. Xing, M. Shen, X. Shi, J. Zhao, *Artif. Cell Nanomed. B.* 46 (2018) 488–498.
- [17] I. Fratoddi, I. Venditti, C. Cametti, M.V. Russo, *J. Mater. Chem. B* 2 (2014) 4204–4220.
- [18] M. Saito, H. Saitoh, *Biosci. Biotechnol. Biochem.* 76 (2012) 1777–1780.
- [19] X. Sun, S. Dong, E. Wang, *J. Colloid Interface Sci.* 288 (2005) 301–303.
- [20] S.-C. Wei, P.-H. Hsu, Y.-F. Lee, Y.-W. Lin, C.-C. Huang, *ACS Appl. Mater. Interfaces* 4 (2012) 2652–2658.
- [21] U.D. Kahlert, A.K. Suwala, E.H. Raabe, F.A. Siebzehrnubel, M.J. Suarez, B.A. Orr, E.E. Bar, J. Maciaczyk, C.G. Eberhart, *Brain Pathol.* 25 (2015) 724–732.
- [22] B. Devika Chithrani, A. Ghazani, W. Chan, *Nano Lett.* 6 (2006) 662–668.
- [23] T.D. Fernández, J.R. Pearson, M.P. Leal, M.J. Torres, M. Blanca, C. Mayorga, X. Le Guével, *Biomaterials* 43 (2015) 1–12.
- [24] E.C. Cho, L. Au, Q. Zhang, Y. Xia, *small* 6 (2010) 517–522.
- [25] E. Panzarini, S. Mariano, E. Carata, F. Mura, M. Rossi, L. Dini, *Int. J. Mol. Sci.* 19 (2018) 1305–1325.
- [26] W.J. Song, J.Z. Du, T.M. Sun, P.Z. Zhang, J. Wang, *small* 6 (2010) 239–246.
- [27] M. Ortega-Muñoz, M. Giron-Gonzalez, R. Salto-Gonzalez, A. Jodar-Reyes, S. De Jesus, F. Lopez-Jaramillo, F. Hernandez-Mateo, F. Santoyo-Gonzalez, *Chem. Asian J.* 11 (2016) 3365–3375.
- [28] M. Thomas, A.M. Klibanov, *PNAS* 100 (2003) 9138–9143.
- [29] H.S. Choi, W. Liu, P. Misra, E. Tanaka, J.P. Zimmer, B.I. Ipe, M.G. Bawendi, J.V. Frangioni, *Nat. Biotechnol.* 25 (2007) 1165.
- [30] S. Wang, X. Wang, Z. Zhang, L. Chen, *Colloids Surf. A Physicochem. Eng. Asp.* 468 (2015) 333–338.
- [31] G. Maiorano, S. Sabella, B. Sorce, V. Brunetti, M.A. Malvindi, R. Cingolani, P.P. Pompa, *ACS Nano* 4 (2010) 7481–7491.
- [32] X. Cheng, X. Tian, A. Wu, J. Li, J. Tian, Y. Chong, Z. Chai, Y. Zhao, C. Chen, C. Ge, *ACS Appl. Mater. Interfaces* 7 (2015) 20568–20575.
- [33] B. Halamoda-Kenzaoui, M. Ceridono, P. Urbán, A. Bogni, J. Ponti, S. Gioria, A. Kinsner-Ovaskainen, *J. Nanobiotechnol.* 15 (2017) 48.
- [34] S. Honary, F. Zahir, *Trop. J. Pharm. Res.* 12 (2013) 255–264.
- [35] J. Hed, G. Hallden, S.G. Johansson, P. Larsson, *J. Immunol. Methods* 101 (1987) 119–125.
- [36] S. Vranic, N. Boggetto, V. Contremoulins, S. Mornet, N. Reinhardt, F. Marano, A. Baeza-Squiban, S. Boland, *Part. Fibre Toxicol.* 10 (2013) 2, <https://doi.org/10.1186/1743-8977-10-2>.
- [37] A. Eramo, L. Ricci-Vitiani, A. Zeuner, R. Pallini, F. Lotti, G. Sette, E. Pilozzi, L.M. Larocca, C. Peschle, R. De Maria, *Cell Death Differ.* 13 (2006) 1238–1241.
- [38] D. Capper, D.T.W. Jones, M. Sill, V. Hovestadt, D. Schrimpf, D. Sturm, et al., *Nature* 555 (2018) 469–474, <https://doi.org/10.1038/nature26000>.

Supporting Information

Influence of synthesis methods on the internalization of fluorescent gold nanoparticles into glioblastoma stem-like cells

Beatriz Giesen^a, Ann-Christin Nickel^b, Alba Garzón Manjón^c, Andrés Vargas Toscano^b, Christina Scheu^c, Ulf Dietrich Kahlert^{b,d,*}, Christoph Janiak^{a,*}.

^a Institut für Anorganische Chemie und Strukturchemie, Heinrich-Heine-Universität Düsseldorf, 40204 Düsseldorf, Germany.

janiak@uni-duesseldorf.de, beatriz.giesen@uni-duesseldorf.de

^b Clinic for Neurosurgery, Medical Faculty, Heinrich-Heine University Dusseldorf, 40225 Dusseldorf, Germany.

ann-christin.nickel@med.uni-duesseldorf.de, andres.vargastoscano@med.uni-duesseldorf.de

^c Max-Planck-Institut für Eisenforschung GmbH, Max-Planck-Straße 1, 40237 Düsseldorf, Germany. scheu@mpie.de, a.garzon@mpie.de

^d Deutsches Konsortium für Translationale Krebsforschung (DKTK), Essen/Düsseldorf, Germany. ulf.kahlert@med.uni-duesseldorf.de

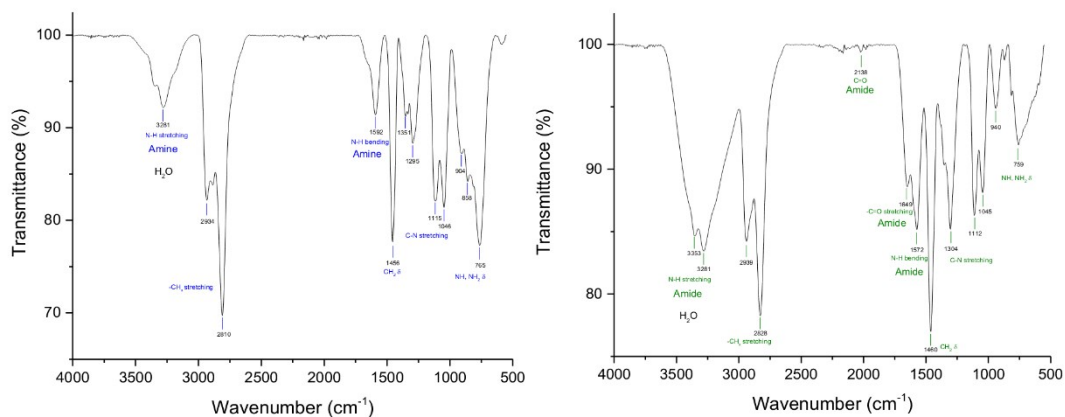


Fig. S1. IR Spectra of PEI (left) and AuPEI6 (right).

Compared to the spectrum of PEI, Au-NPs capped with PEI (AuPEI NPs) showed the appearance of a band at $\tilde{\nu}=1649\text{ cm}^{-1}$, corresponding to the C=O stretching of an amide function. Moreover, the amine N-H bend at $\tilde{\nu}=1592\text{ cm}^{-1}$ of PEI shifted to $\tilde{\nu}=1572\text{ cm}^{-1}$, corresponding to an amide N-H bend, after its reaction with KAuCl_4 .

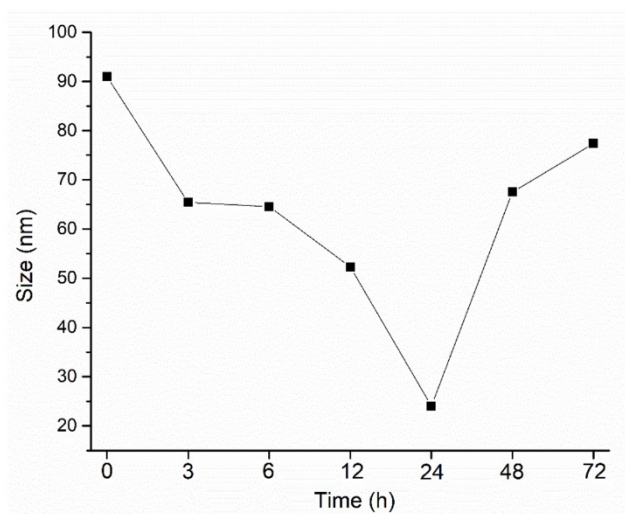


Fig. S2. Dependence of NP size by variation of dialysis time for AuPEI6.

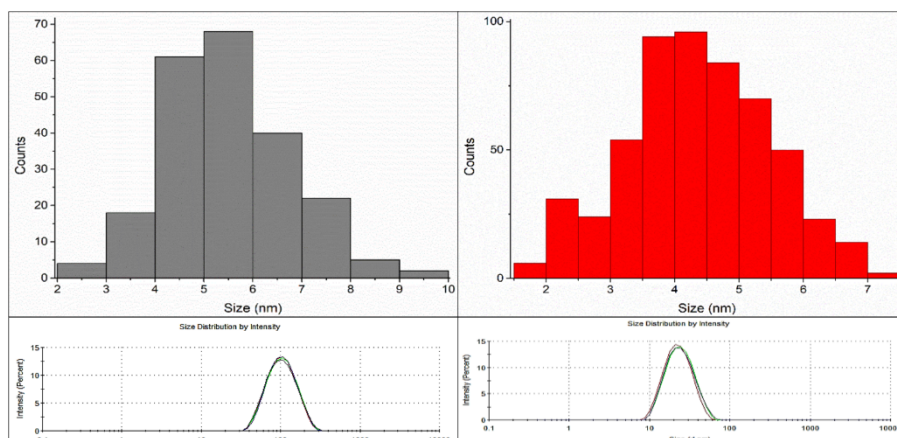


Fig. S3. Histograms and DLS measurements for AuPEI6 NPs before (left) and after dialysis (right).

Table S1. Synthesis and Purification Approaches for AuPEI-FITC NPs.

Entry	Sample name	C _{FITC} [mg/L]	Reaction medium	Dialysis
1	AuPEI-FITC1	4	water	water
2	AuPEI-FITC2	4	water	PBS
3	AuPEI-FITC3	4	PBS	PBS
4	AuPEI-FITC5	4	water	water
5	AuPEI-FITC6	40	water (Au) + PBS (PEI-FITC)	PBS
6	AuPEI-FITC7	40	water (Au) + PBS (PEI-FITC)	1. water 2. PBS
7	AuPEI-FITC4	4	water (AuPEI)+ PBS (PEI-FITC)	PBS
8	AuPEI-FITC8	4	water	water
9	AuPEI-FITC9	8	water	PBS
10	AuPEI-FITC10	40	water (AuPEI)+ PBS (PEI-FITC)	PBS

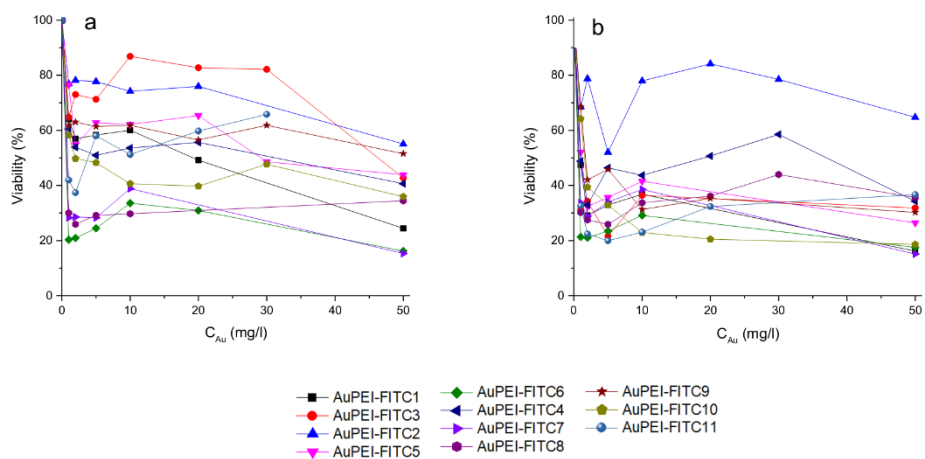


Fig. S4. Viability of AuPEI-FITC NPs in HEK cells after 1 (a) and 3 h (b).

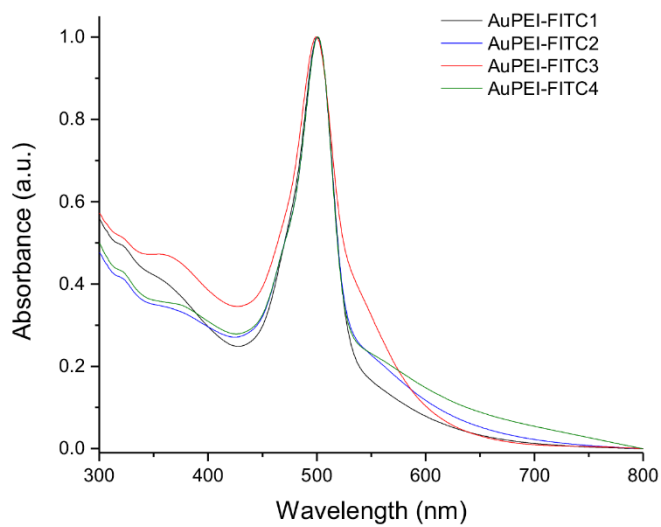


Fig. S5. UV-VIS Spectra of AuPEI-FITC NPs.

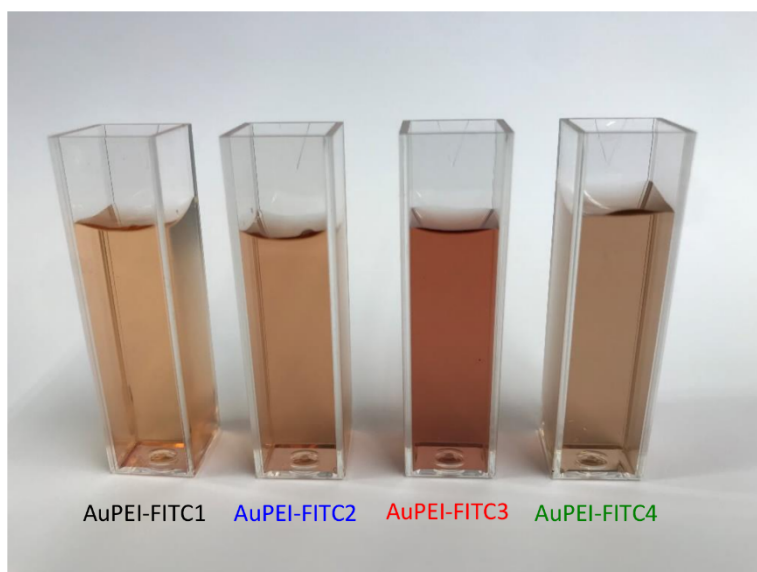


Fig. S6. AuPEI-FITC NPs solutions.

Table S2. Size of fluorescent AuPEI NPs determined by DLS and TEM.

Nanoparticle Sample	Size (nm)	
	TEM	DLS
AuPEI-FITC1	3 ± 1	118
AuPEI-FITC2	4 ± 1	47
AuPEI-FITC3	3 ± 1	115
AuPEI-FITC4	6 ± 2	129

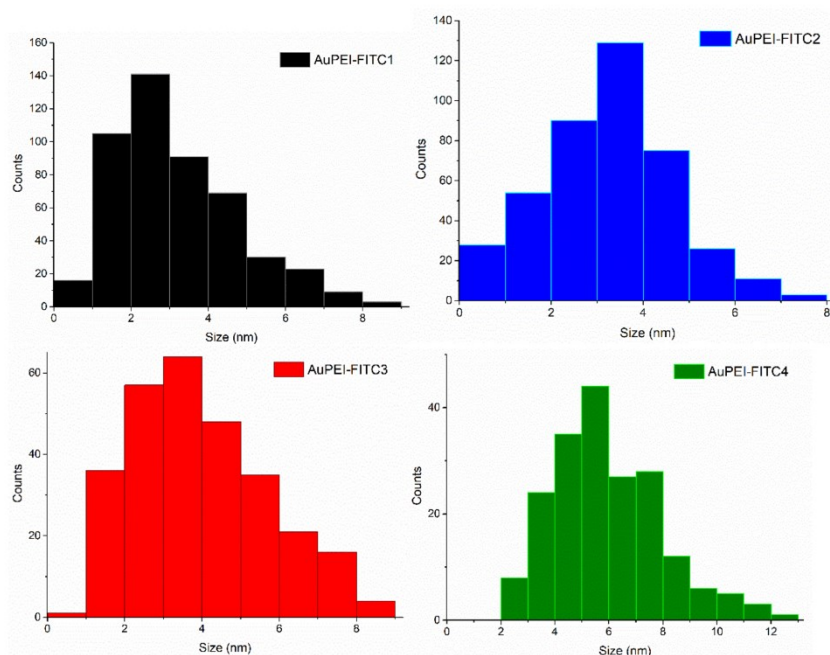


Fig. S7. Size distribution of AuPEI-FITC NPs.

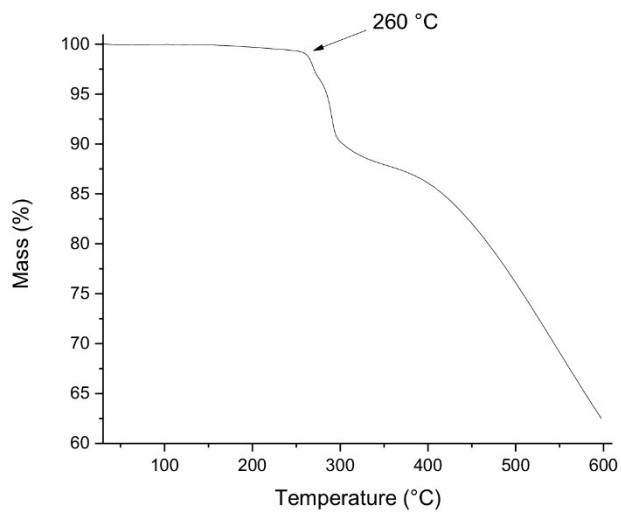


Fig. S8. Thermogravimetric analysis of FITC.

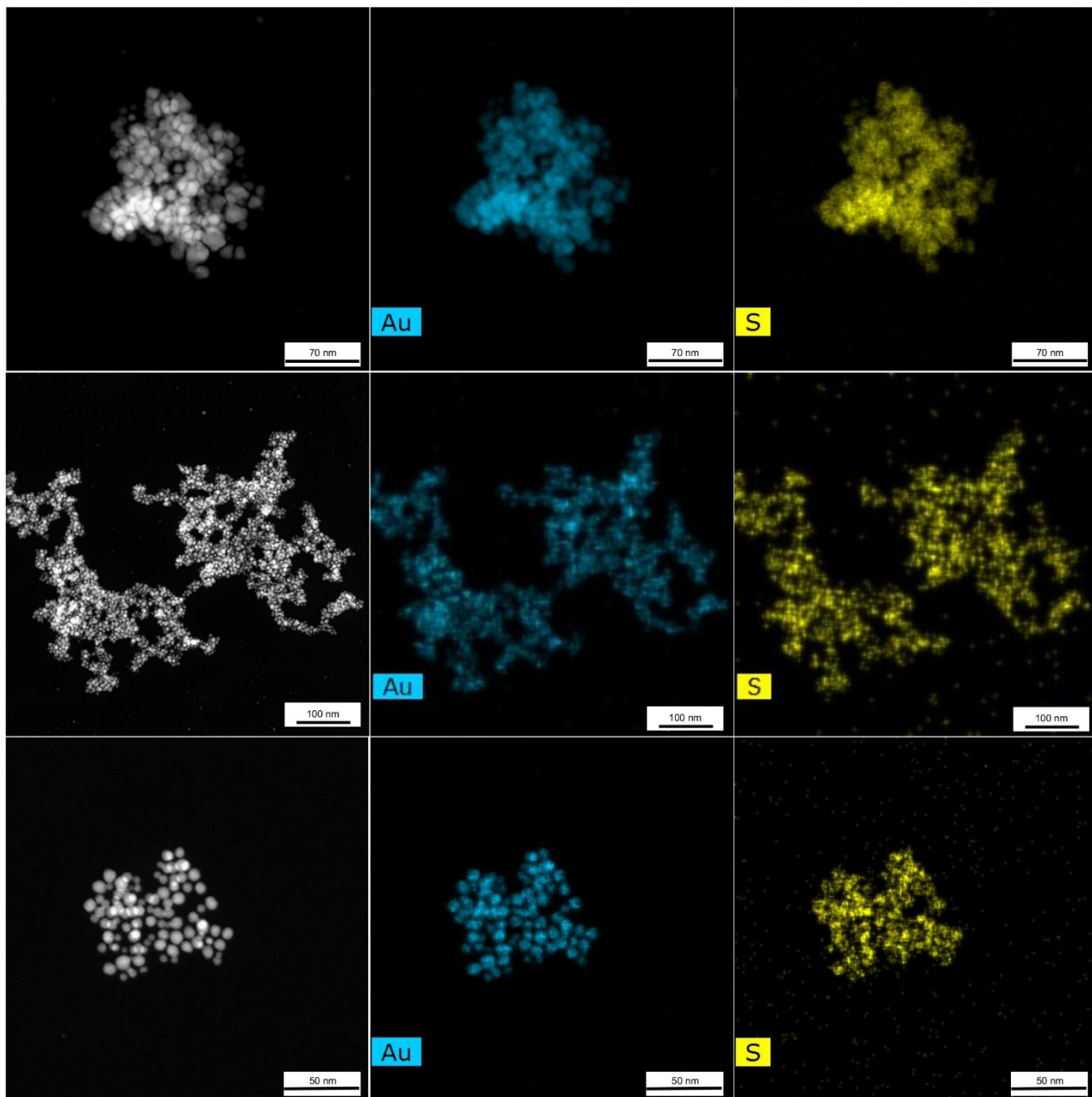


Fig. S9. STEM-EDX from AuPEI-FITC1 (top), AuPEI-FITC2 (middle) and AuPEI-FITC4 (bottom).

pH Resistance of FITC attachment to Au

AuPEI-FITC1 NPs were incubated in potassium phosphate buffers with pH values of 6, 6.5, 7, 7.5 and 8. After centrifugation (20000 rpm, 20 min), UV-VIS measurements of supernatants were performed, showing no unbound FITC at 465 nm.

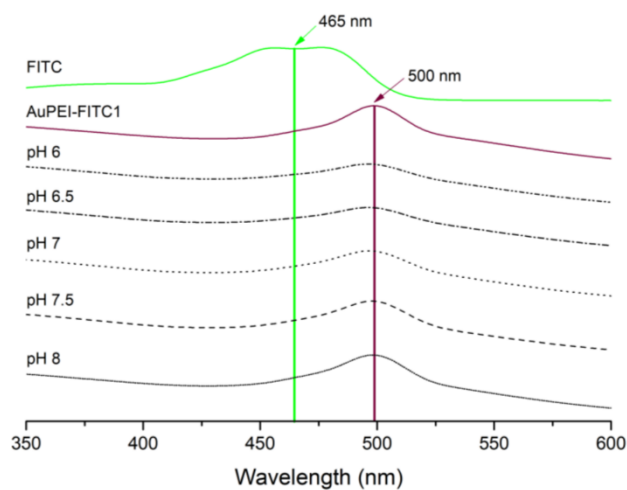


Fig. S10. UV-VIS measurements of AuPEI-FITC1 supernatants after incubation in different phosphate buffers with pH variation. The spectra of “free” FITC (green) is for comparison only, to show, that the supernatants do not give an absorption in this region. AuPEI-FITC1 (in wine red) is the reference spectrum for the as-synthesized sample as a solution in water. pH 6-8 refer to AuPEI-FITC1 NPs incubated in buffers at those pH values.

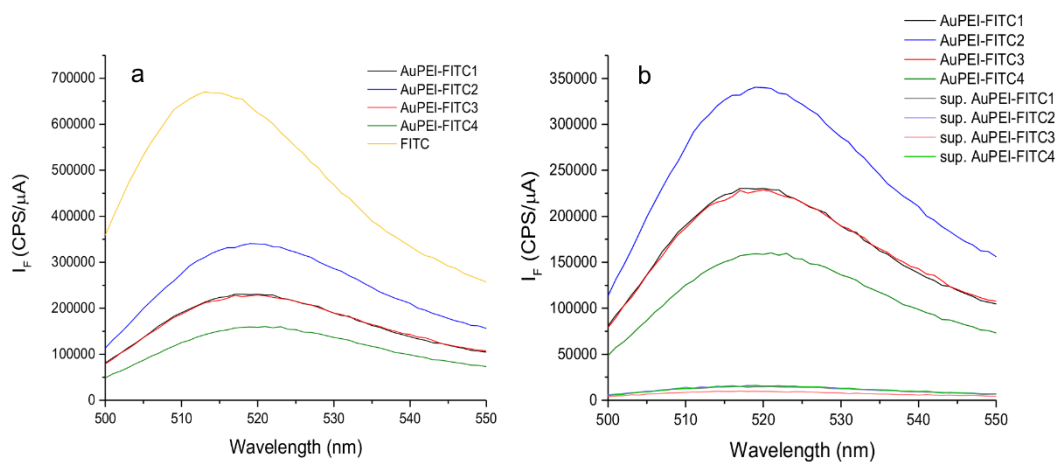


Fig. S11. Fluorescence spectra of AuPEI-FITC NPs.

Ratio of fluorescent NPs

The question of what percentage of NPs were fluorescent, was tackled by measuring FACS of one of our AuPEI-FITC NPs in solution.

In the flow cytometry scatter and gating plots of AuPEI-FITC4 NPs (Fig. S12 a), NPs appeared as a single population. However, when were separated based on their fluorescence intensity (Fig. S12 b, Count-FITC graph), we could distinguish between non-fluorescent (A) and fluorescent (B) NPs. The calculated percentage of AuPEI-FITC NPs for AuPEI-FITC4 was 52% non-fluorescent and 48% fluorescent. According to the fluorescence spectra in Fig. S11, AuPEI-FITC4 was the least fluorescent sample. The NPs AuPEI-FITC1-3 all had higher fluorescent intensities. Thus, we conclude that at least 50% of all NPs are fluorescent.

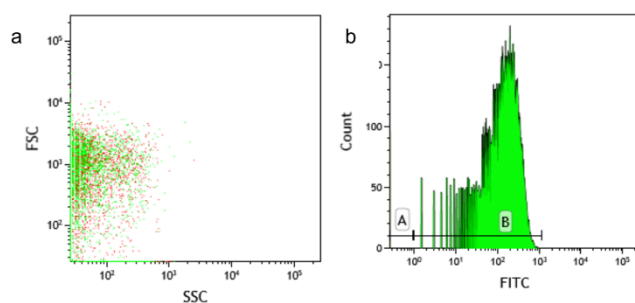


Fig. S12. Flow cytometry scatter and gating plots of AuPEI-FITC4 NPs. Population A (in red) represents NPs without fluorescence and B (in green) fluorescent NPs.

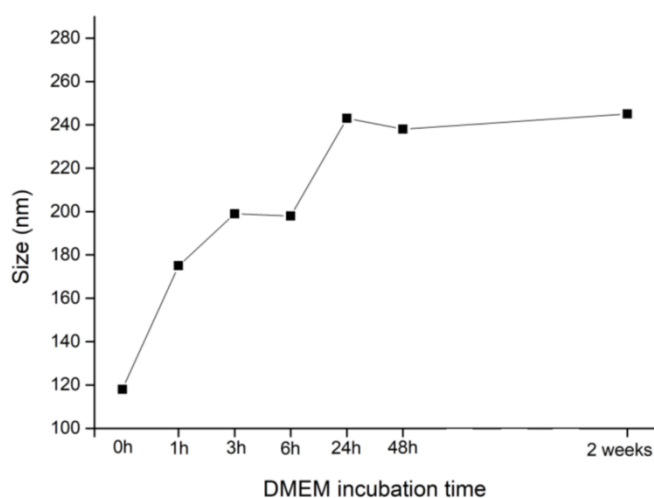


Fig. S13. Time dependent size increase of AuPEI-FITC1 NPs after incubation in DMEM culture media. Hydrodynamic diameter was determined using DLS.

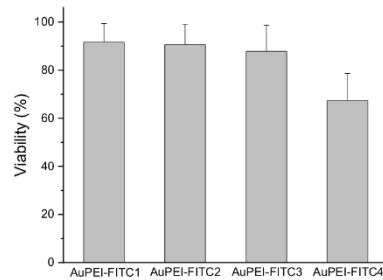


Fig. S14. Viability of all cell lines after incubation with AuPEI-FITC NPs. All concentrations and times were included in the mean calculation.

Stability of FITC attachment to Au after cell internalization

20 000 JHH520, 407 and GBM1 cells were incubated with AuPEI-FITC1 NPs and separated from the media by centrifugation (1080 rpm, 5 min). The cell pellets were washed with PBS to remove any remaining NPs on the surface and centrifuged again. Pellets were now dispersed in water to cause bursting of cell membranes and the release of internalized AuPEI-FITC NPs. High speed centrifugation (20000rpm, 20 min) isolated the remaining cells and NPs from their supernatants. UV-VIS measurements of these supernatants did not show (“free”) FITC absorption signals. Given that FITC dye which is not attached to Au-NPs (“free” FITC) does not precipitate at the chosen centrifugation speed, there is no significant loss of dye from the AuPEI-FITC NPs after internalization into GBM cells.

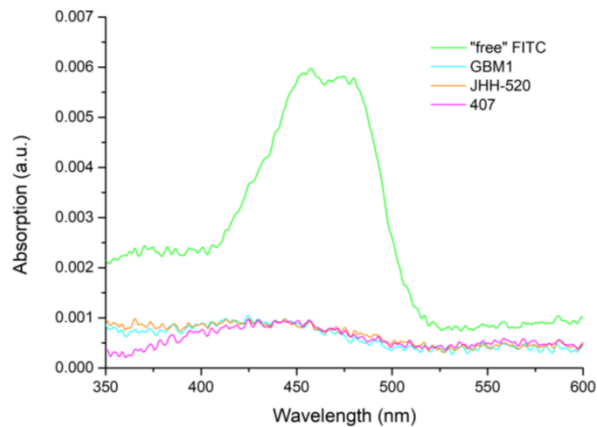


Fig. S15. UV-VIS spectra of cell supernatants after induced osmolysis of cells (JHH520, 407 and GBM1) with internalized AuPEI-FITC1 NPs. The spectrum of “free” FITC (green) is for comparison only, to show, that the cell supernatants do not give an absorption in this region.

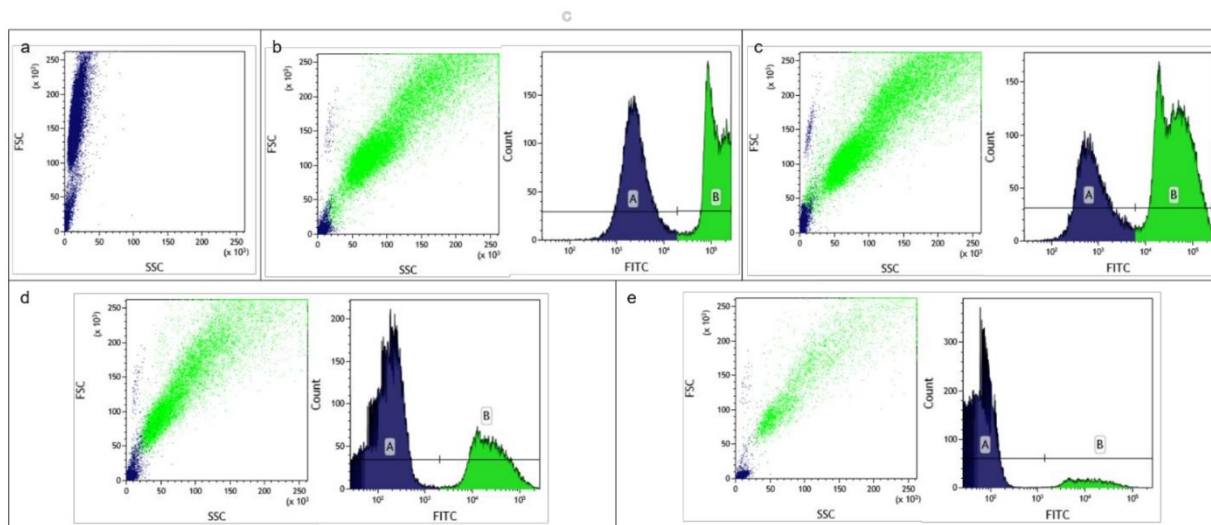


Fig. S16. Flow cytometry scatter and gating plots of GBM cells. a: untreated GBM1 cells, b: GBM1 cells treated with AuPEI-FITC2, c: GBM1 cells treated with AuPEI-FITC4, d: GBM1 cells treated with AuPEI-FITC2 after extracellular fluorescence quenching, e: GBM1 cells treated with AuPEI-FITC4 after Trypan blue quenching. Population A represents cells without fluorescent AuPEI-FITC NPs and B cells containing NPs.

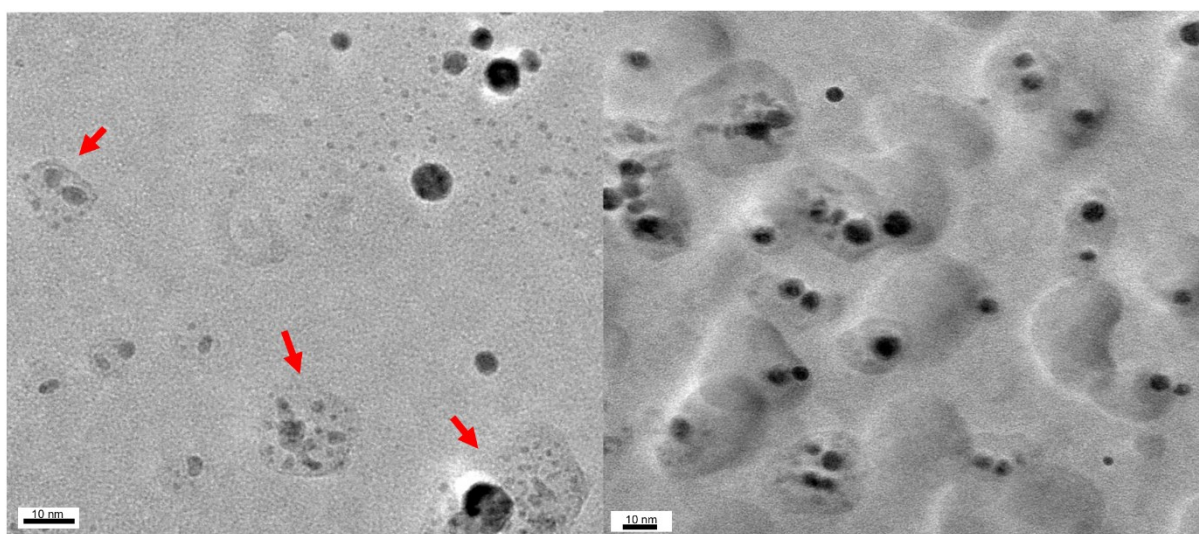


Fig. S17. HR-TEM images of AuPEI-FITC4 showing polymer accumulation (red arrows), right image taken in defocus to visualize polymer film.

Amount of NPs per cell

The most appropriate method of quantification to answer this question would be an inductively coupled plasma mass spectrometry (ICP-MS) measurement equipped with a single particle mode [1], to which we unfortunately do not access to in our institute.

Yet, for our small nanoparticles of about 3 nm Au-core diameter an ICP-MS measurement would still present a challenge, as the minimum measurable diameter for NPs has been given as 18 nm for most instruments [2].

On the other hand, a quantification through microscopy methods by counting NPs inside the cell would also be highly complex due to the small size of the AuPEI-FITC NPs (<5 nm). Nevertheless, we provide here an estimation based on a theoretical calculation and atomic absorption spectroscopy (AAS) for AuPEI-FITC1 NPs in all three GBM cell lines.

One million JHH520, 407 and GBM1 cells were incubated for 1 h with AuPEI-FITC1 NPs and then separated from the NP-containing dispersion through centrifugation. AAS measurements of these supernatants, as well as of the initial AuPEI-FITC1 NP dispersion added to the cells were performed to determine both gold concentrations. The amount of the AuPEI-FITC1 NPs which are taken up by the cells are subsequently calculated as the difference in gold amount between these two dispersions.

In order to give the gold uptake as amount of NPs per cell, the gold amount per NP was calculated as number of gold atoms per NP as follows:

From the average diameter (D) of AuPEI-FITC1 NPs determined by TEM, the total number of gold atoms (Au_T) in a single NP can be calculated according to the following equation [3]:

$$Au_T = \frac{N_A \cdot \rho \cdot V}{M_{Au}}, \text{ where } V = \frac{4}{3} \cdot \pi \cdot \left(\frac{D}{2}\right)^3,$$

N_A = Avogadro constant, ρ = gold metal density, M_{Au} = gold atomic mass.

For 3 nm AuPEI-FITC1 NPs,

$$V = \frac{4}{3} \cdot \pi \cdot \left(\frac{3nm}{2}\right)^3 = 14 \text{ nm}^3 \text{ and}$$

$$Au_T = \frac{6.022 \cdot 10^{23} \text{ mol}^{-1} \cdot 19.3 \frac{g}{cm^3} \cdot 1.4 \cdot 10^{-20} \text{ cm}^3}{196.9665 \frac{g}{mol}} = 834 \text{ Au atoms per NP.}$$

which we rounded to 1000 Au atoms per NP for our estimation.

The AuPEI-FITC1 NP dispersion had an AAS confirmed concentration of 5.0 mg/L after 500 μ L were diluted to 5 mL, corresponding to a gold mass (m_{Au}) of 25.1 μ g in the sample volume of 5 mL.

An AuPEI-FITC1 NP dispersion volume of 5 mL with an Au concentration of 5.0 mg/L was used for the incubation of one million JHH520, 407 and GBM1 cells.

The supernatant from the incubation experiment then had gold concentration by AAS determined as given in entry 1 in Table S3. From the gold concentration the total mass amount of gold remaining was calculated in μ g (entry 2).

The difference between the initial and remaining gold mass in the dispersion corresponds to the gold mass which is internalized and adsorbed in/on the cells (entry 3).

The gold mass is transformed into number of gold atoms (entry 4) according to (e.g. for GBM1 cells)

$$number_{Au} = \frac{m_{Au}}{M_{Au}} N_A = \frac{0.0000082g}{196.9665 g/mol} 6.022 \cdot 10^{23} = 2.5 \cdot 10^{16} \text{ gold atoms.}$$

Each Au-NP contains about 1000 NP. Hence $2.5 \cdot 10^{16}$ gold atoms correspond to about $2.5 \cdot 10^{13}$ Au-NPs which are internalized and adsorbed (entry 5).

With 10^6 cells used for the incubation, this leaves $2.5 \cdot 10^7$ Au-NPs which are internalized and adsorbed per cell (entry 6).

From the FACS experiments (see Table 1 in paper) the degree of internalization had been determined; e.g. to 61% for GBM1 cells (entry 7).

Thus, from the, e.g., $2.5 \cdot 10^7$ Au-NPs about $1.5 \cdot 10^7$ Au-NPs will be internalized.

Table S3. Estimate of the amount of NP uptake per cell.

Entry	Sample	AuPEI-FITC1 NPs added to the cells	AuPEI-FITC1 in GBM1	AuPEI-FITC1 in JHH520	AuPEI-FITC1 in 407
1	Gold conc. in dispersion (mg/L) (supernatant after cell incubation)	5.00	3.38	3.74	3.65
2	Gold mass in dispersions (µg) (supernatant after cell incubation)	25.1	16.9	18.7	18.3
3	Internalized+Adsorbed Gold mass (µg)	/	8.2	6.4	6.8
4	Number of Gold Atoms	/	$2.5 \cdot 10^{16}$	$2.0 \cdot 10^{16}$	$2.1 \cdot 10^{16}$
5	Number of Au-NPs	/	$2.5 \cdot 10^{13}$	$2.0 \cdot 10^{13}$	$2.1 \cdot 10^{13}$
6	Internalized+Adsorbed Au-NPs per cell	/	$2.5 \cdot 10^7$	$2.0 \cdot 10^7$	$2.1 \cdot 10^7$
7	Internalization degree from FACS (%)	/	61	51	47
8	Internalized Au-NPs per cell from AAS	/	$1.5 \cdot 10^7$	$1.0 \cdot 10^7$	$1.0 \cdot 10^7$
9	Fluorescence Intensity I_f at 520 nm (CPS/µA)	44780	3749	2448	2205
10	Internalized gold mass (µg)	4.50	0.38	0.25	0.22
11	Internalized number of Au-NPs (per 20 000 cells)		$1.2 \cdot 10^{12}$	$8.0 \cdot 10^{11}$	$7.2 \cdot 10^{11}$
12	Internalized Au-NPs per cell from fluorescence spectrosc.	/	$6 \cdot 10^7$	$4 \cdot 10^7$	$3.6 \cdot 10^7$

Along the same lines we double-checked the Au-NP uptake by fluorescence spectroscopy:

Here 20 000 JHH520, 407 and GBM1 cells were incubated for 1 h with AuPEI-FITC1 NPs (at a concentration of 0.9 mg/L after 100 µL were diluted to 5 mL, corresponding to a gold mass (m_{Au}) of 4.5 µg in the sample volume of 5 mL). Then the cells were removed by centrifugation, washed with PBS buffer and separated from the wash solution again through centrifugation. The

remaining cell pellets were re-dispersed in water and their fluorescence intensity was compared to that of the “free” AuPEI-FITC1 NPs in the original dispersion (Figure S18, Table S3 entry 9).

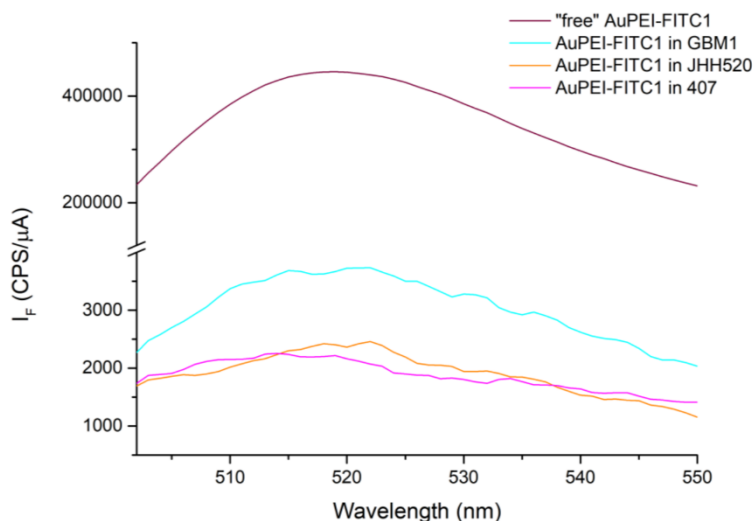


Fig. S18. Fluorescence intensity for the 0.9 mg/L AuPEI-FITC1 dispersion and the cell pellet dispersions after incubation, washing and separation by centrifugation.

The AuPEI-FITC1 dispersion concentration of 0.9 mg/L after 100 μ L were diluted to 5 mL corresponds to a gold mass (m_{Au}) of 4.5 μ g in our sample volume of 5 mL.

From the rule of proportion this gold mass is correlated to the gold mass in the cells through the fluorescence intensity (entry 10 in Table S3).

This gold mass is again transformed into number of gold atoms (see above) and further into number of Au-NPs (on the basis of 1000 Au-atoms/NP, see above), giving entry 11 in Table S3.

With 20 000 or $2 \cdot 10^4$ cells used for the incubation, division by 20 000 then gives the number of NPs which are internalized on average in each cell (entry 12).

The values from entry 8 (estimated internalized Au-NPs/cell from AAS) and entry 12 (estimated internalized Au-NPs/cell from fluorescence spectroscopy) match remarkably well within the same order of magnitude. Thus, we are confident that about 10^7 Au-NPs are internalized on average in each glioblastoma cell.

-
- [1] J. Noireaux, R. Grall, M. Hullo, S. Chevillard, C. Oster, E. Brun, C. Sicard-Roselli, K. Loeschner, P. Fiscaro, *Separations* 6 (2019) 3. <https://doi.org/10.3390/separations6010003>
- [2] S. Lee, X. Bi, R.B. Reed, J.F. Ranville, P. Herckes, P. Westerhoff, *Environ. Sci. Technol.* 48 (2014) 10291–10300. doi: 10.1021/es502422v
- [3] L. Schmolke, S. Lerch, M. Bülow, M. Siebels, A. Schmitz, J. Thomas, G. Dehm, C. Held, T. Strassner, C. Janiak, *Nanoscale* 11 (2019) 4073-4082.

5. Discussion

We initially implemented a high throughput screening technology with the intrinsic benefit of testing multiple compounds at the same time in a time-efficient drug discovery context^{14,27,28}. This approach facilitated time-efficient transparent results with high accuracy and high data reproducibility given the direct electronic data transfer without human operator intervention.

After finishing the drug screen on a highly specialized and characterized GSC *in vitro* model, it was of high interest that out of the 22 identified compounds showing evidence of efficacy, THP and other four high potency compounds had a neurotransmitter-modulating mode of action. To explain this finding, we correlated these results with previous publications, which demonstrated that the growth of gliomas depends on neurotransmitter activity of their neighboring neurons. This phenomenon is reported as *neuro-glioma synapses*^{29,30}. It basically describes how neurons and brain cancer cells form excitatory synapses and generate an electrically active tissue that signals other glioma cells in the network to promote their migration and growth. These findings might provide a possible explanation for the own observation that GSCs were susceptible to neurotransmitter-modulating compounds. Moreover, THP is currently being validated in our group using four additional glioblastoma models and is undergoing *in vivo* trials.

Following the main molecular subtypes of glioblastoma as defined by Verhaak *et al.* in 2010, this transcriptome-based classification was used to perform a data mining *in silico* assessment, employing data sets from the TCGA⁸ and the more recent CGGA¹⁸ databases, which enabled to validate the relevance of the mTOR pathway in a glioblastoma stemness and EMT context.

Therefore, we chose the potent mTOR inhibitor RL1 based on the results of the robotic-screening and validated its therapeutic anti-stem cell and anti-EMT effects against multiple IDH-wt GSC models. These effects are probably attributed to the strong inhibition at low nM concentrations of RL1 that blocks the full mTOR pathway through the mTORC-1 and mTORC-2 proteins, thereby closing the gap left by first generation mTOR inhibitors and promising a high predictive value of clinical efficiency, with lower chances of resistance³¹. Moreover, we identified its synergistic effect when RL1 was combined with TTFIELDS or TMZ. This might point to the benefit of this treatment strategy in a model representing one of the most challenging manifestations of the disease, namely an IDH-wt GSC model without *MGMT* promoter methylation. Ultimately, by showing fewer toxic effects on non-cancer stem cell controls and given the results and previous reports on the effectiveness of RL1 in animal models of human glioblastoma²¹, RL1 was thus established as a promising candidate for future clinical evaluation.

In parallel, we focused on nanoparticles, which are actually very common in nature and in our daily lives³²⁻³⁴. However, only with the advancement of technology have scientists been able to build and customize highly efficient nanoparticles for medical purposes²⁶. Probably, the most recent and notable example is the effective RNA-lipid-nanoparticle vaccines developed against the COVID-19 virus in 2020³⁵. In the context of cancer research and oncology, their

applications cover targeted drug delivery, gene therapy, hyperthermia, radiation therapy, diagnostic mechanisms, controlled release, and others ³⁶. Furthermore, there are currently numerous ongoing nanoparticle-based therapies in clinical trials ³⁷.

We specifically focused on AuNP because they are robust and biocompatible vessels for research, treatment and diagnosis in the medical field ^{38,39}. Some of the main currently used examples of AuNP in oncological clinical trials are the *NU-0129* RNA interference drug delivered on spherical AuNP for the treatment of glioblastoma, and the *AuroLase* drug, consisting of PEG-coated silica-gold nanoshells, for near infrared light thermal ablation in prostate cancer ^{38,40}.

Therefore, working closely with the inorganic chemistry department at Heinrich Heine University, it was possible to reproducibly synthesize fluorescent AuNP with optimal-sized cores between 3 and 6 nm. The use of a novel synthesis strategy called the “one-pot method” allowed to achieve fluorescent AuNPs in a rapid, inexpensive and simple manner. Furthermore, these nanoparticles were successfully used as a practical, effective and biocompatible approach for transfection of GSCs. Thus, basic science nanotechnology was translated into a promising preclinical research nanocarrier for pharmacotherapy, gene therapy or equivalent future applications in the context of GSC research. This generation of a novel locally made product was enabled by a strong research collaboration backed by multiple specifically assigned researchers who continue to work in this project ^{25,41}.

Finally, some of the most relevant knowledge gained in this thesis was the ability to work in a multidisciplinary, multicultural environment, fostering the development of directed *precision medicine* therapies, with a strong translational approach. This experience will be one of the strongest foundations for my professional work in the future.

5.1 General Conclusions

A wide array of modern *precision medicine* technologies were established and successfully used in our research group, including an industry-grade liquid-dispensing robotic device used for semi-automated drug screening. As shown in this thesis, this allowed for the identification of the repurpose-drug-candidate THP, along with 22 other promising compounds, and additionally fostered the extensive characterization of RL1 in glioblastoma models, including successful analyses for synergistic interactions with either temozolomide chemotherapy or *in vitro* TTFields treatment, the latter facilitated by the establishment of a respective TTFields treatment device for research purposes. In parallel, the generated cross-institutional collaboration allowed the translation of basic research inorganic chemistry to preclinical neuro-oncology and neurosurgery, resulting in locally-produced inorganic AuNP nanoparticles as a novel vector for future treatment and other research studies on GSCs. Therefore, the main aims of this doctoral project were achieved by developing and preclinically evaluating novel targeted therapy approaches directed towards the development of targeted next-generation treatments against glioblastoma.

6. References

1. Krzyszczyk P, Acevedo A, Davidoff EJ, et al. The growing role of precision and personalized medicine for cancer treatment. *Technology*. 2018;06(03n04):79-100. doi:10.1142/S2339547818300020
2. National Research Council (US) Committee on A Framework for Developing a New Taxonomy of Disease. *Toward Precision Medicine: Building a Knowledge Network for Biomedical Research and a New Taxonomy of Disease*. National Academies Press (US); 2011. Accessed April 1, 2021. <http://www.ncbi.nlm.nih.gov/books/NBK91503/>
3. Dugger SA, Platt A, Goldstein DB. Drug development in the era of precision medicine. *Nat Rev Drug Discov*. 2018;17(3):183-196. doi:10.1038/nrd.2017.226
4. Alexander BM, Ba S, Berger MS, et al. Adaptive Global Innovative Learning Environment for Glioblastoma: GBM AGILE. *Clin Cancer Res*. 2018;24(4):737-743. doi:10.1158/1078-0432.CCR-17-0764
5. Louis DN, Perry A, Wesseling P, et al. The 2021 WHO Classification of Tumors of the Central Nervous System: a summary. *Neuro Oncol*. Published online June 29, 2021: noab106. doi:10.1093/neuonc/noab106
6. Weller M, van den Bent M, Preusser M, et al. EANO guidelines on the diagnosis and treatment of diffuse gliomas of adulthood. *Nat Rev Clin Oncol*. 2021;18(3):170-186. doi:10.1038/s41571-020-00447-z
7. Tonn J-C, Reardon DA, Rutka JT, Westphal M, eds. *Oncology of CNS Tumors*. Springer International Publishing; 2019. Accessed October 16, 2020. <http://link.springer.com/10.1007/978-3-030-04152-6>
8. Verhaak RGW, Hoadley KA, Purdom E, et al. Integrated Genomic Analysis Identifies Clinically Relevant Subtypes of Glioblastoma Characterized by Abnormalities in PDGFRA, IDH1, EGFR, and NF1. *Cancer Cell*. 2010;17(1):98-110. doi:10.1016/j.ccr.2009.12.020
9. Spinelli C, Montermmini L, Meehan B, et al. Molecular subtypes and differentiation programmes of glioma stem cells as determinants of extracellular vesicle profiles and endothelial cell-stimulating activities. *J Extracell Vesicles*. 2018;7(1):1490144. doi:10.1080/20013078.2018.1490144
10. Bonnet D, Dick JE. Human acute myeloid leukemia is organized as a hierarchy that originates from a primitive hematopoietic cell. *Nat Med*. 1997;3(7):730-737. doi:10.1038/nm0797-730
11. Beck B, Blanpain C. Unravelling cancer stem cell potential. *Nat Rev Cancer*. 2013;13(10):727-738. doi:10.1038/nrc3597
12. Shackleton M, Quintana E, Fearon ER, Morrison SJ. Heterogeneity in cancer: cancer stem cells versus clonal evolution. *Cell*. 2009;138(5):822-829. doi:10.1016/j.cell.2009.08.017
13. Singh SK, Hawkins C, Clarke ID, et al. Identification of human brain tumour initiating cells. *Nature*. 2004;432(7015):396-401. doi:10.1038/nature03128
14. Yates LR, Seoane J, Le Tourneau C, et al. The European Society for Medical Oncology (ESMO) Precision Medicine Glossary. *Ann Oncol*. 2018;29(1):30-35. doi:10.1093/annonc/mdx707

15. Jain KK. Personalized medicine. *Curr Opin Mol Ther.* 2002;4(6):548-558.
16. Stupp R, Wong ET, Kanner AA, et al. NovoTTF-100A versus physician's choice chemotherapy in recurrent glioblastoma: A randomised phase III trial of a novel treatment modality. *European Journal of Cancer.* 2012;48(14):2192-2202. doi:10.1016/j.ejca.2012.04.011
17. Stupp R, Taillibert S, Kanner A, et al. Effect of Tumor-Treating Fields Plus Maintenance Temozolomide vs Maintenance Temozolomide Alone on Survival in Patients With Glioblastoma: A Randomized Clinical Trial. *JAMA.* 2017;318(23):2306. doi:10.1001/jama.2017.18718
18. Vargas-Toscano A, Nickel A-C, Li G, et al. Rapalink-1 Targets Glioblastoma Stem Cells and Acts Synergistically with Tumor Treating Fields to Reduce Resistance against Temozolomide. *Cancers.* 2020;12(12):3859. doi:10.3390/cancers12123859
19. Stupp R, Weller M, Belanger K, et al. Radiotherapy plus Concomitant and Adjuvant Temozolomide for Glioblastoma. *The New England Journal of Medicine.* Published online 2005:10.
20. Sleire L, Førde HE, Netland IA, Leiss L, Skeie BS, Enger PØ. Drug repurposing in cancer. *Pharmacol Res.* 2017;124:74-91. doi:10.1016/j.phrs.2017.07.013
21. Fan Q, Aksoy O, Wong RA, et al. A Kinase Inhibitor Targeted to mTORC1 Drives Regression in Glioblastoma. *Cancer Cell.* 2017;31(3):424-435. doi:10.1016/j.ccell.2017.01.014
22. Wick W, Dettmer S, Berberich A, et al. N2M2 (NOA-20) phase I/II trial of molecularly matched targeted therapies plus radiotherapy in patients with newly diagnosed non-MGMT hypermethylated glioblastoma. *Neuro-Oncology.* 2019;21(1):95-105. doi:10.1093/neuonc/noy161
23. Popova NV, Jücker M. The Role of mTOR Signaling as a Therapeutic Target in Cancer. *IJMS.* 2021;22(4):1743. doi:10.3390/ijms22041743
24. Zheng Y, Jiang Y. mTOR Inhibitors at a Glance. *Mol Cell Pharmacol.* 2015;7(2):15-20.
25. Giesen B, Nickel A-C, Garzón Manjón A, et al. Influence of synthesis methods on the internalization of fluorescent gold nanoparticles into glioblastoma stem-like cells. *J Inorg Biochem.* 2020;203:110952. doi:10.1016/j.jinorgbio.2019.110952
26. Zingg R, Fischer M. The consolidation of nanomedicine. *Wiley Interdiscip Rev Nanomed Nanobiotechnol.* 2019;11(6):e1569. doi:10.1002/wnan.1569
27. Macarron R, Banks MN, Bojanic D, et al. Impact of high-throughput screening in biomedical research. *Nat Rev Drug Discov.* 2011;10(3):188-195. doi:10.1038/nrd3368
28. Dorval T, Chanrion B, Cattin M-E, Stephan JP. Filling the drug discovery gap: is high-content screening the missing link? *Curr Opin Pharmacol.* 2018;42:40-45. doi:10.1016/j.coph.2018.07.002
29. Barria A. Dangerous liaisons as tumour cells form synapses with neurons. *Nature.* 2019;573(7775):499-501. doi:10.1038/d41586-019-02746-7
30. Allen NJ. Brain tumours manipulate neighbouring synapses. *Nature.* 2020;578(7793):46-47. doi:10.1038/d41586-020-00137-x

31. Chiarini F, Evangelisti C, Lattanzi G, McCubrey JA, Martelli AM. Advances in understanding the mechanisms of evasive and innate resistance to mTOR inhibition in cancer cells. *Biochimica et Biophysica Acta (BBA) - Molecular Cell Research*. 2019;1866(8):1322-1337. doi:10.1016/j.bbamcr.2019.03.013
32. Glover RD, Miller JM, Hutchison JE. Generation of metal nanoparticles from silver and copper objects: nanoparticle dynamics on surfaces and potential sources of nanoparticles in the environment. *ACS Nano*. 2011;5(11):8950-8957. doi:10.1021/nn2031319
33. Donaldson K, Tran L, Jimenez LA, et al. Combustion-derived nanoparticles: a review of their toxicology following inhalation exposure. *Part Fibre Toxicol*. 2005;2:10. doi:10.1186/1743-8977-2-10
34. Dalby B, Cates S, Harris A, et al. Advanced transfection with Lipofectamine 2000 reagent: primary neurons, siRNA, and high-throughput applications. *Methods*. 2004;33(2):95-103. doi:10.1016/j.ymeth.2003.11.023
35. Nanomedicine and the COVID-19 vaccines. *Nat Nanotechnol*. 2020;15(12):963. doi:10.1038/s41565-020-00820-0
36. Ahmed N, Fessi H, Elaissari A. Theranostic applications of nanoparticles in cancer. *Drug Discov Today*. 2012;17(17-18):928-934. doi:10.1016/j.drudis.2012.03.010
37. Anselmo AC, Mitragotri S. Nanoparticles in the clinic: An update. *Bioeng Transl Med*. 2019;4(3):e10143. doi:10.1002/btm2.10143
38. Kumthekar P, Ko CH, Paunesku T, et al. A first-in-human phase 0 clinical study of RNA interference-based spherical nucleic acids in patients with recurrent glioblastoma. *Sci Transl Med*. 2021;13(584). doi:10.1126/scitranslmed.abb3945
39. Lee B, Lee K, Panda S, et al. Nanoparticle delivery of CRISPR into the brain rescues a mouse model of fragile X syndrome from exaggerated repetitive behaviours. *Nat Biomed Eng*. 2018;2(7):497-507. doi:10.1038/s41551-018-0252-8
40. Movia D, Benhaddada M, Spadavecchia J, Prina-Mello A. Latest advances in combining gold nanomaterials with physical stimuli towards new responsive therapeutic and diagnostic strategies. *Precision Nanomedicine*. Published online April 22, 2020. doi:10.33218/001c.12650
41. Giesen B, Nickel A-C, Barthel J, Kahlert UD, Janiak C. Augmented Therapeutic Potential of Glutaminase Inhibitor CB839 in Glioblastoma Stem Cells Using Gold Nanoparticle Delivery. *Pharmaceutics*. 2021;13(2). doi:10.3390/pharmaceutics13020295

7. Acknowledgements

I thankfully acknowledge Priv.-Doz. Dr. Ulf Kahlert, Prof. Dr. Michael Sabel, Prof. Dr. Guido Reifenberger and Prof. Dr. Hans-Jakob Steiger for their support and supervision. Dr. Ann-Christin Nickel, Michael Hewera and the rest of the lab members are acknowledged for kindly providing technical assistance. I thank Dr. Katharina Koch, Donata Maciaczyk and Prof. Dr. Jarek Maciacyck for initial support. Last but not least, I'm grateful to Prof. Dr. Christoph Janiak and Dr. Beatriz Giesen for the rich collaboration.